EMPIRICAL STUDIES ON THE INITIATION OF IMPULSIVE HEATING IN CORONAL LOOPS

by

Adam Robert Kobelski

A dissertation submitted in partial fulfillment
of the requirements for the degree

of

Doctor of Philosophy

in

Physics

MONTANA STATE UNIVERSITY
Bozeman, Montana

May 2014

DEDICATION

To my grandparents, Lauretta and Robert Pyzel.

ACKNOWLEDGEMENTS

The completion of this work and stage of education could not have been accomplished alone. It has required a lot of help and support to get to this point, and I need to thank the following individuals and groups who made it possible for me to finish this dissertation while still maintaining some of my sanity and hair.

I need to thank Dr. David McKenzie (and his wife Dr. Wendy Chou) for enabling me to work with him, funding my research, and also his patience with me. This dissertation would not be possible without his direct assistance. His support has allowed me to travel to places I never thought I'd see (like Titusville FL) and kept me working even through failed projects and tight wallets.

I would also like to acknowledge and thank the XRT team (particularly Mark Weber, Kathy Reeves, Steve Saar, and Trae Winter at SAO and Sabrina Savage at MSFC) for their help and guidance with the XRT instrument, and making me feel part of the solar physics community. Lucas Tarr has been an excellent friend, drinking buddy, and conference cohort. Margaret Jarrett and Keiji Yoshimura have forever gained my respect through their positive attitude and help throughout the years.

My family has always been supportive, even when it took this long for me to finish. I would never have gotten this far without the opportunities and support they have given me. Finally, I thank my wife, Kathryn Williamson, for her love and support even when I wanted to quit. The long distance is almost over. At least for now.

TABLE OF CONTENTS

TABLE OF CONTENTS – CONTINUED

LIST OF TABLES

LIST OF TABLES – CONTINUED

LIST OF FIGURES

LIST OF FIGURES – CONTINUED

LIST OF FIGURES – CONTINUED

Figure Page

LIST OF FIGURES – CONTINUED

LIST OF FIGURES – CONTINUED

LIST OF FIGURES – CONTINUED

LIST OF FIGURES – CONTINUED

LIST OF FIGURES – CONTINUED

Figure Page

LIST OF FIGURES – CONTINUED

LIST OF FIGURES – CONTINUED

Figure Page

LIST OF FIGURES – CONTINUED

Figure Page

ABSTRACT

The heating of the solar corona is an important topic both for scientists and modern society. One of the most fundamental of structures in the corona are bundles of plasma confined to the magnetic field, loops. Here we perform empirical studies to better understand the mechanisms responsible for heating loops. We observe loops in X-rays with XRT and model the observations as bundles of independent strands, showing that the mechanisms instigating the heating of loops is likely impulsive, yet requires multiple heating events to match observations. We also observe and model very small loops with Hi-C, exploiting the high resolution to show that the frequency with which small loops are heated is larger than expected. This study also puts constraints on the size of the heating events. We also perform a study on the initiation of magnetic reconnection between neighboring active regions, in hopes of understanding how magnetic fields interact, evolve and heat coronal loops. We close with a discussion on calibrating the data from a solar X-ray telescope and interpret the uncertainties within.

1. INTRODUCTION

“Always Never Know When to Quit”

— Jared Warren

Given the central part the sun plays in human existence, it may be surprising how many fundamental solar processes are not yet fully understood. When the complex nature of these processes is considered, though, it is quite impressive how much information about the sun has been gained in such a relatively short period of time. A full description of human understanding of the sun and stars is beyond the description of a single document, but in this chapter we will undertake a brief overview of our knowledge of the sun, in particular the parts relevant to our current study, the corona.

1.1. A Brief History of Observing the Corona

Neglecting early observations of solar eclipses, our discussion of the corona begins in the middle 19th century with a combination of events. In 1859 the first solar flare[1] was observed in visible light independently by Richard Carrington and Richard Hodgson. The solar activity surrounding this flare caused a geomagnetic storm large enough to create aurorae in the tropics and disrupt telegraph systems. A correlation between solar activity and terrestrial effects had only recently been suggested by Edward Sabine, Rudolf Wolf and Jean-Alfred Gautier in 1852, all of whom independently

---

[1] Though it was reported that Stephen Fry observed a “flash of lightning” near a sunspot in 1705

noticed strikingly similar periods between the sunspot cycle and geomagnetic activity. These events helped drive the need for understanding the link in the Sun-Earth system, inadvertently establishing the field of space-weather prediction.

In 1860 and 1861, James Clerk Maxwell published early forms of equations describing electrodynamics which would evolve into the famous Maxwell's Equations. These deceptively simple but elegant equations made it possible to classically understand the dynamics and statics of electromagnetic fields. The importance of these equations to our understanding of the sun was not fully realized until George Ellery Hale established the magnetic nature of sunspots in 1908 (Hale, 1908) by observing the Zeeman splitting of spectral lines (Zeeman, 1897).

While strongly related to coronal activity, these observations were of the solar photosphere: the outermost layer commonly visible to the unaided human eye, but below the corona. During eclipses and using specific filters, the corona and chromosphere can be seen, but in general, the 6000 K photosphere was the focus of study. We now know that the corona is much hotter (over 1 million K in many places) than the photosphere, and the light emitted from the disk of the corona generally requires an X-ray or extreme ultraviolet (EUV) telescope for detection[2]. These high

---

[2] It is worthwhile to differentiate between the high energy wavelengths; the line between EUV and soft X-rays is often blurred, and for some wavelengths these terms are used interchangeably. In this dissertation, EUV is defined as the high energy photons with wavelengths $75\text{Å} \lesssim \lambda \lesssim 1200$ Å, generally detected by normal incidence telescopes (such as AIA and TRACE); soft X-rays are in the range of $2\text{Å} \lesssim \lambda \lesssim 75$ Åwhich generally require grazing incidence optics (such as the *Yohkoh* Soft X-ray Telescope (SXT) and *Hinode*/XRT); hard X-rays ($\lambda \lesssim 2$Å) require more complicated imaging methods (such as the Fourier imaging used on the Reuven Ramaty High Energy Solar Spectroscopic Imager (RHESSI)).

energy photons are blocked by our atmosphere, requiring space based telescopes for detection.

The difficulty in capturing coronal emission made the study of the solar corona somewhat limited until the 20th century. In addition to the difficulties in viewing coronal EUV and X-rays, the low densities of the corona cause the longer wavelength light to be obscured by the light from denser regions (such as the photosphere). This aspect was alleviated when the coronagraph was invented by Bernard Lyot in 1931, allowing astronomers the ability to observe an eclipse (and thus parts of the corona) at any time. Early coronagraphic measurements suggested temperatures in the sun in excess of 600,000 K (Lyot & Marshall, 1933; Grotrian, 1939), but were not immediately accepted. In 1942, James Stanley Hey (Hey, 1946, and others independently) detected solar radio emission from a sunspot region, which were later used to suggest over 1 MK temperatures around sunspot regions. Unlike high energy photons, radio waves can pass through the atmosphere, but were very difficult to detect until shortly after these discoveries. A more direct confirmation of high temperature coronal plasma came when in 1949 a detector from the U.S. Naval Research Lab on board a sounding rocket was able to detect solar soft X-rays, confirming the existence of the million degree solar corona. Thus began the era of the "coronal heating problem," as it is difficult to reconcile a 6000 K region heating the plasma only a few hundred km above it to temperatures orders of magnitude hotter, even when considering that the densities drop off at a similar rate. In some regards, the coronal heating problem could be considered “solved;” the problem now is that we have too many possible solutions (some of which are described below), few of which can be fully disproven.

A series of sounding rockets taking measurements of the EUV and X-ray sun in the 1950s and 1960s paved the way to the development of instruments on-board SkyLab in the 1970s. The success of SkyLab helped usher in the era of satellite missions such as *Yohkoh* (1991-2001), the Solar and Heliospheric Observatory (SOHO, 1995-), the Transition Region And Coronal Explorer (TRACE, 1998-2010), *Hinode* (2006-), and the Solar Dynamics Observatory (SDO, 2010-) among many others. Of particular interest for this dissertation are the X-Ray Telescope (XRT) on *Hinode*; the Atmospheric Imaging Assembly (AIA) and the Helioseismic and Magnetic Imager (HMI) onboard SDO; the Sun Watcher with Active Pixels and Image Processing (SWAP) on the Project for Onboard Autonomy (Proba2); and the Hi-resolution Coronal Imager (Hi-C) sounding rocket. The details of these instruments will be discussed throughout.

1.2. Solar Magnetic Fields

Currently, the three most commonly cited solutions to the coronal heating problem are the dissipation of heat from a variety of magnetic waves, mass flows into the corona along magnetic fields (such as via spicules), and small scale magnetic reconnection events. While the methods of action of these solutions are different, the solar magnetic field is the driving factor for all of them.

While the central source of heating for the sun (and all stars) is nuclear fusion in the core, the primary agency for the observed dynamics near the surface is the magnetic field. In simple terms, the high temperatures in the sun cause the positively charged (heavy) atomic nuclei to separate from the much lighter negatively charged electrons, creating a plasma. The disassociated, moving parts of the plasma support currents, inducing magnetic fields as predicted and described by Maxwell's equations. Just below the photosphere lies the solar convection zone, where hot plasma rises to the photosphere, cools and drops back down. The flowing plasma of the convection zone creates a differential rotation, whereby different latitudes of the star rotate at different rates ($\approx$34 days rotation near the poles and $\approx$25 day rotation near the equator). Over the course of $\approx$11 years, this differential rotation will cause a global bipolar magnetic field to become more sporadic, creating smaller scale magnetic fields during solar maximum, finally returning to a bipolar state (though with the polarity reversed) approximately 11 years later (solar minimum). This is referred to as the solar cycle, with each cycle referring to a half period of the greater $\approx$22 year solar field oscillation. The finer details of this cycle are still not fully understood, and would take many documents longer in length than available here to describe.

The convection zone plasma will create conglomerations of magnetic fields, which interact with the plasma. If these magnetic fields get strong enough, they can disrupt the convection, leaving a "cool" spot in the photosphere with a strong magnetic field: a sunspot. These magnetic fields extend up from the photosphere ($>10^{16}$ particles cm^{-3}, Eddy & Ise, 1979) through the chromosphere and transition region into the corona where the density is much lower ($\approx 10^8$ particles cm^{-3}). This lowered plasma density in the corona causes the plasma to act quite differently. In the convection zone, the magnetic field is moved around and twisted by the convecting plasma. In the corona, on the other hand, the plasma pressure is so low compared to the strength of the magnetic field that the magnetic field moves the plasma. The plasma in the corona is confined to move along lines of the magnetic field. Due to the multi-polar nature of magnetic fields, these magnetic field lines appear to rise from a “monopolar” source region in the photosphere up into the corona, and then back down into the photosphere, terminating at a monopolar region of opposite polarity. The photospheric monopoles mentioned here are not actually magnetic monopoles, but the ends of slender flux tubes which can be treated as monopoles if we ignore what happens below the photosphere (as is very common in coronal physics; see for example Longcope, 2005).

The magnetic field lines are not required to return back into the sun; concentrations of non-returning (referred to as “open”) fields create coronal holes (see Figure 1). Dense regions of magnetic field lines that return to the photosphere are active regions (ARs) (see Figure 1). It is here in coronal ARs that the bulk of the discussion of this dissertation will take place. The magnetically confined plasma orbits around the magnetic field lines, emitting photons due to atomic transitions which correspond to the temperature of the plasma. The high temperature of this plasma limits the

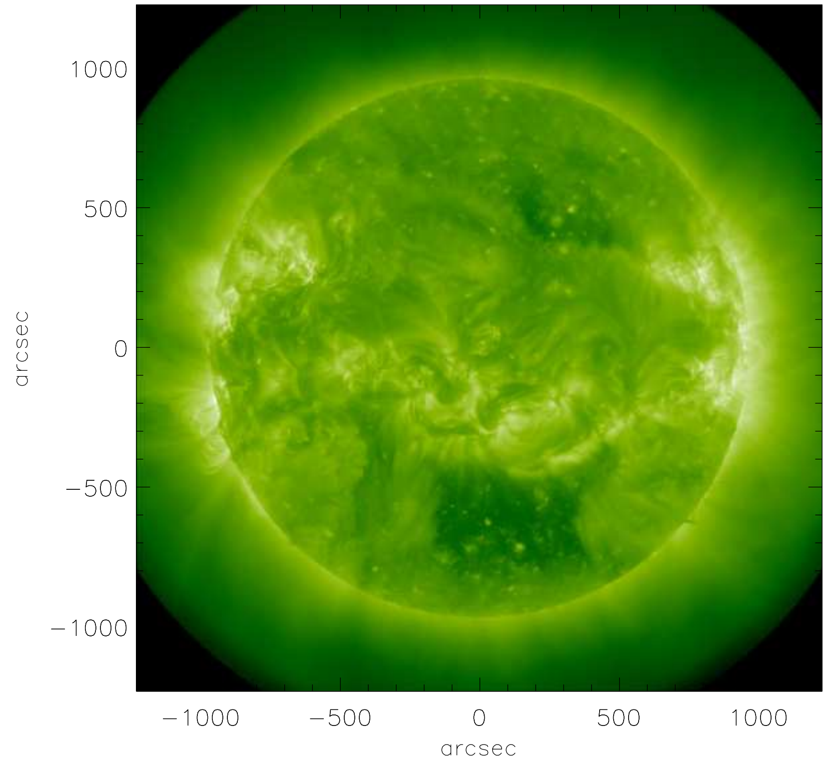

Figure 1: Example image from SDO/AIA 193 Å, taken on 2014 April 10 00:15:18 UT. The dark areas in the north and south are coronal holes, and on the east and west limbs loops of confined plasma are visible within active regions.

emission in the corona primarily to EUV and soft X-ray wavelengths, though the interaction of the plasma with the magnetic field and higher density plasma can create emission in other photon energies, such as the high energy hard X-ray spectrum and the low energy radio spectrum.

1.3. Flares, Microflares and Nanoflares

Due in part to the dynamics of the photosphere below, the coronal magnetic fields can become unstable. An instability can cause the field lines to reconfigure into a lower energy state by reconnecting to each other (magnetic reconnection), releasing large amounts of energy, often in the form of light emission and particle acceleration. A solar flare is created when enough energy is converted to heat, which in turn promotes the generation of photons causing the region to become orders of magnitude more bright. A coronal mass ejection (CME) is created when the reconnection directs a significant amount of material outwards away from the sun, a subtle distinction only accepted relatively recently (Gosling, 1993). The amount of magnetic energy converted into radiation and particle acceleration is a topic of much current discussion (*e.g.*, Kazachenko et al., 2012; Tarr et al., 2013), partially due to the difficulties of measuring and modeling the magnetic field of the corona.

The distinction between flares and CMEs is made more difficult as many CMEs have associated flares, and many flares have associated CMEs. In fact, the standard 2D flare model (as described in Benz, 2008, and shown in Figure 2), often referred to as the CSHKP model (Carmichael, 1964; Sturrock, 1968; Hirayama, 1974; Kopp & Pneuman, 1976), includes a CME. In the standard 2D CSHKP model, magnetic field lines pointing in opposite directions become increasingly close together. If the sheet separating the fields become sufficiently thin, they will reconnect. The reconnected magnetic field (and associated plasma) above the reconnection point creates a plasmoid which is then accelerated and travels into space as a CME. When expanded to three (or 2.5) dimensions, the CME becomes a flux rope, where the component perpendicular to the 2D model may continue to tie the CME to the star. CME ejection is an important component for the prediction of space weather, but is outside of the scope of this dissertation. The field lines (and associated plasma) below the point of reconnection relax and shrink towards the sun. The plasma within the shrinking loop is accelerated towards the chromosphere and photosphere, interacting with the higher density plasma below it, creating flare ribbons (Qiu et al., 2010; Cheng et al., 2012). Plasma from the transition region then evaporates and fills the coronal loop, causing the loop to become bright, creating an arcade of loops in the 2.5D and 3D cases.

Obviously, this is a simplified version of the process. As shown in Figure 2, significant work has been done and continues to be done for each stage of the process. The complicated topologies involved in the real 3D corona make it difficult for such a simplistic map of flares to adequately describe the observations. When attempting to move from the idealized cartoon to a numerical model, the difficulties become even greater. The spatial scales involved in solar flares (hundreds of Mm), and energies involved (up to 10^{32} ergs) involve many scales and flows, which make it difficult to simplify the physical equations. To avoid some of the complications involved at the spatial, temporal and energetic scales of flares, much of this dissertation will focus on much smaller reconnection events, sometimes referred to as microflares.

It has been hypothesized (Parker, 1983) that small flaring events, roughly nine orders of magnitude smaller than flares (hence the term nanoflares), could be responsible for heating the corona. This involves many small reconnection events in loops

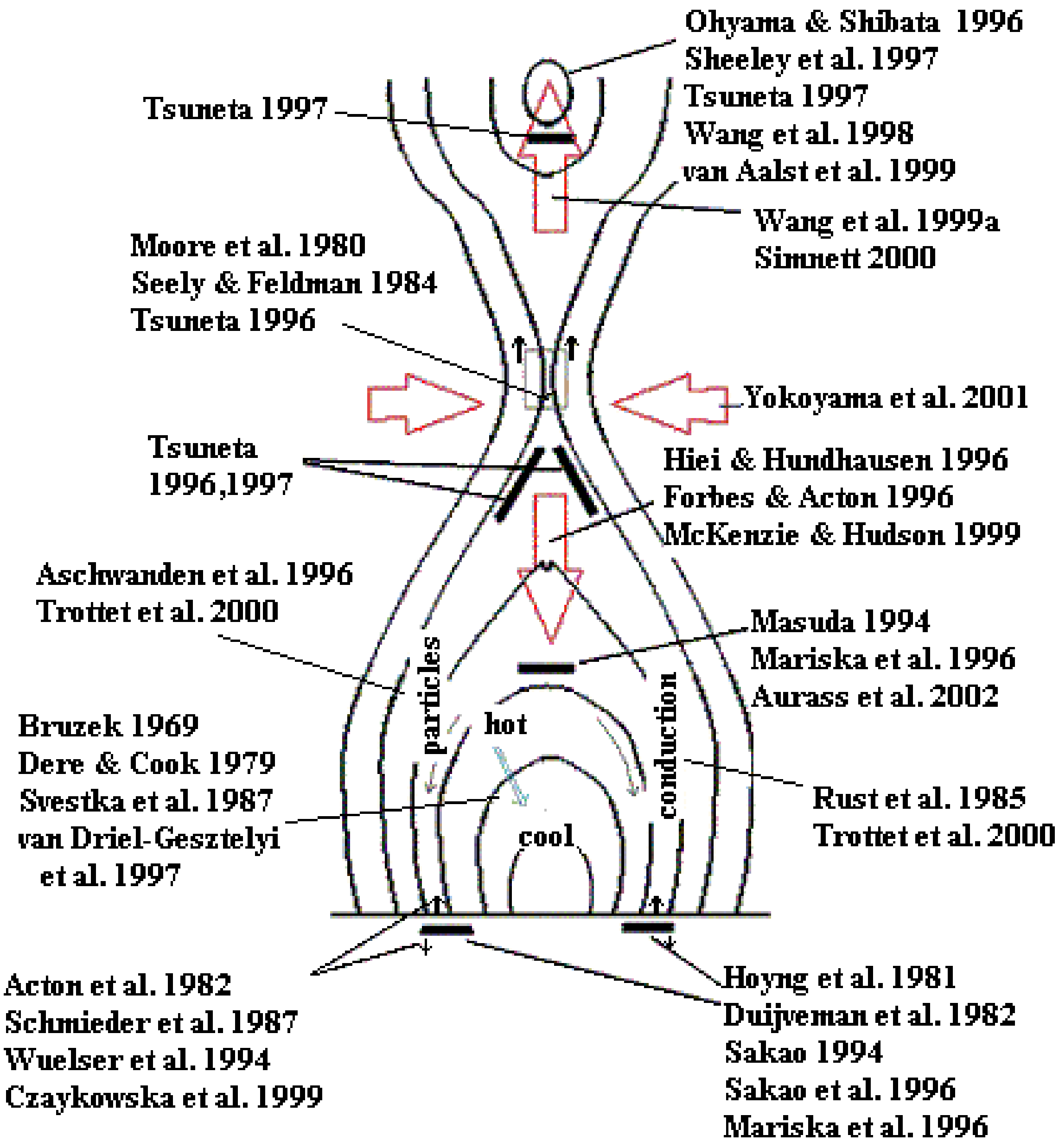

Figure 2: Standard 2D CSHKP flare model, taken from McKenzie (2002), showing the basic mechanisms of the model as well as the relevant citations to papers describing each mechanism.

creating the hot corona. This has been explained as magnetic “braiding” (theorized in Parker (1983, 1988), observed in Cirtain et al. (2013)). For this type of magnetic heating to be responsible for the coronal temperature, though, the number of flaring events (N) must increase as the energy of the flaring events (W) decreases (Hudson, 1991):

$$\frac{dN}{dW} \sim W^{-\alpha} \tag{1.1}$$

where $\alpha > 2.0$. Many studies have found smaller values for α (generally around 1.8 Lee et al., 1993; Mercier & Trottet, 1997; Gary et al., 1997; Krucker & Benz, 1998, among many others), suggesting that nanoflares are not the sole source of heating in the corona. Nevertheless, signatures of nanoflares can be seen in the corona, and play a role in the total heat input.

Energetically smaller than archetypal flares, but larger than nanoflares, exists a range of events referred to as microflares. Whereas nanoflares are often too small to be directly observed (and are hence often inferred), microflares are readily visible as transient brightening events in the corona, observationally linking nanoflares to flares. In addition to being an important aspect of the total heat input into the corona, microflares are important to study as their frequency of occurrence is significantly higher than that of flares (see Chapter 3 for a discussion of their frequency), allowing for statistical study. Additionally, microflaring activity occurs throughout the corona, as opposed to flares, which are generally only found in active regions. Microflaring activity may exhibit different behaviors in different environments, so they are sometimes differentiated by location. In the case of stand alone microflares in active regions, they are historically referred to as active region transient brightenings (ARTBs), as discussed in Chapter 2. The smaller sizes and scales involved with microflares also allows the models describing them to be more readily simplified compared to those of flares. It is for these reasons that we have utilized microflares for the studies described in Chapters 2 and 3.

1.4. Overview and Method of Study

It is well accepted that reconnection plays a role in the large scale flaring activity in the corona, though the scales involved and the exact role of reconnection are still debated. There are a variety of models and theories available to describe the dynamics of the sun, and it is thus very important to develop observational tests for the different methods of plasma heating and to develop observational constraints in order to build better models. The focus of this dissertation is to gain this observational insight, and is accomplished using observations from many different space based telescopes in combination with simple models to help close the gap between model and reality.

To help close this gap, in Chapter 2, we look for brightenings around an active region (ARTBs), observed with XRT. We model these observed ARTBs as loops made of bundles of independent strands, to better understand the parameters involved in heating the plasma. We use a highly efficient modeling algorithm to build individual strands: the 0D Enthalpy Based Thermal Evolution of Loops model (EBTEL, Klimchuk et al., 2008; Cargill et al., 2012a,b). A 1D model uses the properties of magnetic confinement to simplify the dynamics of a strand such that only the dimension parallel to the magnetic field line needs to be considered. This simplification allows significantly faster computational calculation of the evolution of the strand. EBTEL further simplifies a 1D model by only calculating the average parameters across the length of individual strands (creating a 0D model since the result lacks direct spatial variance). We superimpose independent strands from EBTEL to create multi-stranded loops, which we then compare to the observed brightenings from XRT. By utilizing a genetic algorithm to explore the parameter space of model loops, we minimize the difference between the model loop and the observed ARTB, in a technique often referred to as forward-modeling. Chapter 2 describes the ARTB detection algorithm and modeling method in detail, and also discusses the results of using the algorithm on XRT data. A notable aspect of this analysis method is that reconnection is not required to be the source of heating, allowing insight into potential alternative heating mechanisms around active regions (such as wave heating mechanisms). The results of this study show that an impulsive onset to the heating of the plasma is preferred, which strongly favors a reconnection-like trigger to the heating. We also find that at the spatial and temporal resolutions of XRT it is difficult to distinguish between a single strand being heated multiple times and multiple strands heated just once. Extra plots from this study are shown in Appendix B.

In Chapter 3 we utilize the detection and modeling method detailed in Chapter 2, and apply it to data from Hi-C. Hi-C was a sounding rocket launched in 2012, which took the highest resolution EUV images known. Utilizing a 5.5s cadence and 0.1” pixels, Hi-C had temporal resolution approximately twice that of AIA (≈12 s), and sixfold improvement in spatial resolution (≈0.6” pixels). We use this increased sensitivity to detect and analyze a very large number of events, and find that these events occur more frequently than expected, and at very small scales. The results of modeling the observed microflares indicate a preference for an impulsive initiation to the heating, as well as preference for single strands being heated multiple times at the spatial scales and temperatures of Hi-C. Extra plots from this study are shown in Appendix C.

In Chapter 4, we study the instigation of reconnection events after flux emergence. When a set of flux tubes from a new active region emerges from the photosphere into the corona near a pre-existing active region, the preferred (lower) energy state is for the two active regions to be magnetically connected. The magnetic reconnection between such active regions can be seen and often occurs after 12-24 hours (Longcope et al., 2005; Zuccarello et al., 2008; Tarr et al., 2014), but the delay between emergence and reconnection has not been fully explained. Here we analyze flux emergence as observed with HMI, and look for reconnection events with SWAP in order to better understand and quantify this delay. As with Chapters 2 and 3, this allows us to understand empirically the mechanisms that instigate magnetic reconnection. We will provide a brief summary of the future of these projects in Chapter 5.

When analyzing the data from any instrument, it is imperative to understand the acquisition and calibration of that data, in order to interpret accurately the results obtained. As part of my research, I helped develop and quantify the data calibration for XRT. As this is an important aspect of data usage, it is included as Appendix A, where we discuss the steps used to calibrate XRT, and also discuss the uncertainties left in the data. This calibration is similar to the calibration required for other instruments. A surprising result from the study is the relative magnitude of JPEG compression errors versus photon counting uncertainties (shot noise): JPEG block artifacts are dwarfed in magnitude by shot noise, especially when looking at binned data.

2. MODELING ACTIVE REGION TRANSIENT BRIGHTENINGS OBSERVED WITH XRT AS MULTI-STRANDED LOOPS

Contribution of Authors and Co–Authors

Manuscript in Chapter 2

Author: Adam R. Kobelski

Contributions: Conceived and implemented study design. Wrote first draft.

Co–Author: David E. McKenzie

Contributions: Helped to conceive study. Provided feedback of analysis and comments on drafts of the manuscript.

Co–Author: Martin Donachie

Contributions: Summer Research Experience for Undergraduates Student. Helped test early versions of the detection software.

Manuscript Information Page

Adam R. Kobelski, David E. McKenzie and Martin Donachie
The Astrophysical Journal
Status of Manuscript:
____Prepared for submission to a peer–reviewed journal
____Officially submitted to a peer–reviewed journal
____Accepted by a peer–reviewed journal
_x__Published in a peer–reviewed journal

Published April, 2014, The Astrophysical Journal

ABSTRACT

Strong evidence exists that coronal loops as observed in EUV and soft X-rays may not be monolithic isotropic structures, but can often be more accurately modeled as bundles of independent strands. Modeling the observed active region transient brightenings (ARTBs) within this framework allows exploration of the energetic ramifications and characteristics of these stratified structures. Here we present a simple method of detecting and modeling ARTBs observed with the *Hinode* X-Ray Telescope (XRT) as groups of 0-dimensional strands, which allows us to probe parameter space to understand better the spatial and temporal dependence of strand heating in impulsively heated loops. This partially automated method can be used to analyze a large number of observations to gain a statistical insight into the parameters of coronal structures including the number of heating events required in a given model to fit the observations. In this chapter we present the methodology, and demonstrate its use in detecting and modeling ARTBs in a sample data set from *Hinode*/XRT. These initial results show that in general, multiple heating events are necessary to reproduce observed ARTBs, but the spatial dependence of these heating events could not yet be established.

"I heard he dabbled into witchcraft,
I heard occult
Oh, they're pretty much the same"

— Jared Warren

2.1. Introduction

Flaring structures have been historically represented with models of quickly heated monolithic loops, whose cross-sections can be characterized by a single temperature (Cargill et al. (1995); Yoshida et al. (1995)). This kind of monolithic model has difficulties reproducing the observations, particularly when it comes to reproducing the energy budget and temporal profiles of the temperature, density and emitted radiation (Reeves & Warren (2002)). These monolithic models tend to have plasma cooling faster than observed. One possible explanation for the inconsistency is that the observed single loop is actually a more complex structure that can be described by multiple unresolved strands, with each strand heating and cooling independently (such as shown in: Cargill, 1994; Warren, 2006; Sarkar & Walsh, 2008). Recent data from the Hi-C (Cirtain et al., 2013, and Chapter 3) sounding rocket strongly support this explanation of threaded loops as do the results of Brooks et al. (2012) using the Extreme Ultraviolet Imaging Spectrometer (EIS; Culhane et al., 2007).

Full 3-dimensional modeling of braided strands is computationally intensive, which hinders the models' utility for comparison to observations. When fast computation is required, physical simplifications can be made. The most common simplification derives from the strong magnetic confinement of plasma in coronal strands, which allows the structure to be simplified to one dimension (1D), parallel to the magnetic field. Direct comparison of these 1D models to observations requires the flux tube to be resolved in observation. We can further reduce these 1D models to obtain a zero-dimensional (0D) model. The 0D calculations are commonly performed in two ways. The first method is to simplify the whole strand to the details at a single location along its length (such as done by Cargill et al. (1995)), the second method is to simplify the equations for parameters averaged over the entire strand (such as done by Klimchuk et al. (2008)). By utilizing an averaging 0D model to compare to observations, we can achieve quick computations while maintaining an accurate physical description (still bearing in mind the simplifications inherent in collapsing a coronal loop to zero dimensions).

Previous works (e.g. Reeves & Warren (2002); Warren (2006)) have modeled the cooling of flares as multi-stranded loops and found that to recreate the observations, multiple strands cooling independently are necessary; but studies like these frequently focus on a single case. Brooks et al. (2012) used *Hinode* EIS, and the Atmospheric Imaging Assembly (AIA; Lemen et al., 2012) on board the Solar Dynamics Observatory (SDO; Pesnell et al., 2012) to measure the differential emission measure (DEM) of impulsively heated loops to find lower limits on the number of structures within an active region loop. Ugarte-Urra & Warren (2013) used AIA to study the temporal profiles of impulsively heated active region loops. To build on these (among other) previous works, we have undertaken a study using active region transient brightenings (ARTBs) observed with the X-Ray Telescope (XRT: Kano et al., 2008; Narukage et al., 2011; Golub et al., 2007) on *Hinode* (Kosugi et al., 2007) which are modeled with the 0D Enthalpy Based Thermal Evolution of Loops (EBTEL) framework (Klimchuk et al., 2008; Cargill et al., 2012a,b).

ARTBs are very small flaring events with thermal energy content in the range of $10^{25} - 10^{29}$ ergs, compared to the typical $10^{29} - 10^{32}$ ergs found in flares. ARTBs occur with a significantly higher frequency (1-40 events per hour per active region - Berghmans et al., 2001; Shimizu et al., 1992), which provides a large data set for analysis. Here we detect ARTBs in a small (few hours long) data set from XRT, and use models to predict the X-ray flux of the light curves to test the validity of the method.

The detection algorithm is based on the method of Berghmans & Clette (1999), which looks for enhancements in the observed flux on a pixel by pixel basis. Enhancements in neighboring pixels are then grouped together and defined as an ARTB. We use this algorithm on calibrated data from *Hinode* XRT of NOAA Active Region 11512 from 22UT on 2012 June 30 through 03:30 UT 2012 July 01. The results of the detection are then background subtracted, and strand lengths are extracted. The detections are then modeled as single- and multi-stranded loops, with each strand modeled using EBTEL. The results of this study show that multiple heating events are needed to reproduce the observed activity, and an impulsive mechanism is required for the triggering of these heating events, which strongly favors reconnection over wave triggering mechanisms.

Section 2.2.1 describes the detection method, with Section 2.2.2 detailing the parameters of the algorithm. Section 2.3 describes the multi-stranded model. In Section 2.4 we describe the data, including the details of the background subtraction in Section 2.4.1 and the estimation of strand length in Section 2.4.2. Results are discussed in Section 2.5, with particular details on the multi-stranded cases in Section 2.5.1 and the single-stranded cases in 2.5.2. We conclude with a discussion in Section 2.6 of the benefits of using the method described here to model and analyze ARTBs from the larger XRT AR catalog.

2.2. ARTB Detection

2.2.1. Method Overview

Initial ARTB detection methods (Shimizu et al., 1992) relied on visual detection of brightenings in the Geostationary Operational Environmental Satellite (GOES) X-Ray Sensor (XRS) full sun light curves, and *Yohkoh*/SXT (Tsuneta et al., 1991) image sequences, leaving many smaller but useful observations undetected. Later methods (Shimizu, 1995) automated the process by analyzing light curves of aggregations of pixels (macropixels) in SXT images looking for sharp increases in flux. Berghmans & Clette (1999) developed an improved method relying on a more automated approach to find ARTBs in SXT and EIT (Delaboudinière et al., 1995). This approach involves subtracting a running mean from the time profile of brightness in each pixel, then looking for residuals larger than a predefined threshold, typically 3 standard deviations. The automated approach allows greater sensitivity than visual inspection and provides a much more objective process of detection allowing the user to utilize a larger data set. We have adapted and optimized the method of Berghmans & Clette (1999) for the data from *Hinode*/XRT; herein we present this adapted algorithm and subsequent procedures for fitting models of the coronal structures to the observed light curves.

The first step necessary to utilize the algorithm adapted from Berghmans & Clette (1999) is to obtain an appropriate set of calibrated and aligned ARTB observations. After calibration and co-alignment, a running mean of the image stack is created by applying a temporal boxcar smoothing of width w_{rm}. This temporally smoothed version of the image is then subtracted from the original image, resulting in a residual with the mean removed.

The next step is to determine the standard deviation of the light curves for each pixel in the image stack, which is used to make a ratio between the residual and the standard deviation. The "brightest" pixel in this ratio is determined to be an ARTB as long as it is greater than q_{D}, the detection threshold. All pixels in the ratio array that are larger than a second threshold, q_{C}, are then checked for connectivity to the q_D point, with all continuously connected points denoted as part of an individual ARTB. All connected points are replaced with the value of the running mean at their location, effectively hiding the detected regions from subsequent iterations of the algorithm. The detection process then reiterates, ending when the "brightest" pixel in the ratio between the running mean subtracted residual and the standard deviation is smaller than the detection threshold.

2.2.2. Usage Parameter Overview

Not surprisingly, the efficiency of the ARTB detection algorithm is affected by the values of the constraining parameters w_{rm}, q_{D}, and q_{C}. In this section, we describe how each of these parameters affects the outcome.

The span used for calculating the running mean, w_{rm}, determines in part the sensitivity of the algorithm to secular variations in X-ray flux. This parameter sets the time scale of variations in the running mean which is subsequently removed from the original image sequence. Shorter widths, corresponding to smaller values of w_{rm}, result in shorter time scales being removed, and thus smoother residual light curves. At the extreme, a value of $w_{\mathrm{rm}} = 1$ produces a boxcar of unit width; and removal of a running mean so calculated leaves a perfectly smooth (and useless) residual. Expanding the boxcar width by use of larger w_{rm}, on the other hand, relaxes the sensitivity of the running mean to short-time-scale fluctuations, so that the running mean (the subtrahend of the residual) becomes more smooth. Subtraction of a smooth running mean results in a residual that retains much of the sensitivity to transient fluctuations. The extreme case of this is w_{rm} equal to the number of images in the data stack, such that the subtrahend is tantamount to a simple pedestal, and an equal value is subtracted from every image in the stack. In such a case, the temporal behavior of the flux is not changed at all. Thus the optimal value of w_{rm} is that which will accentuate the temporal dynamics of the system, on the time scale of the ARTBs. We have found, for the test cases considered in this study, $w_{\mathrm{rm}} = 20$ (images) yields the most consistent results which for this data set corresponds to ≈ 10 minutes.

The unitless threshold for detection, q_{D}, has a much more direct effect on the ARTB detection. Berghmans & Clette (1999) utilized a threshold of $q_{\mathrm{D}} = 3$ (i.e., detection threshold of 3 standard deviations above the pre-event mean). This value, in the test cases we have studied, resulted in an unacceptable number of spurious "false positives". This inconsistency with previous results is most likely caused by the increased sensitivity of current solar EUV and X-ray data. Testing with $q_{\mathrm{D}} = 5$

yielded detections of only the largest of ARTBs, or in some cases only flares. The most reliable results were achieved with $q_{\mathrm{D}} = 4$, although visual confirmation of the resulting light curves is still recommended.

In Berghmans & Clette (1999), the connectivity threshold q_{C} was held to the same value as q_{D}. Maintaining this equality can be expected to result in underestimating the physical extent of ARTBs where some parts of the heated structure do not reach the same brightness as the peak pixel. The 0D model used here recreates the average parameters of the strand, and so proper measurement of the size of the ARTB better measures the average flux of the observed ARTB, allowing a more accurate comparison between model and observation. In the test cases we considered, as q_{C} was increased, the size of detected ARTBs decreased, eventually becoming single-pixel detections as q_{C} approached q_{D} (with $q_{\mathrm{D}} \geq 4.0$). Conversely, relaxing q_{C} to lower values can result in many additional pixels being added into the ARTB, even though their fluxes do not increase significantly. When q_{C} was reduced below 3, very large ARTBs were logged, particularly in the final iterations of the scheme (i.e., when many data points had been reset to the median, lowering the required standard deviation threshold). For most observations $q_{\mathrm{C}} = 3$ was found to be adequate. It is worthwhile to note that at this time only a small number of data sets have been studied, and an expanded search in the future may require the re-evaluation of these parameters. After detection is complete, a 2-D spatial mask of the detected region is created containing every pixel that was flagged by the algorithm. It is then a trivial task to use this mask to extract light curves for the ARTB detections and normalize the light curves into DN/pixel/sec. An example light curve is shown in Figure 3. The light curves are then trimmed around the detected ARTB such that the first and last data points are as close to the background level as possible.

2.3. Multi-Stranded Model

After detecting ARTBs and extracting their light curves, the next step is to model each ARTB as a loop made of multiple unresolved strands. The modeling process begins by creating a single strand with the 0D EBTEL code developed in Klimchuk et al. (2008) and revised in Cargill et al. (2012b). EBTEL works by simplifying the one-dimensional time dependent energy equation for a strand into parameters that are spatially averaged across the entire length of the strand. Our observations (as discussed in Section 2.2.1) allow this simplification, as we average the flux from the entire observable ARTB. Additionally, works such as Seaton et al. (2001) have shown that ARTB loops appear to brighten in a fairly uniform fashion across the entire loop, though their results focused on EUV observations.

With the minimal input of an assumed heating function and strand length, EBTEL returns the temporal evolution of many important strand parameters, including the spatially averaged temperature, density, and pressure, as well as estimates of the differential emission measure of the chromosphere and corona. EBTEL was chosen for the present study over more complex models for the speed with which it

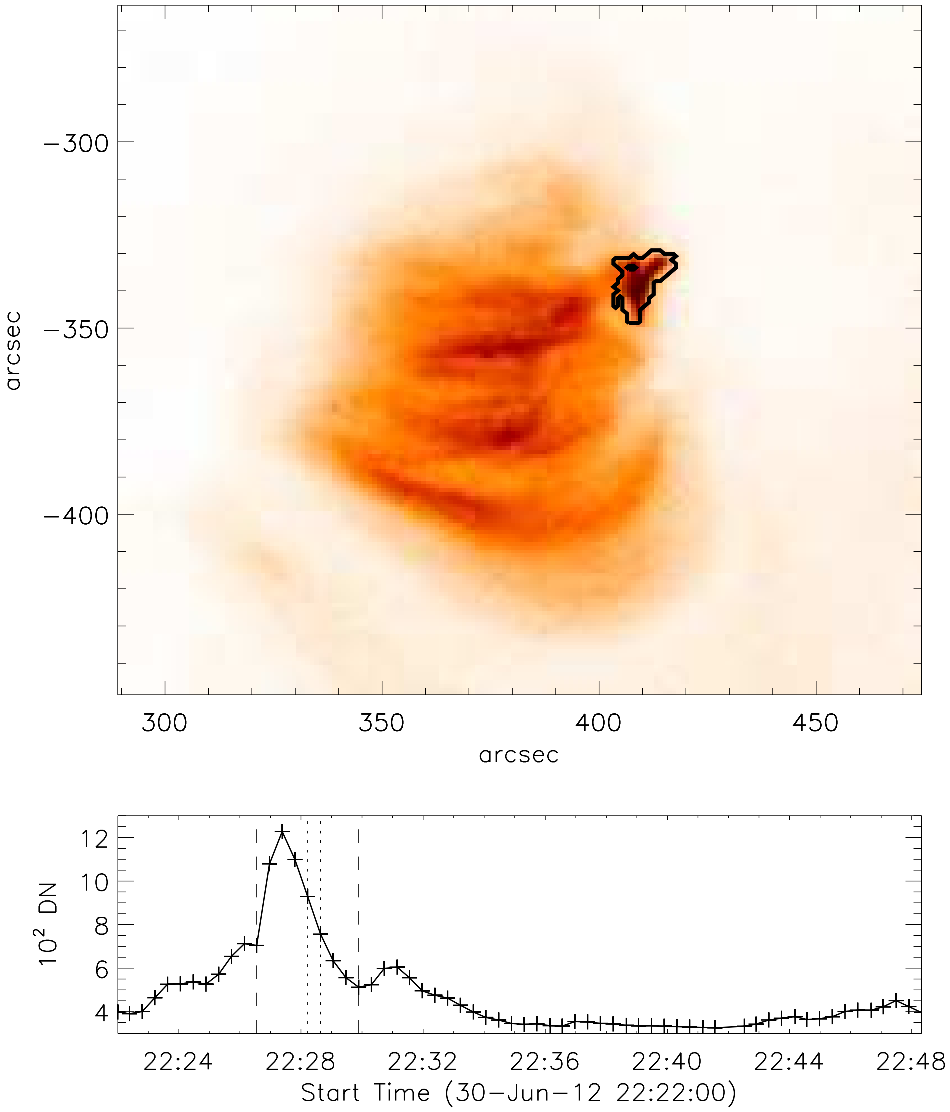

Figure 3: Example of a detected ARTB within a subframe of an XRT image. The black contour in the upper reverse color image is the detected region. The lower panel shows the light curve for the detected region over the entire time range for which the algorithm was run. The detection lasts from 02:59:47 to 03:02:42 (dotted lines), and has been manually cropped for analysis from 2:58:32 to 3:06:33 (dashed lines). As mentioned in Section 2.5, the manual cropping is performed to best isolate the complete ARTB light curve from the background.

can calculate these parameters. This speed is useful for analyzing many realizations of multi-stranded loops for each ARTB. In seconds, EBTEL is able to accomplish what a multidimensional model might take hours or even days to calculate, with only slight and predictable variations from the results of higher dimensional and more complicated models as discussed in Cargill et al. (2012a).

One of the primary inputs into the EBTEL model is the heating function. We chose the heating function for each strand to be a triangular shaped function, as can be seen in Figure 4. This heating function was chosen as a simple proxy for a δ-function, which can be used to create more complicated heating functions, such as when utilizing multiple heating events in the same strand (Section 2.5.2). The other primary input into EBTEL is the half length of the strand, $l_{\rm s}$, which we derive from the observations. It was determined through testing that using EBTEL with timesteps larger than one second when modeling individual strands caused higher peak temperature and density results, while using time steps smaller than 1s did little to change the results from EBTEL. Thus we have chosen a temporal resolution of 1s.

To calculate the column emission measure from the returned density and temperature, we assume each strand to be cylindrical with a constant diameter and axis perpendicular to the line of sight; using these parameters we can convolve the EBTEL results with a given instrument response function (for this study, XRT) to estimate an observable flux for any strand. While the actual strands may not have a constant cross-section, this study looks at the average flux across the entire strand, making the assumption of a uniform cross-section acceptable.

An arbitrary number of unique strands are then created with this method, with each strand heating at a different time. The predicted X-ray fluxes from all of the strands are then superimposed to obtain a model multi-stranded loop. For this proof-of-concept study, we have constrained the independence of individual strands such that the parameters of successive strands are related. The length of all strands in a given ARTB is held fixed, a constraint that is justified by the small size and short duration typical of ARTBs, wherein there is an absence of observational measurements of footpoint spreading, such as flare ribbon or hard X-ray footpoint motions. The delay between successive heating events, Δt, is also kept the same for all strands, such that strand $n+1$ fires at a set time after strand n, constant for all n. In the real world, Δt is almost certainly more random. It is possible a specific distribution of Δt will affect why some loops are brighter/hotter than others, a lá Parker nanoflares (Parker, 1988), but this is a level of complexity to be explored in a future study.

The amplitude of the heating function for each successive strand is varied, though the shape of the individual heating functions remain constant, as does the temporal width of the triangular pulse. For this study, we allow successive strands to heat to peaks dictated by a sinusoidal envelope and a lambda shaped envelope as shown in Figure 4. These two envelopes were chosen as they allow us to probe the likelihood of wave heating versus bursty reconnection. It would be expected that wave heating would have a gradual turn-on effect in the heating of individual strands as a particular resonance condition is met (such as with resonant absorption; i.e. Ofman et al., 1995), while bursty reconnection would predict an impulsive beginning to strand heating, followed by a slower decay in the rate of strand energization as the system reconfigures. The sinusoidal envelope is symmetric such that the first and last strands have small heating functions and the central strand has the largest heating function, with a sinusoidal shaped envelope between. The lambda shaped envelope has the first strand experiencing the largest heating event, with a linear decline for each successive strand. Each heating envelope is defined by the number of strands (n), the delay between heating events (Δt), the width of the heating pulses (w), and the peak heating rate for a strand (h_{peak}). A constant (i.e., same for all strands and time invariant) and uniform strand radius (r_{strand}) is used to provide an estimate of the volume of plasma emitting in each strand, representing an average radius for all strands in the case that the strands are not uniform.

After superimposing the flux from a given number of strands to create an aggregate light curve, the simulated light curve is compared to the XRT observation by first aligning the time of the peak fluxes. We then increase or decrease the assumed strand radius of the model until the peak fluxes are equivalent. The quality of the fit can then be easily quantified with a simple χ^2 calculation between the observed and modeled flux as shown in the tables below.

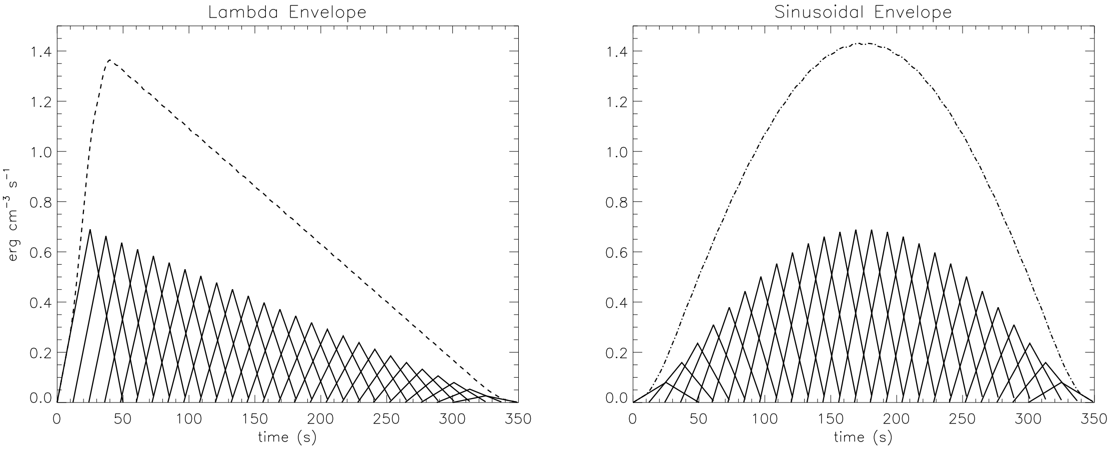

Figure 4: An example of the heating function for the case of 26 individual strands with a heating delay of 12 s, heating width of 50s and a peak heating rate of 0.69 ergs cm^{-3} s^{-1}. On the left is the lambda shaped envelope, the sinusoidal envelope on the right. The solid lines represent the individual heating events, and the dashed line is the sum of the individual events. These parameters (number of strands/heating events), Δt, heating width and peak heating rate) are varied for each realization of the model by the genetic algorithm in order to find the best fit between the combined X-ray flux of the strands and flux observed with XRT.

To find the best fit for a given observation, the genetic minimization algorithm pikaia is employed (Charbonneau, 1995). Pikaia is able to adequately and intelligently test parameter space to find the parameters (peak heating rate, width of heat pulses, delay between heating events, number of strands, and strand length) that minimize the χ^2 value between the observed and modeled flux. Pikaia was chosen over other algorithms (such as amoeba or a monte carlo minimization), as it fully samples the parameter space (unlike amoeba) while also intelligently improving its calculation with each iteration (unlike monte carlo method); thus pikaia is fairly resilient to local minima and still relatively quick.

2.4. Data

For this study, we use data from *Hinode*/XRT of NOAA Active Region 11512 from 22:18UT on 2012 June 30 through 03:35 UT 2012 July 01. These data were split into 4 subsets, separated by observational pauses for environmental conditions (such as the South Atlantic Anomaly) and orbital eclipses. Images were taken in the Ti_poly filter with a 25s cadence and calibrated using the `xrt_prep.pro` software suite discussed in Appendix A. A table of the detections analyzed from this data set can be found in Table 1. Additional ARTBs were detected but not selected for analysis due to complications in their light curves as described in Section 2.5.

2.4.1. Background Subtraction

All observations used herein contain background emission from the surrounding corona which will create extra signal on the detector, requiring the model to produce extra flux. It was found in testing that rudimentary background subtraction greatly improves the reliability and consistency of the results. It has been shown in Klimchuk et al. (1992), Schmelz et al. (2007) and Deforest & Gurman (1998) that a flat background subtraction can be effective, but can cause ambiguity as to the inferred width of loops. Our background subtraction consists of removing 80% of the lowest observed flux in the ARTB light curve, where 80% was chosen to accommodate the flux of the modeled loop existing below the observed noise floor. Since our analysis

Table 1: Information on ARTBs detected and analyzed from the XRT data set of AR 11512. The first dataset runs from 22:18UT to 22:48UT on 2012 June 30, the second from 23:25UT to 00:27UT ending on 2012 July 01, the third dataset from 00:58UT to 02:05UT on July 01, and the fourth from 02:37UT to 03:35UT on July 01.

Data Set	ARTB Number	Size of ARTB (pixels/image)	Number of Images	Average Cadence (s)
01	000	147	9	22.27
01	001	37	9	25.79
02	001	52	11	22.73
02	002	57	9	22.19
02	004	14	11	22.64
02	010	21	15	25.43
02	014	18	14	23.29
02	015	68	20	25.18
02	017	9	35	25.18
02	018	9	20	27.73
02	020	27	20	25.16
02	021	51	34	25.11
02	022	12	17	26.46
02	023	39	13	23.08
02	024	9	12	22.92
02	025	8	19	23.67
03	038	23	19	25.17
03	040	47	16	23.42
04	002	45	16	23.42
04	004	99	19	23.71
04	006	45	21	23.83
04	007	65	19	23.71
04	010	28	18	23.64
04	011	8	16	23.45
04	012	84	19	25.30
04	013	10	20	25.22
04	014	22	18	25.26
04	015	18	19	25.30
04	016	48	14	25.43
04	022	15	16	23.42
04	023	11	12	22.92
04	030	9	30	25.19
04	031	8	18	25.40
04	032	17	19	27.64

adjusts the peak flux of the model to match the peak flux of the observation by increasing the radii of the strands, the background flux estimation will have an effect on the model radius. To see this effect, let us first assume the flux of a single strand within one pixel (of width w_{pixel}) can be described by

$$\Phi_i = g_i(T_i, \rho_i) \times V_i = g_i(T_i, \rho_i) \times w_{\text{pixel}} \pi r_i^2. \tag{2.1}$$

where g_i is a function similar to the integrated emissivity of the strand at average temperature (T) and density (ρ), V_i is the volume of a single cylindrical strand of radius r_i. Thus the total emission of our ARTB will be

$$\Phi_{m0} = \sum_{i=0}^{n} \Phi_i = \sum_{i=0}^{n} g_i(T_i, \rho_i) \times w_{\text{pixel}} \pi r_i^2, \tag{2.2}$$

Our calculation initially assumes all strands are one pixel wide ($r_i = r_{\text{strand}} = \frac{w_{\text{pixel}}}{2}$) yielding an unadjusted model flux Φ_{m0}. Φ_{m0} is then scaled to match the observed (background subtracted) flux, Φ_{obs}, using the scaling factor $\xi = \Phi_{\text{obs}}/\Phi_{m0}$. We arrive at our resultant **adjusted** model flux, $\Phi_m = \xi \Phi_{m0}$. Since we are assuming a constant radius for all strands, r_{strand}, $\forall i$

$$\xi = \frac{\Phi_{\text{obs}}}{\Phi_{m0}} = \frac{2^2 r_{\text{strand}}^2}{w_{\text{pixel}}^2}. \tag{2.3}$$

Our background subtraction works such that $\Phi_{\text{obs}} = \Phi_{\text{data}} - \Phi_{\text{bg}}$, where Φ_{data} is the original signal before background subtraction, and Φ_{bg} is the estimated background signal. Some simple algebra shows that the resultant model strand radius will be:

$$r_{\text{strand}} = \frac{w_{\text{pixel}}}{2} \left(\frac{\Phi_{\text{data}} - \Phi_{\text{bg}}}{\Phi_{m0}} \right)^{\frac{1}{2}} = \frac{w_{\text{pixel}}}{2} \left(\frac{\Phi_{\text{data}}}{\Phi_{m0}} \right)^{\frac{1}{2}} \left(1 - \frac{\Phi_{\text{bg}}}{\Phi_{\text{data}}} \right)^{\frac{1}{2}}. \tag{2.4}$$

A brief expansion of the $\Phi_{\rm bg}$ parenthetical shows that

$$\begin{aligned} r_{\rm strand} \approx & \frac{w_{\rm pixel}}{2} \left(\frac{\Phi_{\rm data}}{\Phi_{m0}} \right)^{\frac{1}{2}} \\ & \times \left[1 - \frac{1}{2} \frac{\Phi_{\rm bg}}{\Phi_{\rm data}} - \frac{1}{8} \left(\frac{\Phi_{\rm bg}}{\Phi_{\rm data}} \right)^2 - \frac{3}{48} \left(\frac{\Phi_{\rm bg}}{\Phi_{\rm data}} \right)^3 + \cdots \right]. \end{aligned} \tag{2.5}$$

This illustrates that while the $\Phi_{\rm bg}$ can have a large effect on the measured radius, small changes in $\Phi_{\rm bg}$ do not. Our background subtraction provides a reasonable estimate of the base level, but small corrections to this level (such as could be found with a more sophisticated method) will not drastically change our results. Hence we determine that our method of background subtraction is sufficient, but that our estimates of strand radius should not be taken too literally.

2.4.2. Strand Length

To better constrain the parameter space searched, we have estimated the full length ($L_{\rm obs}$) for each ARTB from images of its detection. To account for 3D projection effects (among other factors), we allow the length to vary, but constrain the parameter search on strand length to stay between $L_{\rm obs}/2.5 \leq l_{\rm s} \leq 2.5 L_{\rm obs}$. The lower bound allows the strands to be slightly smaller than the observed length (note that $L_{\rm obs}$ is full length and $l_{\rm s}$ the half length). The upper bound allows the strand (if assumed to follow an elliptical arc) to be 4 times taller than it is wide, and thus most physical strand lengths are contained within our model. The added tolerance for smaller and larger lengths allows a sanity check on our results.

2.5. Results and Analysis

After calibrating the data, the spacecraft pointing jitter was removed and an iterative cross-correlation algorithm was employed individually to each of the 4 datasets to further co-align the data. The datasets were then passed through the ARTB detection algorithm, which resulted in 10 detections in the first dataset (from 22:18UT to 22:48UT), 32 detections in the second (from 23:25UT to 00:27UT), 51 detections in the third (from 00:58UT to 02:05UT), and 33 detections in the fourth (from 02:37UT to 03:35UT). We manually cropped the light curves so that they begin and end as near to the lowest observed flux level as possible, as shown in Figure 3.

Upon visual inspection of the extracted light curves, only a few of these detections were found to be problematic. One type of problematic detection involves coherent spikes in the quiet regions surrounding an active region. Since these detections are not valid ARTBs and we cannot easily determine whether these signals are quiet sun brightenings or instrument noise, they are not analyzed. Another source of problematic detections are events for which flux enhancements in the light curves overlap in time, creating a more complicated profile. These events have slightly different spatial footprints, but overlapping light curves. This overlap adds a level of complexity to the analysis that we determined was not suitable for a proof-of-concept study such as this, and as such do not analyze these ARTBs here. In addition, some of the detected ARTBs spanned fewer than 7 images, and thus are over-constrained by our model. This concept of over-constraint plays an important role in the simplifications used in our model. Increasing the complexity of the model would increase the number of parameters used by the model and thus the number of time steps required for analysis, further decreasing the number of useable observations. Removing the spurious, over-constrained and multi-peaked detections, we are left with 44 ARTBs for analysis, 34 of which were successfully modeled. Only those that were successfully modeled are shown in Table 1.

We then used pikaia with our multi-stranded model and both (sinusoidal and lambda) heating envelopes to determine the parameters which best fit each ARTB. We allowed the peak heating function to vary from 0.2 to 1.0 ergs cm^{-3} s^{-1}, the width of the heating pulse to vary between 2 and 50s (in one second intervals), the delay between successive heating events to vary between 1 and 20s, the number of strands to vary between 1 and 500, and the strand half-length to vary between $L_{\text{obs}}/2.5 \leq l_s \leq 2.5L_{\text{obs}}$ as discussed in Section 2.4.2. We have also fit the data with a single strand, both by using a single impulsive heating event and multiple heating events. When considering multiple heating events in a single strand, we have confined our search to using the lambda envelope to constrain the individual heating events, such as represented by the dashed lines in Figure 4. An overview of all of the results are shown in Table 2.

2.5.1. Multi-Stranded Results

We have modeled 44 detected ARTBs using both the sinusoidal and lambda envelopes. Example fits can be found in the green and blue lines in Figure 5 and

Table 2: Overview of fitting results from using all envelopes.

Data Set	ARTB Number	χ^2 (DN) Sinusoidal	χ^2 (DN) Lambda	χ^2 (DN) Lambda (Mono)	χ^2 (DN) Single Strand
01	000	22.34	11.49	776.24	874.65
01	001	90.78	3.82	5.68	12.41
02	001	12.55	16.22	36.41	135.70
02	002	27.05	648.49	196.02	359.19
02	004	46.57	733.45	94.66	210.79
02	010	15.92	62.41	103.69	72.13
02	014	97.09	51.11	2.94	504.65
02	015	269.59	63.72	10.62	107.94
02	017	1682.60	33.64	25.40	87.57
02	018	24.05	31.32	31.75	87.69
02	020	68.40	15.34	17.33	111.64
02	021	26.94	26.02	6.03	67.27
02	022	230.15	30.83	8.54	85.92
02	023	38.37	12.32	6.85	57.64
02	024	60.84	13.43	6.91	27.41
02	025	30.20	33.48	21.43	13.16
03	038	36.78	26.93	6.11	72.17
03	040	41.08	172.44	13.62	301.73
04	002	24.32	61.26	22.84	17.54
04	004	87.82	8.52	29.74	399.09
04	006	30.74	37.69	16.09	103.78
04	007	28.64	23.30	12.60	215.38
04	010	8.96	5.16	45.02	388.82
04	011	35.69	25.11	4.77	613.44
04	012	16.16	118.33	16.15	7.58
04	013	5.25	62.48	73.25	67.22
04	014	20.96	26.88	19.09	19.01
04	015	70.99	26.01	24.55	20.69
04	016	12.88	189.53	15.98	83.55
04	022	122.17	83.69	43.55	83.15
04	023	170.25	49.75	42.78	79.27
04	030	20.58	61.93	5.63	105.19
04	031	38.08	42.21	63.25	81.15
04	032	65.66	102.10	31.16	161.86

Appendix B. Tables 3 and 4 show the results of the multi-stranded runs. In general (but not in every case), the lambda envelope resulted in lower χ^2 values in the best fits than the sinusoidal envelope. Even though the χ^2 minimization provides a good method for comparing fits when modeling a single ARTB observation, it is limited when comparing results from different observed ARTBs. We have found that comparing the ratio of the integrated flux of the model to that of the observation provides a very good proxy for the quality of the individual results. Visual inspection of the results found that good fits exist when this ratio is between 0.95 and 1.06, but acceptable fits can exist with larger or smaller values. These tests indicated 34 of the 44 ARTBs were acceptably modeled with the both the lambda and sinusoidal envelope.

When considering those ARTBs that could be fit with these envelopes, the lambda envelope results used a median value of 23 strands with 17s wide heating pulses to fit the observations, while the sinusoidal envelope required 31 strands each being heated for 21.5s (average value for all results). On average, the results for the other parameters were similar for both envelopes. The best fit for the lambda envelope resulted in a single strand only once, for ARTB 25 in dataset 2 (shown in the lower left of Figure 5), giving a good visual fit. This illustrates the benefit of such a statistical study: by viewing the results of many runs, it is possible to identify such a result as an outlier, instead of interpreting this as proof of singly heated monolithic loops. On average for the good fits, the χ^2 values for the lambda envelope were

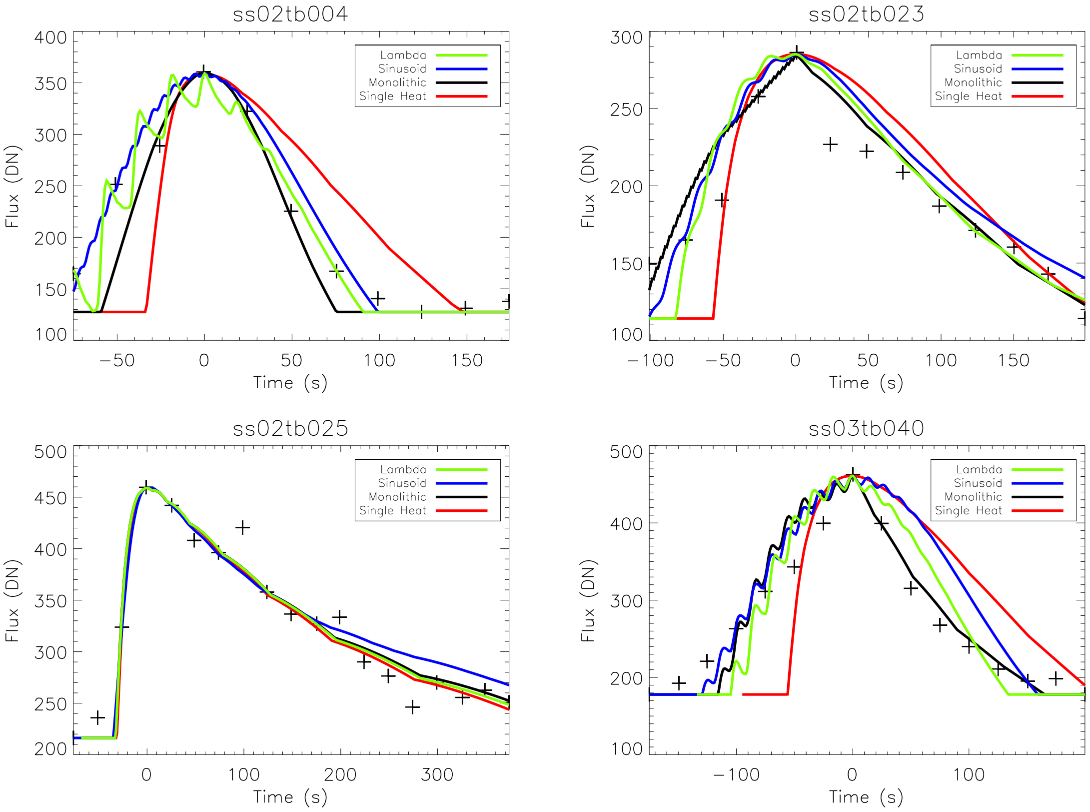

Figure 5: Representative fits from 4 ARTBs. Crosses represent the observed light curves after background subtraction. The green and blue lines represent the best fit for the multi-stranded models using the lambda and sinusoidal envelopes respectively. The red line represents the best fit using a single strand heated a single time. The black line represents a single strand heated multiple times using the lambda envelope. The upper left is ARTB 4 from dataset 2; upper right ARTB 23 from dataset 2; lower left ARTB 25 from dataset 2; and the lower right is ARTB 40 from dataset 3. These results show the improvement from using the lambda shaped envelope with either a single strand or a multi-stranded loop. The lower left shows a unique case where a single heating event in one strand can give comparable results to more complex models. More fits and temperatures can be found in Appendix B.

48% lower than the sinusoidal χ^2, suggesting a significant improvement with the lambda envelope. The suggested strand radius is of order 0.5” for both envelopes, which is slightly larger than expected, though given our rudimentary and minimal background subtraction is not unacceptable. A few results returned unreasonably large strand radii (notably ARTBs 2 and 14 in dataset 2). A possible cause of these large radii is the removal of too small of a background signal. These large radius results accompany low peak heating rates and somewhat large values of their integral ratio suggesting these cases are not well fit by the model and could be readily and consistently flagged.

A desired goal for this and future studies is to search for correlations between the parameters giving the best fits. When looking at the relations between parameters, Δt and n have the only notable correlation, as shown in Figures 6 and 7. A Spearman rank order correlation between Δt and n shows correlation coefficients of -0.8344 and -0.6736 for the sinusoidal envelope and lambda envelopes respectively. The chance probabilities for these distributions are less than 0.01%, suggesting that these parameters are correlated. One should expect some relation between Δt, n, and w, as combined they dictate the total width of the heating envelope, though no monotonic relation between these parameters was found. In fact, when looking at the total integrated heat input, no notable correlations were seen, except for a relation with strand radius. This is an expected relation; if more energy is deposited, the strands will be brighter, and thus a smaller strand radius is necessary to match the observations (as suggested by the Equations of Section 2.4.1). Additionally, the median value of 31 strands and 23 strands for the sinusoidal and lambda envelopes (respectively) show a preference for a small number of strands (but generally more than one).

Table 3: Best fit results from the using the Sinusoidal Envelope.

Data Set	ARTB Number	χ^2 (DN)	Peak Heating (ergs/cm^3/s)	Heat Pulse Width (s)	Event Delay (s)	Number of Strands	Half-Length Observed (Mm)	Half-Length Result (Mm)	Strand Radius (Mm)	Integral Ratio
01	000	1682.60	0.219	16	01	350	8.57	2.26	0.542	1.267
01	001	26.94	0.865	22	16	002	6.78	7.44	0.513	1.075
02	001	30.20	0.316	04	07	014	4.91	2.44	3.428	0.884
02	002	230.15	0.419	47	01	169	6.18	5.09	0.068	1.172
02	004	15.92	0.799	07	06	034	2.97	2.75	0.509	1.034
02	010	24.05	0.659	33	19	027	5.37	10.59	0.135	1.012
02	014	97.09	0.943	26	19	010	4.24	3.40	0.369	1.001
02	015	38.37	0.730	19	01	396	8.58	9.39	0.037	1.038
02	017	269.59	0.622	06	14	016	4.03	14.74	1.230	0.946
02	018	60.84	0.404	15	11	030	5.37	16.63	0.394	1.026
02	020	68.40	0.880	17	17	020	7.83	6.27	0.257	0.978
02	021	27.05	0.357	08	06	077	12.20	25.92	0.576	1.028
02	022	30.74	0.661	05	05	125	6.49	7.02	0.379	1.042
02	023	35.69	0.888	12	17	015	6.68	8.43	0.362	1.083
02	024	20.96	0.653	45	04	054	3.59	3.31	0.080	0.972
02	025	20.58	0.453	06	11	006	6.97	17.44	2.544	1.016
03	038	38.08	0.929	09	19	012	5.22	10.04	0.513	1.030
03	040	90.78	0.591	03	14	026	5.30	4.63	1.778	1.089
04	002	16.16	0.257	35	09	024	6.46	9.04	0.325	0.955
04	004	70.99	0.789	27	18	031	8.36	7.11	0.148	1.034
04	006	122.17	0.710	05	12	025	7.54	7.32	0.818	1.025
04	007	28.64	0.969	15	16	026	9.48	7.82	0.224	0.983
04	010	46.57	0.685	35	08	042	5.42	9.21	0.114	1.001
04	011	170.25	0.958	49	01	301	8.46	7.52	0.026	1.066
04	012	5.25	0.406	12	19	013	8.96	20.46	0.617	0.990
04	013	12.88	0.342	32	06	083	5.37	14.58	0.147	1.024
04	014	8.96	0.443	29	01	223	6.65	16.27	0.063	0.997
04	015	22.34	0.592	35	03	078	4.84	16.86	0.067	1.033
04	016	12.55	0.918	49	02	325	7.75	6.20	0.018	1.042
04	022	36.78	0.761	24	19	014	5.34	9.28	0.260	1.023
04	023	24.32	0.454	25	15	019	3.56	5.01	0.396	1.036
04	030	65.66	0.615	13	01	285	4.89	17.64	0.091	0.986
04	031	41.08	0.348	15	03	114	4.47	12.52	0.291	1.033
04	032	87.82	0.602	13	15	046	7.01	7.06	0.407	1.070

Table 4: Best fit results from the using the Lambda Envelope.

Data Set	ARTB Number	χ^2 (DN)	Peak Heating (ergs/cm^3/s)	Heat Pulse Width (s)	Event Delay (s)	Number of Strands	Half-Length Observed (Mm)	Half-Length Result (Mm)	Strand Radius (Mm)	Integral Ratio
01	000	648.49	0.997	32	14	005	8.57	6.86	0.346	1.327
01	001	733.45	0.610	03	15	010	6.78	2.93	2.380	0.940
02	001	26.93	0.455	02	01	096	4.91	3.98	2.085	1.076
02	002	172.44	0.332	02	19	007	6.18	4.96	10.832	1.222
02	004	5.16	0.804	08	19	008	2.97	2.61	1.119	0.977
02	010	25.11	0.200	14	17	033	5.37	5.96	1.332	1.029
02	014	83.69	0.365	02	15	009	4.24	4.79	13.274	1.062
02	015	49.75	0.997	49	02	176	8.58	10.44	0.020	1.082
02	017	62.41	0.389	05	01	103	4.03	20.12	0.898	1.011
02	018	51.11	0.490	10	06	033	5.37	13.30	0.606	1.030
02	020	63.72	0.640	20	19	010	7.83	6.61	0.483	0.990
02	021	33.64	0.263	16	05	081	12.20	22.18	0.474	1.024
02	022	31.32	0.880	02	18	021	6.49	10.10	2.105	1.080
02	023	30.83	0.860	17	19	008	6.68	8.40	0.368	1.043
02	024	12.32	0.841	21	16	008	3.59	4.50	0.342	0.999
02	025	13.43	0.356	08	01	001	6.97	17.28	4.179	1.002
03	038	33.48	0.484	22	07	023	5.22	8.05	0.394	1.021
03	040	61.26	0.526	06	17	013	5.30	4.24	2.055	1.027
04	002	8.52	0.271	45	04	045	6.46	11.09	0.207	1.005
04	004	118.33	0.475	04	16	023	8.36	7.39	2.092	1.039
04	006	62.48	0.309	20	01	174	7.54	6.41	0.263	0.995
04	007	26.88	1.000	49	06	062	9.48	7.92	0.055	0.992
04	010	26.01	0.393	06	16	028	5.42	4.64	2.079	0.994
04	011	189.53	0.989	33	15	015	8.46	6.80	0.193	1.059
04	012	3.82	0.352	11	01	163	8.96	22.71	0.242	1.000
04	013	16.22	0.867	09	11	076	5.37	4.30	0.367	1.013
04	014	11.49	0.861	15	02	085	6.65	16.89	0.118	1.006
04	015	15.34	0.997	27	01	150	4.84	15.69	0.045	1.001
04	016	26.02	0.975	04	19	019	7.75	7.50	0.856	1.052
04	022	37.69	0.735	22	14	018	5.34	7.54	0.326	1.045
04	023	23.30	0.722	23	19	010	3.56	6.20	0.394	1.031
04	030	61.93	0.855	08	01	241	4.89	17.15	0.154	1.010
04	031	42.21	0.593	11	15	017	4.47	11.85	0.692	1.041
04	032	102.10	0.281	13	19	023	7.01	7.29	1.307	1.050

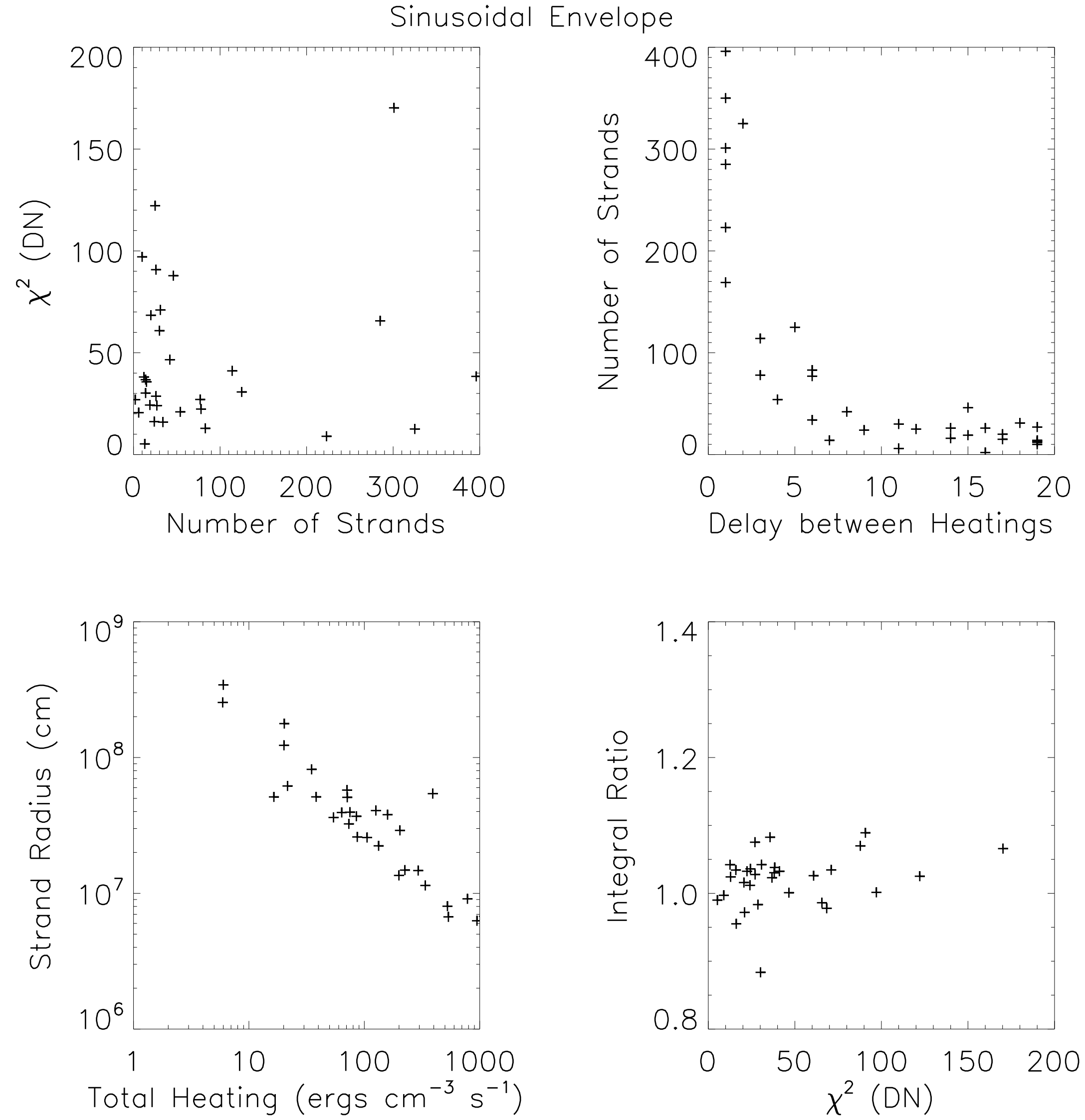

Figure 6: Scatter plots for best multi-stranded fits using a sinusoidal envelope: χ^2 versus number of strands (n: top left), heating delay (Δt) versus n (top right), total integrated heating versus strand radius (r_{strand}: bottom left), and χ^2 versus ratio of integrated flux (bottom right). For the relation between Δt and n, the sinusoidal envelope shows a Spearman correlation coefficient of -0.8344 with a chance probability of less than 0.01%. These comparisons suggest a very strong relation between Δt and n. The relation between strand radius and input heating is shown. The scatter in the integral ratio plot shows the benefit of using the integral ratio technique to compare results between ARTBs. The other parameter relations (not shown) did not show useful relationships with so few data points.

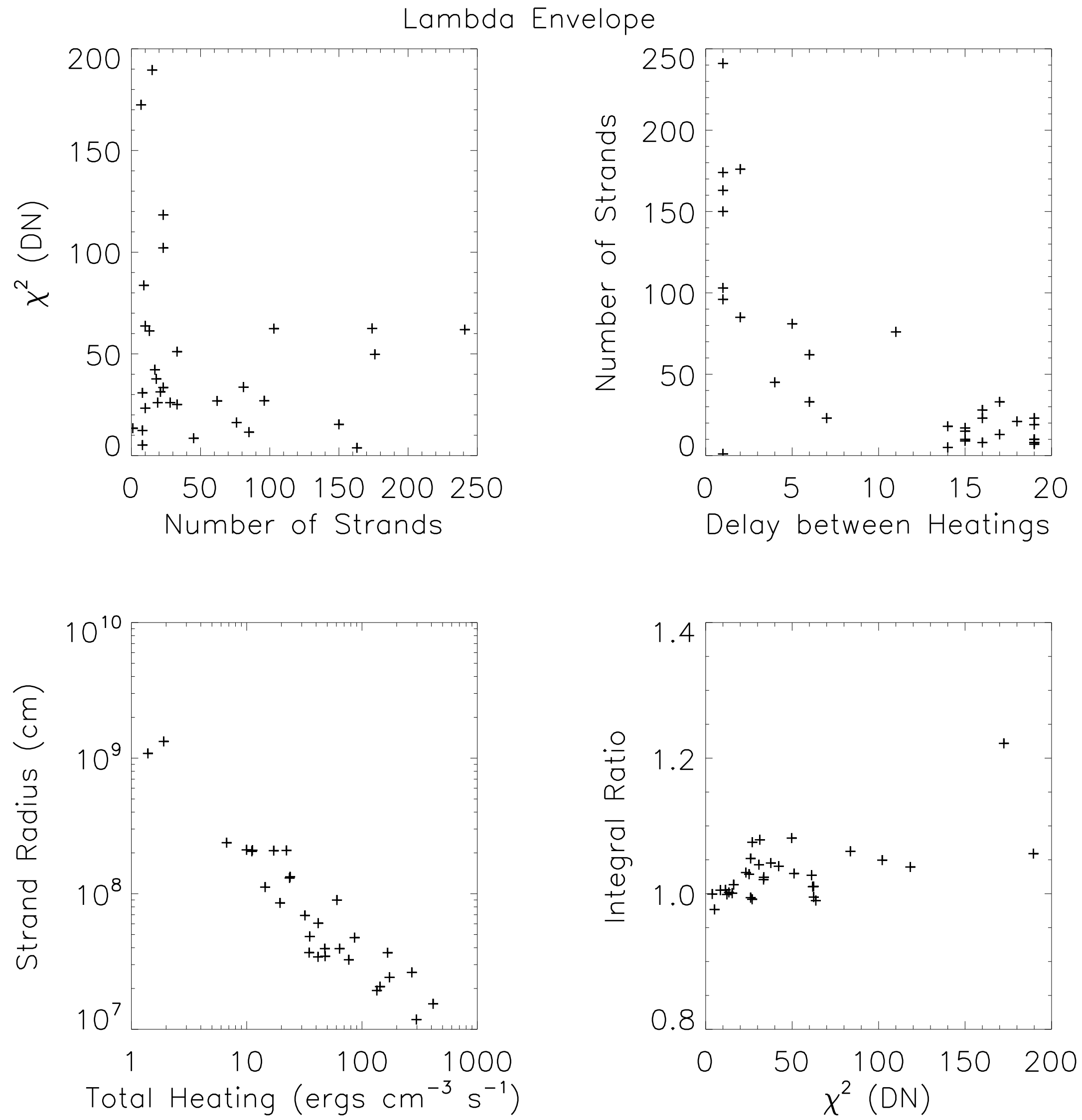

Figure 7: Scatter plots for best multi-stranded fits using a lambda envelope, the layout is the same as Figure 6. For the relation between Δt and n, the lambda envelope shows a Spearman correlation coefficient of -0.6736 with a chance probability of less than 0.01%. These comparisons suggest a very strong relation between the Δt and n. As should be expected, there is a relation between strand radius and input heating, as more input heating will mean a brighter strand and thus a smaller radius is required.

2.5.2. Single Strand Results

We have also tested the capability of using a single strand to match the observations. This process was performed with the same method as the multi-stranded results, but the number of strands was fixed to one. We tested using a single triangular heating event and multiple heating events contained with the lambda envelope discussed earlier (see Figure 4). Examples of the fits are shown by the red and black lines in Figure 5. For the case of a single strand heated once, the χ^2 values in Table 5 show that while in a few cases, the single strand heated once can properly match the observations, as a whole, the dynamics of the energization are too complex to be rectified with a single heating event in a 0D strand. The χ^2 and integral ratio for the singly heated fits are consistently larger than for other cases.

In addition to using a single strand with a single impulsive heating event, we have also matched the observations to a single strand with multiple heating events. This is done to test the usefulness of having independently cooling structures. Since the sinusoidal envelope was consistently less capable, we used the lambda heating envelope and constrained all the heating to occur within a single strand. These results (Table 6 and Figure 8) are quite interesting: while a single strand heated just once was unable to mimic the observations, a single strand heated multiple times performed similarly (and sometimes better) than multiple independent strands. This promotes the tendency of the multi-stranded cases to favor fewer strands. The best-fit single strand cases had a median of 24 heating events.

Table 5: Best fit results from the using a single strand heated only once.

Data Set	ARTB Number	χ^2 (DN)	Peak Heating (ergs/cm^3/s)	Heat Pulse Width (s)	Half-Length Observed (Mm)	Half-Length Result (Mm)	Strand Radius (Mm)	Integral Ratio
01	000	874.65	0.994	49	8.57	7.43	0.335	1.410
01	001	12.41	0.854	34	6.78	5.94	0.338	0.995
02	001	135.70	0.999	49	4.91	5.08	0.204	1.140
02	002	359.19	0.997	49	6.18	8.38	0.234	1.305
02	004	210.79	0.999	49	2.97	5.51	0.218	1.064
02	010	72.13	0.995	48	5.37	18.33	0.220	1.076
02	014	504.65	0.997	49	4.24	5.41	0.339	1.038
02	015	107.94	0.996	49	8.58	11.52	0.141	1.034
02	017	87.57	0.927	02	4.03	20.12	6.557	0.987
02	018	87.69	0.612	03	5.37	13.69	3.766	1.007
02	020	111.64	0.980	49	7.83	8.90	0.225	1.000
02	021	67.27	0.947	31	12.20	25.79	0.354	1.043
02	022	85.92	0.795	46	6.49	23.84	0.270	1.118
02	023	57.64	0.998	49	6.68	8.76	0.200	1.059
02	024	27.41	0.999	49	3.59	6.03	0.201	1.012
02	025	13.16	0.494	05	6.97	16.72	4.008	0.993
03	038	72.17	0.969	45	5.22	9.83	0.256	1.036
03	040	301.73	0.998	49	5.30	8.48	0.253	1.124
04	002	17.54	0.997	49	6.46	11.71	0.207	1.030
04	004	399.09	0.877	43	8.36	22.56	0.280	1.196
04	006	103.78	1.000	49	7.54	11.42	0.224	1.001
04	007	215.38	0.993	49	9.48	14.35	0.227	1.063
04	010	388.82	0.999	49	5.42	13.88	0.251	1.100
04	011	613.44	0.999	49	8.46	11.70	0.287	1.159
04	012	7.58	0.305	31	8.96	19.55	0.776	1.014
04	013	67.22	0.964	49	5.37	19.54	0.218	1.075
04	014	19.01	0.801	22	6.65	15.55	0.497	1.002
04	015	20.69	0.423	45	4.84	14.89	0.450	0.987
04	016	83.55	0.922	40	7.75	23.66	0.216	1.144
04	022	83.15	0.976	49	5.34	8.99	0.248	0.998
04	023	79.27	0.991	49	3.56	8.87	0.246	1.055
04	030	105.19	0.814	19	4.89	18.64	0.571	1.036
04	031	81.15	0.999	49	4.47	15.61	0.244	1.087
04	032	161.86	0.745	12	7.01	11.47	1.283	1.019

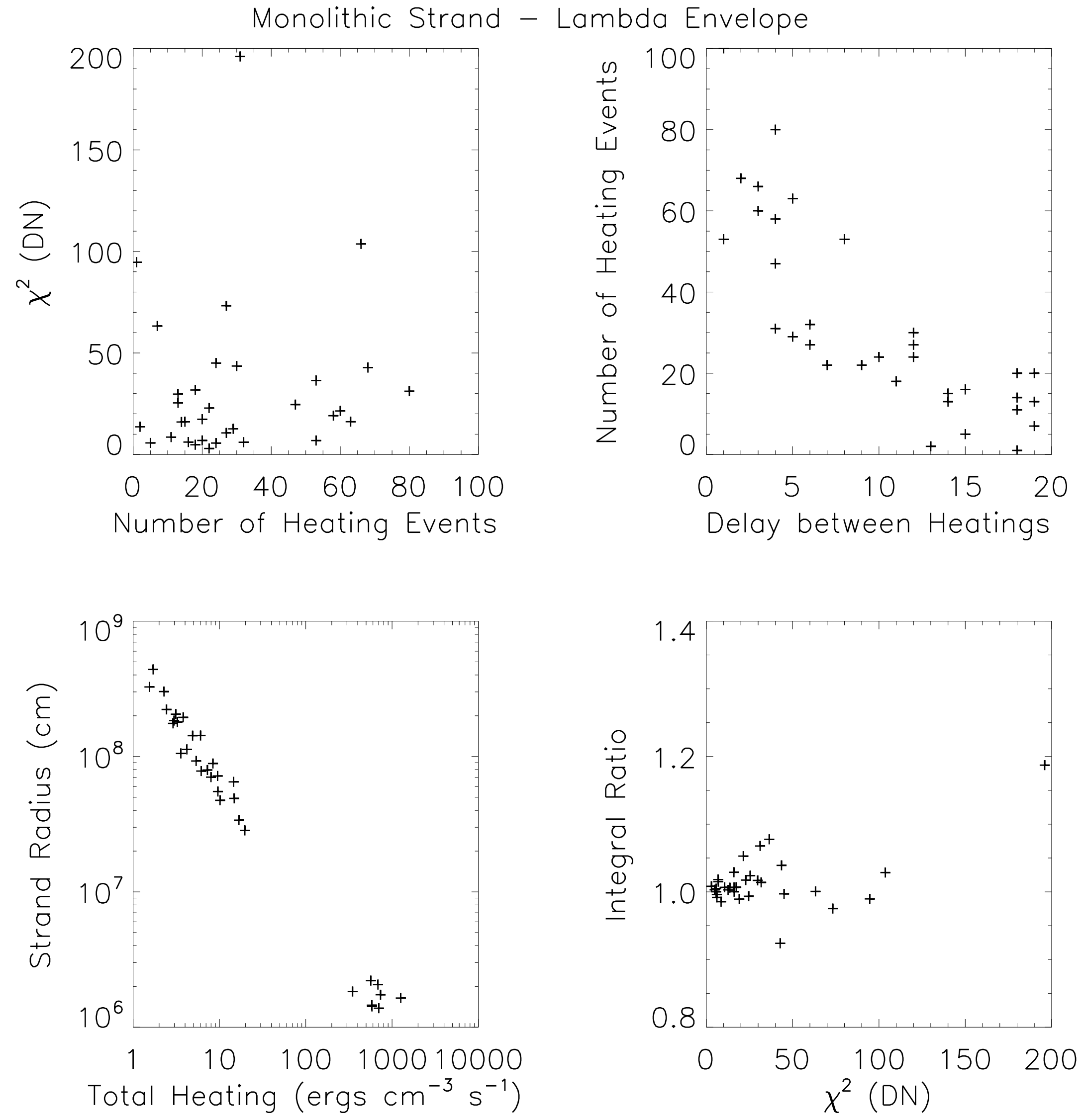

Figure 8: Scatter plots for best single strand fits with a lambda heating envelope, the layout is the same as Figure 6. In this case, the relation between Δt and n has a Spearman coefficient of -0.8819 with a chance probability of less than 0.01%. As expected, the strand radius is strongly correlated to the total heating input into the strand.

Table 6: Results from the using a single strand with multiple heating events (lambda envelope).

Data Set	ARTB Number	χ^2 (DN)	Peak Heating (ergs/cm^3/s)	Heat Pulse Width (s)	Event Delay (s)	Number of Heatings	Half-Length Observed (Mm)	Half-Length Result (Mm)	Strand Radius (Mm)	Integral Ratio
01	000	776.24	0.999	49	01	100	8.57	8.18	0.016	1.381
01	001	5.68	0.299	12	15	005	6.78	6.46	0.926	1.005
02	001	36.41	0.983	43	01	053	4.91	4.68	0.014	1.078
02	002	196.02	0.200	05	04	031	6.18	5.89	0.718	1.187
02	004	42.78	0.969	41	02	068	2.97	2.83	0.014	0.924
02	010	5.63	0.237	02	12	024	5.37	9.89	1.843	1.000
02	014	63.25	0.609	12	19	007	4.24	4.21	0.649	1.001
02	015	31.16	0.958	18	04	080	8.58	11.99	0.018	1.068
02	017	94.66	0.359	05	18	001	4.03	20.12	6.766	0.990
02	018	25.40	0.214	02	19	013	5.37	15.42	3.264	1.024
02	020	31.75	0.200	03	11	018	7.83	9.91	1.946	1.014
02	021	17.33	0.200	02	18	020	12.20	28.16	2.226	1.007
02	022	6.91	0.200	04	19	020	6.49	13.92	1.127	1.015
02	023	21.43	0.200	02	03	060	6.68	9.24	0.781	1.053
02	024	6.11	0.874	04	15	016	3.59	3.44	0.490	0.992
02	025	13.62	0.601	03	13	002	6.97	17.60	4.397	1.006
03	038	22.84	0.278	02	07	022	5.22	9.23	1.799	1.017
03	040	29.74	0.200	11	14	013	5.30	5.95	0.888	1.017
04	002	4.77	0.202	09	11	018	6.46	11.82	0.551	1.003
04	004	16.15	0.205	06	05	063	8.36	8.64	0.284	1.007
04	006	73.25	0.200	11	06	027	7.54	11.08	0.338	0.975
04	007	19.09	0.997	49	04	058	9.48	11.96	0.017	0.989
04	010	24.55	0.984	47	04	047	5.42	10.98	0.022	0.994
04	011	103.69	0.975	42	03	066	8.46	8.06	0.021	1.029
04	012	2.94	0.306	02	09	022	8.96	20.67	1.053	1.008
04	013	10.62	0.241	06	12	027	5.37	15.72	0.475	1.007
04	014	6.03	0.242	03	06	032	6.65	16.16	0.704	0.996
04	015	8.54	0.606	03	18	011	4.84	15.93	0.794	0.985
04	016	6.85	0.899	48	08	053	7.75	10.20	0.015	1.018
04	022	16.09	0.591	02	14	015	5.34	7.07	1.426	1.000
04	023	12.60	0.202	03	05	029	3.56	5.69	1.428	1.003
04	030	45.02	0.200	02	10	024	4.89	18.84	1.756	0.997
04	031	15.98	0.263	02	18	014	4.47	13.13	3.020	1.029
04	032	43.55	0.200	02	12	030	7.01	12.92	2.054	1.039

2.6. Conclusion

We were able to successfully forward model 34 ARTBs observed with XRT as multi-stranded and single-stranded structures using the 0D model EBTEL. We varied the heating rate (spatially via multiple strands and temporally with multiple strands and heating events) to study the energy deposition in these small brightenings. An overview of the results is found in Table 2. It was found that for most events, multiple heating events were required. For a multi-stranded system heated with a sinusoidal envelope, a median of 31 strands were required to reproduce the observations. For the lambda envelope, the multi-stranded cases used a median of 23 strands, and the single strand cases used a median of 24 heating events to reproduce the observed ARTB evolution.

Additionally, we were able to show that a symmetric (sinusoidal) envelope to the heating was not as capable as a more impulsive envelope. This supports the concept of a “triggering” mechanism to these events, wherein something causes a quick burst of heating to these structures, and then quickly fades, as opposed to a more uniform build up and decline to the heating. This tendency towards asymmetric (in time) energization appears to be consistent with the abrupt deposition of energy one might expect from a reconnection-related micro-flaring scenario. On the other hand, wave-heating scenarios, wherein energy is deposited in the coronal loop via a gradually developing resonance within the loop, might be expected to “switch on” less abruptly, and thus may favor the sinusoidal heating profile. The frequency with which the lambda or sinusoidal heating profile achieves a better fit to the observed ARTBs, which may yield inferences regarding the relative importance of reconnection- versus wave-heating, will be addressed by a future study involving a much larger catalog of ARTBs. The present proof-of-concept study serves to introduce the methodology and demonstrate its abilities and limitations in modeling the ARTBs.

One thing we were not able to discern is whether these events require multiple structures in the cross-section perpendicular to the loop axis or if the observed evolution is caused by multiple heating events within a single structure. If considering these events to be the result of braided loops heated by reconnecting braids (causing the braids to re-configure in a less twisted fashion), it is likely that each strand reconnects multiple times before the system stabilizes in a less twisted state, and thus multiple heating events for each strand should be expected. An important distinction between the multi- and single-stranded cases is whether a strand is allowed to cool completely after individual heating events. The multi-stranded cases represent the extreme end of low frequency heating, where the strand is allowed to cool completely before being heated again. The single-stranded cases allow high frequency heating (minimal cooling before being heated again) as well as low frequency heating. Our single-strand results favor high frequency heating, but since we cannot yet find a preference for the multi-strand or single-strand results, we cannot yet reliably determine the frequency of heating for these events, similar to the results found in Guennou et al. (2013).

It would be very useful to understand better the number and frequency of heating events each strand experiences. In the case of multi-stranded loops, however, adding the ability for each strand to experience multiple heating events runs the risk of over-constraining the system, i.e. it would require more parameters than data points for each observation. It is difficult to properly constrain the model using multiple strands heated multiple times without over constraining the data: the model would have to constrain both the number of heating events per strand and the envelope between them in addition to the envelope between individual strands used here. It is our hope that this and future studies will help to constrain the models such that it will be possible to adequately test the effects of multiple strands heated multiple times. Additionally, since our results cannot yet distinguish between the multi-stranded singly heated and single-strand with multiple heating events, it is difficult to justify that this method as currently implemented would be able to distinguish the models shown here with the case of multiple strands heated multiple times. The next step in approaching this level of complexity will be to find many more ARTBs in the XRT data catalog and model them to more rigorously constrain the requirements on the number of strands (and heating events) necessary.

2.7. Acknowledgements

Hinode is a Japanese mission developed and launched by ISAS/JAXA, collaborating with NAOJ as a domestic partner, and with NASA and STFC (UK) as international partners. Scientific operation of the *Hinode* mission is conducted by the *Hinode* science team organized at ISAS/JAXA. This team mainly consists of scientists from institutes in the partner countries. Support for the post-launch operation is provided by JAXA and NAOJ (Japan), STFC (U.K.), NASA, ESA, and NSC (Norway). This work was partially supported by NASA under contract NNM07AB07C with the Smithsonian Astrophysical Observatory.

3. FORWARD MODELING TRANSIENT BRIGHTENINGS AND MICROFLARES AROUND AN ACTIVE REGION OBSERVED WITH HI-C

Contribution of Authors and Co–Authors

Manuscript in Chapter 3

Author: Adam R. Kobelski

Contributions: Conceived and implemented study design. Wrote first draft.

Co–Author: David E. McKenzie

Contributions: Helped to conceive study. Provided feedback of analysis and comments on drafts of the manuscript.

Manuscript Information Page

Adam R. Kobelski, David E. McKenzie
The Astrophysical Journal
Status of Manuscript:
____Prepared for submission to a peer–reviewed journal
_x_ Officially submitted to a peer–reviewed journal
____Accepted by a peer–reviewed journal
____Published in a peer–reviewed journal

Submitted April, 2014, The Astrophysical Journal

ABSTRACT

Small scale flare-like brightenings around active regions are among the smallest and most fundamental of energetic transient events in the corona, providing a testbed for models of heating and active region dynamics. In a previous study, described in Chapter 2, we modeled a large collection of these microflares observed with *Hinode*/XRT using EBTEL and found that they required multiple heating events, but could not distinguish between multiple heating events on a single strand, or multiple strands each experiencing a single heating event. We present here a similar study, but with EUV data from the High Resolution Coronal Imager (Hi-C) sounding rocket. Hi-C provides an order of magnitude improvement to the spatial resolution of XRT, and a cooler temperature sensitivity, which combine to provide significant improvements to our ability to detect and model microflare activity around active regions. We have found that at this resolution, the events occur much more frequently than expected, and are most likely made from strands of order 100 km wide, each of which is impulsively heated with multiple heating events. These findings tend to support bursty reconnection as the cause of the energy release responsible for the brightenings.

3.1. Introduction

The heating of active regions can be considered in two forms: the large impulsive heating (Reeves & Warren, 2002) seen in solar flares, and a more constant background heating. While it is fairly standard to associate flaring events to magnetic reconnection (*e.g.*: Forbes & Acton, 1996; Shibata, 1999; Fletcher et al., 2001; Yokoyama et al., 2001; Qiu et al., 2010), the source of the background heating is more hotly debated. One dominant discussion is the existence of small “nanoflares” as the source of this heating (Parker, 1988; Klimchuk, 2006, among others) which act as flares on much smaller (spatial, temporal, and energetic) scales.

One of the most sought after signatures of nanoflare heating is the existence of high temperature (>10 MK) plasma in quiescent active regions. There has been evidence for this high temperature component in data from the Ramaty High Energy Solar Spectroscopic Imager (RHESSI, McTiernan, 2009), the *Hinode*/X-Ray Telescope (XRT, Reale et al., 2009; Schmelz et al., 2009), and Atmospheric Imaging Assembly (AIA) onboard the Solar Dynamics Observatory (SDO, Viall & Klimchuk, 2011), often using proxies of the differential emission measure (DEM) to estimate the spectral components of the observed plasma. However, this hot component as applied to nanoflare heating has been difficult to find with spectral observations from *Hinode*/Extreme Ultraviolet Imaging Spectrometer (EIS, Warren et al., 2012) or High Resolution Coronal Imager (Hi-C, Winebarger et al., 2013).

While nanoflare heating may not be the sole source of heating in active regions, small flaring events (sometimes referred to as microflares) are quite readily visible. Below the GOES flare detection and labeling threshold, the frequency of coronal flare-like brightenings around active regions is quite large (as many as 40 events per hour per active region, Berghmans et al., 2001; Shimizu et al., 1992). The rate of occurrence of these brightenings tends to increase as the energies involved decrease (down to the noise floor of the instrument used), though not necessarily at a rate sufficient to heat the corona by nanoflare heating (Hudson, 1991; Berghmans, 2002). These active region transient brightenings (ARTBs) can be observed with Extreme Ultraviolet (EUV, Seaton et al., 2001) and soft X-ray instruments (Shimizu et al., 1992; Shimizu, 1995), though their transient nature and the differences in temperature response makes direct comparison between the two wavelengths difficult (see for example: Berghmans et al., 2001). In this chapter, we do not distinguish between ARTBs and microflares, and use the terms interchangeably.

In order to study the scales involved in heating small scale coronal brightenings, in Chapter 2, we detected and modeled 34 ARTBs observed with XRT. The ARTBs were modeled as bundles of independent strands using a variety of heating functions and the Enthalpy Based Thermal Evolution of Loops (EBTEL, Klimchuk et al., 2008; Cargill et al., 2012a,b) code, incorporating a genetic algorithm to find the parameters that best reproduced the observed light curves of the brightenings. The results of Chapter 2 showed that an impulsive mechanism was most likely required to instigate the heating of the individual strands, though they could not distinguish between ARTBs heated by a single strand experiencing multiple heating events, or many strands each being heated once. In reality, it is expected that these structures are actually multiple strands "braided" together, each of which are heated multiple times. This type of strand braiding has been observed with Hi-C (Cirtain et al., 2013).

The improved resolution of Hi-C provides a unique opportunity to better constrain the size of the events which cause these brightenings. In this chapter, we apply the detection and modeling methodology of Chapter 2 to Hi-C data. By detecting and modeling ARTBs observed with Hi-C we have found that the rate of ARTBs might be significantly higher than previously discussed in the literature, consistent with the findings of Testa et al. (2013). The results of this forward-model also support previous findings (Cirtain et al., 2013; Winebarger et al., 2013; Brooks et al., 2013) that the scale of the observed braiding is very close to the resolution of the Hi-C instrument, promoting the need for more instruments with similar observational capabilities as Hi-C if we hope to understand the scales of energy release in the corona.

A brief overview of the method used to detect and model ARTBs is given in Sections 3.2.1 and 3.2.2. Section 3.3 will discuss the observations, with the results of the study shown in Section 3.4. A discussion of these results and comparisons to other studies is given in Section 3.5. Section 3.6 provides a summary of conclusions.

3.2. Method Overview

The method of detection and modeling is thoroughly discussed in Chapter 2, and we present here a brief overview for the benefit of the reader.

3.2.1. ARTB Detection

To find ARTBs in sequences of coronal images, we use a slightly modifed version of the detection scheme utilized by Berghmans & Clette (1999). The detection starts by subtracting the temporal running mean (width w_{rm}) from a calibrated, exposure normalized, and aligned stack of images on a pixel by pixel basis. After dividing by the standard deviation, the algorithm then looks for the brightest pixel in this residual. If this pixel value is larger than q_{D}, neighboring pixels that are larger than

q_C are grouped together. If 10 or more such pixels can be connected, a light curve is created, bounded by the largest spatial extent of the detected region. The flux of the light curve is normalized to DN s^{-1} pixel^{-1}. Regardless of whether or not the detected region is larger than our 10 pixel threshold, the pixel's values within the detected region are reset to the median value, and the process repeated until the brightest pixel in the residual is less than q_D. The extracted light curves are then modeled as multi- or single-stranded loops.

In Chapter 2, we used $w_\mathrm{rm} = 20$, $q_\mathrm{D} = 4$, and $q_\mathrm{C} = 3$ to detect ARTBs with the *Hinode* X-Ray Telescope (XRT: Kano et al., 2008; Narukage et al., 2011; Golub et al., 2007). Since Hi-C data are of significantly higher resolution (temporally, spatially, and spectrally), we found that these detection parameters should be modified to efficiently detect ARTBs with Hi-C. Exploratory analysis runs led to satisfactory results with $w_\mathrm{rm} = 15$, $q_\mathrm{D} = 3.5$, and $q_\mathrm{C} = 3$, which is closer to the values used in Berghmans & Clette (1999) of $q_\mathrm{D} = q_\mathrm{C} = 3$. The values of these detection constants caused significantly more spurious detections than in Chapter 2, but due to the small size of the Hi-C data set, it was deemed easier to remove these detections manually (see Section 3.3). An additional difference between the detections in this study and the those in our previous work is the detection (and analysis) of brightenings further from the core of the active region. These detections outside of the AR core generally occur along loops which appear anchored on one side to the AR, but could potentially behave slightly different than the ARTBs traditionally studied. For this reason, we also use the more general term, microflare.

3.2.2. Multi-Stranded Model

The light curves of the detections are then forward modeled as multi- or single-stranded loops with each strand modeled independently via the 0 dimensional EBTEL framework. The flux of the resultant strands are then superimposed to create a modeled loop. We then utilize the genetic algorithm pikaia (Charbonneau, 1995) to traverse the parameter space of the model to find which parameters minimize the χ^2 value between the modeled ARTB flux and the observed ARTB flux from Hi-C.

To create each strand in EBTEL requires a strand half-length (l_{s}) and a heating function. We estimate the (full) strand length from the observations (L_{obs}), and then constrain pikaia to search for strand lengths $L_{\mathrm{obs}}/2.5 \leq l_{\mathrm{s}} \leq 2.5L_{\mathrm{obs}}$: the upper limit accommodates a large range of projection effects, the lower limit allows a sanity check to the results. For each realization of the forward model, the strand length is fixed. The heating function for each individual strand is a triangular pulse whose width is varied by pikaia (though fixed for each loop realization) and whose peak is dictated by a heating envelope for the group. As in Chapter 2, for the case of a multi-stranded loop, we test the capabilities of two heating envelopes, a sinusoidal and a “lambda” envelope. Figure 4 illustrates these heating envelopes. The sinusoidal envelope shows a symmetric increase and decline for the rate of heat input to individual strands, such as might be predicted if the strands are heated by resonant absorption (Ofman et al., 1995; Walsh & Ireland, 2003), and the lambda envelope suggests a more impulsive onset to strand heating (followed by a period of relaxation) such as might be expected from a bursty reconnection scenario. The delay between individual heating events is constant for a single loop realization, but varied for different realizations by pikaia. We also model strands as monolithic loops, which act identical to the multi-stranded lambda envelope loops, except the heating all occurs within a single strand. Assuming a cylindrical strand of constant radius, the EBTEL results are then convolved with the instrument response function of Hi-C yielding a predicted flux. The strand radius of the model flux is then varied so that the peak flux from the model matches the peak flux of the observation. The multi-stranded sinusoidal and lambda envelopes, as well as the monolithic strand heated with the lambda envelope, are all independently tested, such that the results from each model can be compared.

3.3. Data

The Hi-C sounding rocket (Cirtain et al., 2013) launched on 2012 July 11, taking data for over 5 minutes, from 18:52:09 to 18:57:26 UT. The telescope is of very high resolution, taking images with 0.1” pixels in a narrow wavelength bandpass around 193Å. The entire 4096 × 4096 pixel CCD (4K) was read out from 18:52:09 to 18:55:30 at an average cadence of 5.7s image^{-1}, at which point the field of view was reduced to the central 1024 × 1024 pixels (1K) and the cadence increased to 1.38 s image^{-1}. These data were then calibrated, including dark subtraction, flat field removal, dust spot removal, and co-alignment (including tracking). In the case of the higher cadence 1K data, 4 images were stacked to improve the signal to noise, and to match the cadence of the larger images.

The detection algorithm was run on both the full field of view 4K Hi-C data as well as the higher cadence, smaller field of view 1K data. To ease the computational requirements, the 4K data were split into 16 1K data sets. As mentioned in Section 3.2.1, the parameters used in the detection algorithm were not fully optimized, returning many spurious "false positive" detections. These spurious detections include spikes due to instrument noise, and flux enhancements existing where only the beginning or end of the brightening was observed. Further optimization of the parameters would have taken more time than manual removal of the spurious detections, so we opted to tune the algorithm to over-detect regions and remove the poor detections manually by way of visual light curve inspection. In all, the algorithm returned 452 detections, 395 of which were spurious, and 57 were deemed suitable for analysis. The accepted detections are found in Table 7. Figure 9 shows a subframe of a Hi-C image and the detections within that region have been overplotted. The detected regions were then normalized as discussed in Section 3.2.1, and background subtracted by removing 80% of the lowest flux observed in the light curve (as discussed in Section 2.4.1). The aspect ratios denoted in Table 9 were calculated as the square root of the eigenvalues of the second moment of inertia matrix of the detection mask. Low values of the aspect ratio (near unity) potentially suggest a footpoint source, while

Table 7: Information on ARTBs detected and analyzed from the Hi-C data set running from 18:52UT to 18:56UT on 2012 July 11. The large variation in ARTB sizes, with a few large and many smaller detections, helps illustrate the advantage of using a high resolution instrument such as Hi-C. The aspect ratio was calculated from the shape of the detection, showing the range of shapes of detected regions, where values near one represent circular detections.

ARTB Number	Size of ARTB (pixels/image)	Number of Images	Aspect Ratio	ARTB Number	Size of ARTB (pixels/image)	Number of Images	Aspect Ratio
01	104	13	6.0	30	52	14	4.2
02	62	19	3.6	31	11	13	2.1
03	26	28	3.3	32	46	9	2.3
04	70	24	1.6	33	61	14	2.6
05	11	26	3.3	34	9	16	1.0
06	67	35	4.2	35	16	11	2.0
07	11	12	1.7	36	44	15	3.0
08	39	25	3.6	37	33	10	1.5
09	58	33	8.1	38	49	24	2.4
10	54	27	56.6	39	18	26	3.5
11	76	13	4.2	40	6	30	2.7
12	39	26	7.4	41	9	11	5.8
13	24	13	48.5	42	22	21	5.5
14	51	14	1.6	43	12	20	12.0
15	18	24	3.5	44	11	26	3.7
16	23	26	3.0	45	59	24	1.6
17	1072	13	29.7	46	22	26	28.0
18	46	16	14.5	47	17	21	4.0
19	40	17	15.2	48	19	23	6.9
20	84	6	7.7	49	9	21	2.7
21	70	11	9.7	50	14	23	5.5
22	16	19	3.0	51	26	32	2.5
23	520	14	10.9	52	11	25	3.7
24	58	10	3.4	53	12	21	2.9
25	95	9	45.8	54	34	19	3.1
26	12	21	2.9	55	13	10	4.2
27	21	18	5.4	56	22	26	4.6
28	86	18	11.6	57	24	20	16.9
29	17	13	1.2				

larger values (much greater than unity) illustrate a detection of a complete loop. This value, though, should be considered a minimum value, since it only represents the shape detected by the algorithm, and not necessarily the complete shape of the brightening. The range in these values suggest that we are seeing some footpoint heating events, and many loop long heatings.

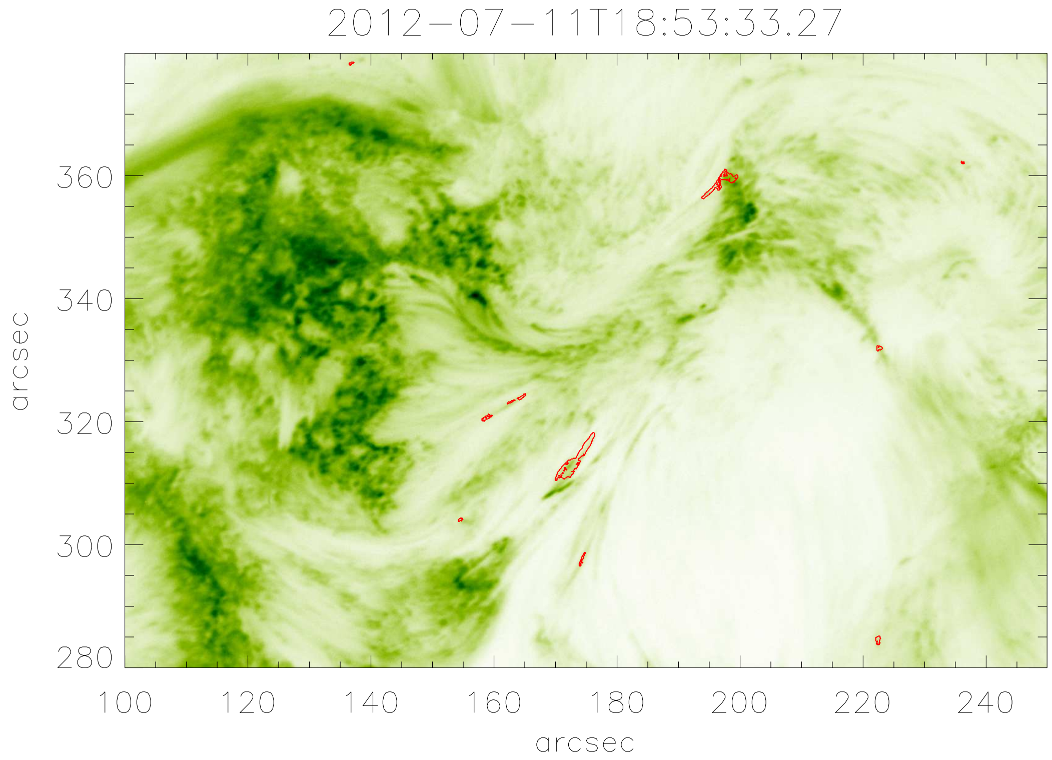

Figure 9: Reverse color example sub-image from a full-frame Hi-C image, with contours of detected and analyzed ARTBs overlayed in red. Here you can see a spread of the size and shape of detections as noted in Table 7.

3.4. Results and Analysis

The 57 ARTBs detected were forward modeled as discussed in Section 3.2.2; typical fits are shown in Figures 10 and 11. The parameters used to create these example fits are shown in Table 8. More fits and temperatures can be found in Appendix C. The median results of all of the fittings for each envelope are shown in Tables 9 and 10. The loop lengths noted in Table 9 represent the strands' length in the corona as used in the EBTEL calculation. The aspect ratio listed in Table 9 represents the model's resultant strand half-length divided by the strand radius. The multi-stranded model is allowed to create strands with radii the same size as their length, in essence creating point like brightenings, hence we use this aspect ratio as a validity test of our results, since it shows relatively slender strands.

The integral ratio shown in Table 10 is defined as the ratio between the integrated fluxes of the model and the observation. As the χ^2 should not be directly compared between different data sets, the integral ratio is an effective method for comparing the quality of fits between different events. The temperatures used in Table 10 are the emission measure weighted average temperature, and the duration of elevated temperatures are calculated from that. The duration of elevated temperatures is shown as the time spent above half-peak temperature (essentially the full-width at half-maximum) as well as the time the model temperature is above 5MK.

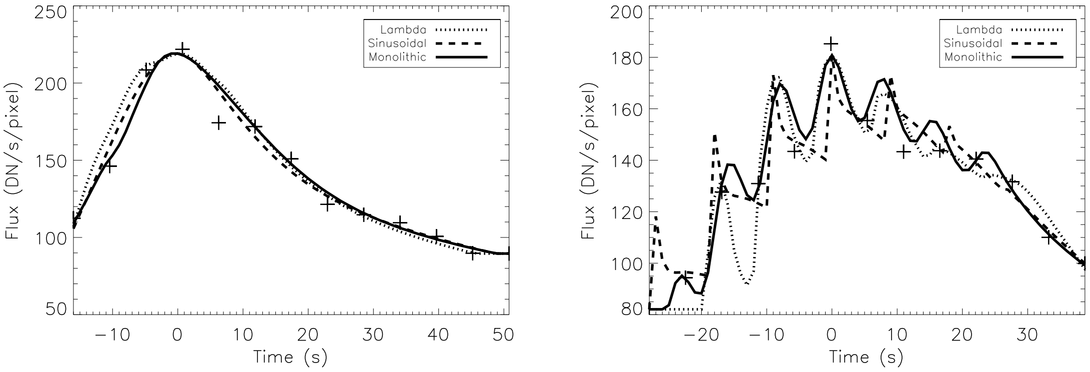

Figure 10: Example fit of the flux for ARTB numbers 1 and 31 as listed in Table 7. The dotted line is the fit from the lambda envelope, the dashed for the sinusoidal envelope and black for the monolithic envelope. The observational flux is denoted with (+)s. As is typical of the fits for Hi-C data, all three models visually fit the observed light curve quite well. The left fit is a typical fit, the right was chosen to illustrate the potential dynamics capable with such a model. More fits and temperatures can be found in Appendix C.

Table 8: Model Parameters for the results shown in Figures 10 and 11.

Envelope	Heat Input (10^{23} ergs)	Heat Pulse Width (s)	Event Delay (s)	Number of Heatings	Half-Length Result (Mm)	Strand Radius (km)
ARTB number 1						
Lambda	3.37	11	8	26	1.53	107
Sinusoidal	3.44	20	3	15	1.37	66
Monolithic	3.39	8	8	25	1.69	257
ARTB number 31						
Lambda	0.83	11	9	25	0.33	79
Sinusoidal	1.90	5	9	12	0.38	129
Monolithic	1.44	6	8	1	0.93	133

Table 9: Median of the best fit parameters (and median absolute deviation) used for the model for each envelope after running the fitting algorithm on the detections shown in Table 7. The average observed half-length was 1.18±0.12 Mm. For the lambda and sinusoidal case, the number of heatings represents the number of strands used. The monolithic envelope uses a single strand heated multiple times, with the heating events dictated by the lambda shaped envelope. The aspect ratio is calculated as the resultant strand half length divided by its radius.

Envelope	Peak Heating (ergs $cm^{-3}s^{-1}$)	Heat Pulse Width (s)	Event Delay (s)	Number of Heatings	Half-Length Result (Mm)	Strand Radius (km)	Aspect Ratio
Lambda	0.166±0.108	18±7	6±2	16±7	1.68±0.89	93±43	17.5±12.2
Sinusoidal	0.343±0.153	15± 8	7±1	17±7	1.85±0.69	52±37	27.5±19.3
Monolithic	0.123±0.046	4± 2	7±1	17±8	1.73±0.63	107±62	17.6±11.0

Table 10: Median results (and median absolute deviation) from the model. The χ^2 values and integral ratios favor the monolithic loop heated multiple times for Hi-C data. The heat input is the heating function integrated across the entire loop and lifetime of the heating event. The temperature refers to the emission measure weighted temperature. The FWHM is the full-width at half maximum of the temperature profile, and the time above refers to the time the temperature is above 5MK (both interpolated to 0.01 second resolution). The density is the peak average density from all strands, which **does not** occur during the temperature peak.

Envelope	Integral Ratio	χ^2 (DN)	Heat Input (10^{23} ergs)	Temperature Peak (MK)	FWHM (s)	Time Above 5MK (s)	Peak Density (10^8 cm^{-3})
Lambda	1.007±0.020	24.3±14.0	6.4±3.3	8.3±3.6	7.8±3.1	5.0±4.5	14.2± 7.3
Sinusoidal	1.015±0.016	24.2±15.7	5.1±3.2	3.3±0.6	16.1±10.5	-	25.6±13.2
Monolithic	1.009±0.009	15.2± 9.7	3.5±2.2	10.8±3.3	8.1±3.1	9.7±4.3	46.6±20.0

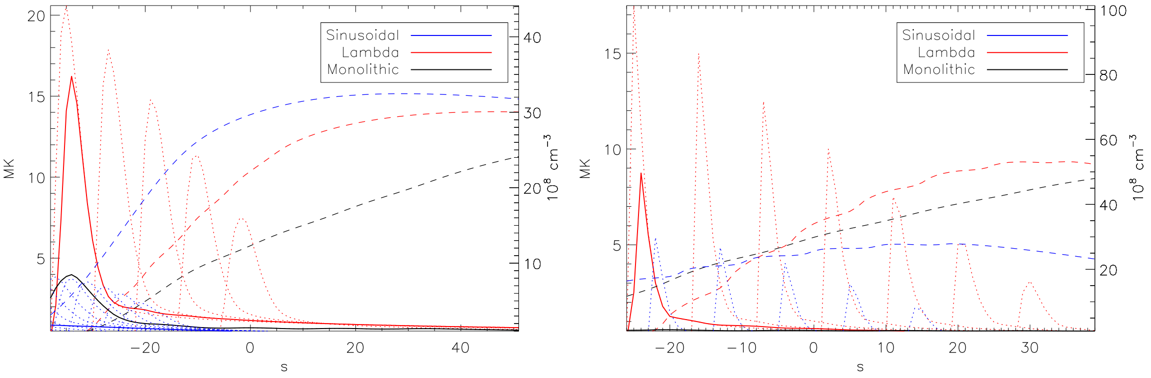

Figure 11: Example temperature and density results from the model. These particular results are for ARTB numbers 1 and 31 as listed in Table 7. The dotted curves represent the temperature evolution for each individual strand, while the solid lines are the emission measure weighted temperature. The dashed lines show the evolution of the density for each model. Blue curves are for the sinusoidal envelope, red for the lambda envelope, and black for the monolithic strand. The comparison between the peak temperatures for each envelope is not typical, though the short duration of the elevated temperatures is fairly typical (see Table 10). Note that for ARTB 31, the sinusoidal envelope result does not get above 1MK during the observation. These are the same ARTBs and timings depicted in Figure 10. More fits and temperatures can be found in Appendix C.

It is worthwhile to note the importance of initial conditions used in the EBTEL model. The rate of background heating and strand length in EBTEL determines the initial temperature and density of the loops. When the initial temperature and density are low, the strand temperature can become exceedingly hot, (over 15 MK), but quickly drops down to a more stable temperature before the density is sufficient for any observable signature. In the case of a multi-stranded loop and emission measure weighted temperatures, the staggering of strands will mitigate this effect for all but the first strand, as the short lived high temperatures will be normalized by the densities of the already heated strands. Some of these effects can be seen in

Figure 11 and Appendix C. Altering the background heating rate to 5% of the peak of the individual heating functions and re-fitting the best fit results did not change the resultant flux. Above 5% of the peak of the individual heating events only a few of the results were affected. For these reasons and since we are looking for notable brightenings above the background, we believe this ratio of background heating to peak heating to be a reasonable assumption. Additionally, higher background heating rates than used here would create steady loops hotter than observed in Winebarger et al. (2013).

The width of the individual heating pulses in the best fits was smallest for the monolithic envelope, though this number is slightly misleading, as the monolithic loop received a median of 17 heating events, significantly increasing the amount of time the loop experienced heating. This heating pulse width is smaller than the event delay, suggesting the model did not favor a steady heating in these strands, as there was generally time for the loop to cool slightly before being heated again (as evidenced in Figure 10). The heat input in Table 10 was calculated by integrating the heating function of all strands in time across the entire volume of the loop, assuming the strands to be cylinders with the lengths and radii returned by the model.

The modeling algorithm was quite adept at fitting all of the detections as shown by the low χ^2, and integral ratio values near unity in Table 10 and Figure 10. The right-hand plot of Figure 10 shows the dynamics possible with this model, even though the parameters of this fit might be unnecessarily dynamic due to possible signal oscillations from an uncalibrated noise source. A few of the fits exhibit this type of oscillatory behavior, but not the majority (a more typical example can be found in left of Figure 10).

The multi-stranded sinusoidal envelope resulted in a median peak temperature of over 3.3 MK, while the lambda envelope resulted in median peak temperatures of 8.3 MK and 10.8 MK for the multi- and single-stranded cases respectively. While these results corroborate the existence of hot quiescent active region plasma (above 8MK), the sinusoidal results are lower than might be expected (see right panel of Figure 11). Additionally, it was shown in testing (Section 2.3) that EBTEL tends to slightly overestimate temperatures when the time step is too large, but our time step size (1s) was empirically chosen to minimize this effect. It is important to note that for all results, the median duration of high-temperature (>5MK) plasma is less than 10s (below the temporal resolution of current instruments), occurs when the strand density is low (Figure 11), and extends over a region smaller than the spatial resolution of most instruments, all of which complicate the detection of the hot component suggested by the model. The strand peak densities are as expected, and occur much later than the temperature peak, minimizing the visibility of the temperature peak in the observed light curves.

By adjusting the peak flux returned by the model to that of the observation (and assuming cylindrical strands that bisect the pixel) we have obtained the crude estimates of the radius of the strands shown in Table 9. The results suggest a strand size of order 100 kilometers. This crude estimate is comparable to the resolving power of Hi-C (≈150km), and due to the assumptions involved in its calculation should only be used as an order of magnitude estimate. That notwithstanding, these results are consistent with the findings of Cirtain et al. (2013); Shimizu et al. (1992); Winebarger et al. (2013); Brooks et al. (2013), and Chaper 2 (among others).

3.5. Discussion

The often quoted ARTB occurrence rate is 1-40 events per hour per active region (Berghmans et al., 2001; Shimizu et al., 1992), which would predict no more than 2 detections during the observing period of Hi-C, significantly fewer than detected here. Hi-C observed a fairly typical active region, and extrapolating our data (57 detections in an active region in ≈5 mins) suggests the possibility of many hundreds per hour. Given the rudimentary nature and small sample size of this observation, this number cannot be taken too literally. It does suggest, though, that many of the events occur at spatial and temporal scales much lower than previous and current EUV detectors can detect, which may have inadvertently biased previous estimates. This was also noted by Testa et al. (2013).

A possible reason for this discrepancy can be seen in Figure 9; the detections are not limited to the core of an active region, such as is traditionally studied. This may bias our detected numbers, but not enough to eliminate the possibility of a higher microflare occurence rate than previously thought. This may also bias the sample of fitted data, as brightenings outside of active region cores (moss, plage, etc...) could be caused by slightly different mechanisms.

The resolution of Hi-C very likely plays a significant factor in the number of detected events, as previous studies used significantly less sensitive instruments, both in temporal and spatial resolution. Shimizu (1995) used SXT data which has a pixel size of ≈2.5", and a sensitivity to significantly higher temperatures. To test the effect of spatial resolution on ARTB detection, we rebinned the Hi-C data to the AIA (0.6" pixel^{-1}) and XRT (1.0" pixel^{-1}) scale. For the binned data to be detected by our algorithm, the brightening would have to span at least 1000 Hi-C pixels at XRT resolution, and over 360 Hi-C pixels at AIA resolution (since the algorithm requires a 10 pixel enhancement). We only detected two coherent brightenings with the AIA scaling, and 0 with the XRT scaling, which is consistent with the expected occurrence rate of 1-40 per hour. This strongly suggests that the rate of these events is significantly higher (possibly 10 times larger) than may have been previously thought: but due to the small number of high resolution observations, it may be premature to revise the projected rate of microflare occurrence with just the Hi-C results.

Microflares are generally quoted as having a thermal energy content between 10^{25}-10^{29} ergs (Shimizu et al., 1992; Berghmans et al., 2001), but the events studied here appear to be at least an order of magnitude less energetic than those often studied (median values of order 5×10^{23} for all envelopes - Table 10). Given the improved resolution, it is not surprising that we would detect brightenings with much lower energy contents than previously observed. This also helps to explain the more frequent detection than predicted.

When this method of detection and modeling was performed on XRT data (Chapter 2) understandably different results were returned. The peak emission measure weighted temperatures found in the XRT results were of order 15-20 MK, which is larger than found here, and likely attributable to the higher temperature plasmas to which XRT is sensitive. The low densities suggested here would also be difficult to detect with XRT. The visible quality of the fits when using XRT was also less robust than the results here (see e.g. Appendices B and C), which is likely due to a combination of factors including the broader passbands of XRT causing more background noise, and the inherent detection bias for larger and more complicated events in XRT.

The previous work with XRT was unable to clearly distinguish between a single strand heated multiple times and multiple strands each experiencing a single heating event. While there is still some ambiguity with the Hi-C results, it seems apparent from the χ^2 and integral ratios shown in Table 10 that at these spatial and temporal scales, only a few strands are being heated, but each is heated multiple times. Additionally (but subjectively), the visual quality of the fits were most often best when using the monolithic loop. This preference for a monolithic strand can potentially be used to improve the multi-thermal model by establishing a firmer spatial and temporal scale to allow the study of multi-stranded multiply heated loops observed by instruments with lower resolutions than Hi-C. The monolithic loops will be above

5MK for a longer period of time, since the multiple heating events keep their temperatures high. They also tend to be the most dense of the three envelopes, which promotes the visibility of these structures. Additionally, a single strand was preferred by the model even when multiple strands were allowed on two occasions: one case using the lambda envelope and one case using the sinusoidal envelope.

A useful comparison is to the work of Winebarger et al. (2013), who studied different loop brightenings in Hi-C. Combining the Hi-C data with AIA, they found the loops to be cool (≈0.25MK) and dense (10^{10} cm^{-3}). The cool temperatures were inferred from the fact that the brightenings appeared in both hot and cool channels of AIA simultaneously, and were supported by a DEM analysis. Due to the very short duration of the high temperature phase suggested in the present work, it would be difficult for the microflares analyzed here to show up in AIA, given the lower cadence and low strand filling factor. These discrepancies could result simply from analyzing a different type of event, as the loops studied herein are not necessarily as easily identified as loops given the automated detection algorithm employed. The objectives of the present work differ from those of Winebarger et al. (2013) (as well as those of Brooks et al. (2013, 2012)), as reflected in the methodologies involved: Winebarger et al. (2013) and Brooks et al. (2013) were specifically investigating the nature of isolatable loops, and so sought out features that could unambiguously be identified as such for their analyses; whereas the present work focuses on transient brightenings regardless of their shape, and thus utilizes an objective detection algorithm that triggers only on changes in the brightness.

Additionally, we also note the correspondence between the energy input and the observed radiation. It is common to use the observed radiation as a proxy for the total energy of the microflare (i.e., Hudson, 1991), and we can now compare the models energy input into the strand to the various radiative measurements. In Figure 12 we compare the observed radiation flux, input energy, conductive losses and radiative losses. The radiation flux is calculated /by converting the detected light curve flux into energy by assuming all observed light is 193Å and converting from DN s^{-1} $pixels^{-1}$ to ergs s^{-1} $pixels^{-1}$ using the instrument response function of Hi-C. The losses are calculated from the EBTEL results for the best fit of each observation. This is to show the scaling between input and output energy, which can be fit with power law of 0.65 and 0.75 for the multi-stranded and single stranded cases respectively.

3.6. Conclusion

We have detected and modeled 57 brightenings observed with the Hi-C instrument as strands experiencing different forms of heating, and found them to be quickly and consistently heated to temperatures of order 10MK at low densities, generally cooling to temperatures below 5MK very quickly, before there is significant density for direct detection. The size of the strands is also sub-resolution for most instruments, which makes detection difficult without Hi-C.

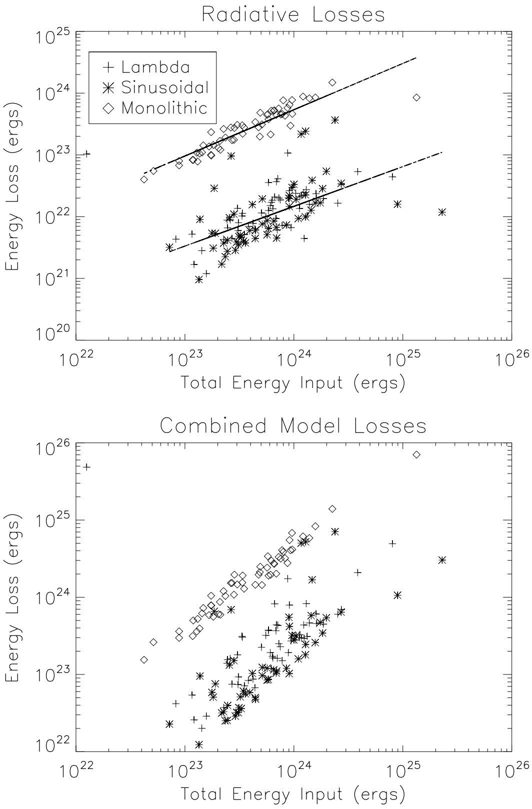

Figure 12: Energy distributions from the modeling. The horizontal axis in all plots is the total integrated energy input of the model, less background flux. The upper left compares the total energy to the integrated radiative loss function, the upper right shows the integrated conductive losses, the lower left shows the combined energy loss from both radiative and conductive losses. The lower right shows the integrated energy incident on the detector, with background subtracted, and assuming a wavelength of 193Å for the incident photons. The lines in the upper left plot represent a best fit line between the integrated radiative loss function and the total energy input for the single and multi-stranded cases, suggesting a power law ratio between them with an exponent between 0.65-0.75.

The results from this study provide an improvement from those of Chapter 2, as the monolithic envelope was marginally preferred by the model at Hi-C scales. The model was able to match the observed data easier with the monolithic envelope with the least energy and very reasonable parameters. The widths of these strands should be near the resolution of the next generation of imagers (including Hi-C), and could thus be resolved on a consistent basis.

The number of detections of coherent brightenings was significantly higher than predicted by previous estimates, which is likely due to the unprecedented resolution of Hi-C. The length of time of the Hi-C observations and sample size is too small to effectively update the predicted frequency of these events for future observations, though we recommend that more observations at similarly high temporal and spatial resolution be made to explore more thoroughly the frequency of their occurrence, as well as the distributions of size, duration, and energy budget. With more results, we could better develop the distribution between the frequency of events and energy input of microflares. Better understanding of this distribution would improve the discussion of whether nanoflares can heat the corona started via Lin et al. (1984).

In all, these results strongly promote the scientific utility and benefit of higher resolution coronal imagers, such as Hi-C.

3.7. Acknowledgements

We acknowledge the High resolution Coronal Imager instrument team for making the flight data publicly available. We especially thank Sabrina Savage for her help with acquiring and calibrating the data. We also thank Hugh Hudson for helpful discussions about microflares. This work was partially supported by NASA under contract NNM07AB07C with the Smithsonian Astrophysical Observatory.

4. INITIATION OF AR-AR RECONNECTION AFTER FLUX EMERGENCE USING PROBA2 SWAP AND LYRA

Contribution of Authors and Co–Authors

Manuscript in Chapter 4

Author: Adam R. Kobelski

Contributions: Conceived and implemented study design. Wrote first draft.

Co–Author: David E. McKenzie

Contributions: Helped to conceive study. Provided feedback of analysis and comments on drafts of the manuscript.

Co–Author: Daniel B. Seaton

Contributions: Assisted with acquisition and calibration of PROBA2 data.

Co–Author: Derek A. Lamb

Contributions: Assisted with using SWAMIS software.

Manuscript Information Page

Adam R. Kobelski, David E. McKenzie, Daniel B. Seaton, Derek A. Lamb
The Astrophysical Journal
Status of Manuscript:
_x_ Prepared for submission to a peer–reviewed journal
____ Officially submitted to a peer–reviewed journal
____ Accepted by a peer–reviewed journal
____ Published in a peer–reviewed journal

To Be Submitted 2014, The Astrophysical Journal

ABSTRACT

Magnetic reconnection is one of the most important and fundamental processes in astrophysics, but is not yet fully understood. The speed at which reconnection occurs and the MHD instability that instigates the reconnection are still heavily debated. Observational signatures of reconnection can provide necessary information for improving our understanding of how magnetic energy is dissipated in the sun and universe. Here we perform an observational study utilizing SWAP onboard PROBA2 as well as HMI magnetograms to provide empirical insights into the factors which control the rate of reconnection by studying the initiation of flux transfer between newly emerged active regions (ARs) and nearby pre-existing active regions. We have measured the delay between flux emergence as seen in HMI data and signatures of reconnection between active regions observed with SWAP for 8 events. In 6 of the cases we find delays that are similar to those reported previously in the literature; we also find one case with a much shorter delay, and one case in which the two ARs do not appear to connect during the time span studied.

4.1. Introduction

In considering an emerging active region (AR) to be a flux tube rising from the convection zone through the photosphere, the AR can be thought of as initially only connected to itself. In the case of a new emergence near a pre-existing AR, this magnetic topology is energetically unfavored and the magnetic field lines of the emerging AR will reconnect to the older AR. Potential field extrapolations of such regions clearly show it is a lower energy configuration to have regions of a given single polarity from the newly emerged AR connect to opposite polarity poles of the pre-existing AR. This magnetic reconfiguration via reconnection is frequently assumed, but the timescales between AR emergence and reconnection have not been well documented. Some observations reported in the literature (Longcope et al., 2005; Zuccarello et al., 2008; Tarr et al., 2014) have recorded long delays, of order 24 hours, between flux emergence and the first significant reconnection to nearby pre-existing ARs, suggesting that some “threshold” (such as the accumulation of electric current as described in Longcope et al. (2005)) must be reached before the reconnection is accelerated and substantial amounts of flux can be transferred. Several recent numerical models (*e.g.*, Cassak et al., 2006; Galsgaard et al., 2007) have been specifically aimed at determining the factors that set this threshold. It is noteworthy that the observations can appear to conflict with these theoretical predictions (*e.g.*, observations from Zuccarello et al. (2008) suggest timescales of ≈20 hours, conflicting with the Galsgaard et al. (2007) prediction of ≈20 minutes). Establishing the range of delays between emergence and reconnection is the first step towards an understanding of the factors that determine the nature of this threshold and characterize the mechanisms that control reconnection.

To put the investigation of the threshold for reconnection initiation onto a firmer observational footing, we follow up on measurements of AR to AR flux transfer to better establish the conditions under which a delay may be observed. We study this delay by looking at emerging ARs observed with the full sun observational capabilities of the Sun Watcher with Active Pixels and Image Processing (SWAP, Seaton et al., 2013; Halain et al., 2013) on the Project for Onboard Autonomy 2 spacecraft (PROBA2, Santandrea et al., 2013) and the Helioseismic and Magnetic Imager (HMI, Scherrer et al., 2012) onboard the Solar Dynamics Observatory (SDO, Pesnell et al., 2012) as well as high temperature information from the X-Ray Telescope (XRT: Kano et al., 2008; Narukage et al., 2011; Golub et al., 2007) on *Hinode* (Kosugi et al., 2007). The emergence of magnetic flux is timed with HMI line-of-sight (LOS) magnetograms via feature detection (but not emergence tracking) from the SouthWest Automatic Magnetic Identification Suite (SWAMIS, DeForest et al., 2007). SWAP 174Å data are used to observe and quantify reconnection events between the ARs. For one event, we also include reconnection timings from XRT. This study will help us better constrain the rate of free energy accumulation in magnetic fields as it pertains to the initiation of reconnection.

In Section 4.2, we outline the basic method for analyzing the flux emergence events. A description of the data used is found in Section 4.3. We will detail the current results in Section 4.4, and discuss the future plans for this study in Section 4.5.

4.2. Method

We detect individual regions of magnetic flux observed with HMI using the SWAMIS software. SWAMIS detects features in the full disk HMI magnetogram with a thresholding algorithm at a variety of spatial scales. The thresholding identifies pixels in the input magnetogram that are greater than a set upper threshold. All pixels greater than a lower second threshold that touch pixels above the upper threshold are then lumped together as a detected "feature" (similar to that discussed in Section 2.2.1, but the detected regions are limited to a single image at this point). SWAMIS then attempts to connect regions of emerging flux between images, creating "events," though we do not utilize this feature of SWAMIS. To connect the detected features into regions so that we can locate and separate pre-existing regions from emerging regions, we look for regions of similar polarity directly neighboring each other in the image plane and consecutive images. We can then visually verify that a distinct set of regions consisting of flux of both polarities can be observed emerging in the magnetograms, and that these regions coincide with a new numbered AR as denoted by the National Oceanic and Atmospheric Administration (NOAA). We define this new set of regions as the emerging flux, as distinguished from the pre-existing flux.

The next step is to obtain calibrated SWAP and XRT data from the noted emergence region. We then extract a "slit" from the SWAP data between the ARs, attempting to establish a line separating the ARs for all possible time steps, based on the method employed in Longcope et al. (2005). The location of the slit must be carefully chosen to prevent contamination from loops which are not reconnecting between the ARs. We thus create the slit by selecting a series of line segments between the active regions through which no self-connecting (within a single AR) loops can be seen. By tracking EUV and X-ray flux peaks between successive slit images, we can observe loop brightening from reconnection between the ARs, which can be verified in the full-frame images. In order to reliably make these measurements and observe the loops, we require multiple images within the cooling time of the loop, which is of order an hour (Cargill et al., 1995), which is easily obtained with SWAP's standard cadence of 85s. By comparing the timings observed with SWAP and XRT, we can learn about the impulsiveness of the heating of the loops. In the case that the loops show up in XRT first, the loops would be heated over a prolonged period of time, and if they are readily observed in SWAP but not XRT, it implies that the heating was quite impulsive such that the densities in the loops do not reach observable levels until after the temperature has fallen below the XRT bandpass.

4.3. Data

Using the NOAA AR database, we have identified 39 instances of new ARs emerging within 10 degrees of pre-existing ARs during the PROBA2 operational phase between 2010 September and 2013 January. Of these 39 instances, 38 of the emergences occurred within 45 degrees of disk center, which will allow the use of HMI line-of-sight (LOS) magnetograms. Visual inspection of the SWAP data showed that some of the regions appear to emerge underneath the AR canopy of the pre-existing region, making detection of the reconnection too difficult for proper analysis. This narrowed our list down to 8 regions as shown in Table 11. This selection mechanism allows us to better establish across many event types what type of delays and features should be expected, though it is still biased against ARs which exist very close together.

We utilize the full resolution HMI LOS magnetograms to measure the photospheric magnetic flux. HMI observes the full solar disk in an absorption line of Fe I at 6173Å with 0.50” pixels, which is used to construct the LOS magnetograms used

Table 11: Information on emergences analyzed.

Event Label	Existing AR	Emerging AR	Time of Flux Emergence	SWAP delay (hours)
1	11124	11125	2010 Nov 10 00:00:12	24.4
2	11149	11152	2011 Jan 20 00:00:12	26.6
3	11161	11162	2011 Feb 17 14:24:00	12.8
4	11334	11335	2011 Oct 29 15:48:00	40.5
5	11395	11398	2012 Jan 12 07:48:00	29.4
6	11590	11597	2012 Oct 16 22:12:00	¿72
7	11631	11632	2012 Dec 07 00:12:00	22.8
8	11649	11655	2013 Jan 08 00:12:00	32.0

here. The HMI images are taken at a cadence of 4s, but we use the data averaged over 5 minutes, creating the 720s cadence magnetograms, which have an improved signal strength and reliability.

SWAP is a full sun EUV imager onboard the PROBA2 satellite, utilizing a unique CMOS-APS detector and wide 54×54 arcminute field of view with a narrow bandpass focused on 174Å and 3.2” pixels. The bandpass focusses on emission from Fe IX and X, with small contributions of Fe XI. These emission lines showcase emission of plasma around 0.6MK. The average exposure time is 10s at a cadence of ≈85s. We have used Solar Soft (Freeland & Handy, 1998) software to grab the SWAP data, and it is calibrated to normalize the exposure times, remove cosmic ray hits, dark noise, and other instrument noise using p2sw_prep. After creating a cutout of the SWAP data around the desired region, the data are co-aligned using cross-correlation.

In one case, we also look for signal in XRT data. XRT is a grazing incidence soft X-ray telescope onboard the *Hinode* satellite. XRT observes high temperature coronal plasma (generally above 2MK), in a variety of wide bandpasses with 1.0” pixels. When available, the comparatively high temperatures viewed with XRT allow us to better bound the temperatures of the observed reconnection event. The XRT data is calibrated and exposure normalized using the method described in Appendix A. The XRT data is then co-aligned by removing spacecraft pointing inconsistencies artifacts via xrt_jitter, available in the Solar Soft library.

4.4. Results and Discussion

To illustrate our results, we begin the discussion with a detailed description of our analysis on one case, event 2 in Table 11. We follow with a brief description of the results from the other observations. The SWAP delays from each event are listed in Table 11. A full disk image from SWAP from 2011 January 21 at 7UT is shown in Figure 13, showing these two regions are the dominant source of coronal activity between the 20th and 21st. A few GOES B class events occurred on 2011 January 20 and 21, in addition to 4 C class events after 12UT on the 21st.

We begin by looking at the HMI magnetograms of the desired active regions, and attempt to separate the emerging flux from the pre-existing flux in order to time the beginning of flux emergence. We have done this by detecting individual single polarity regions within each HMI magnetogram. We then look for overlaps in single polarity regions between images, and consider them connected. This creates some problems in distinguishing between pre-existing and emerging flux regions (such as shown in Figure 14), but as the emergence of the flux tube can be treated as a bi-polar

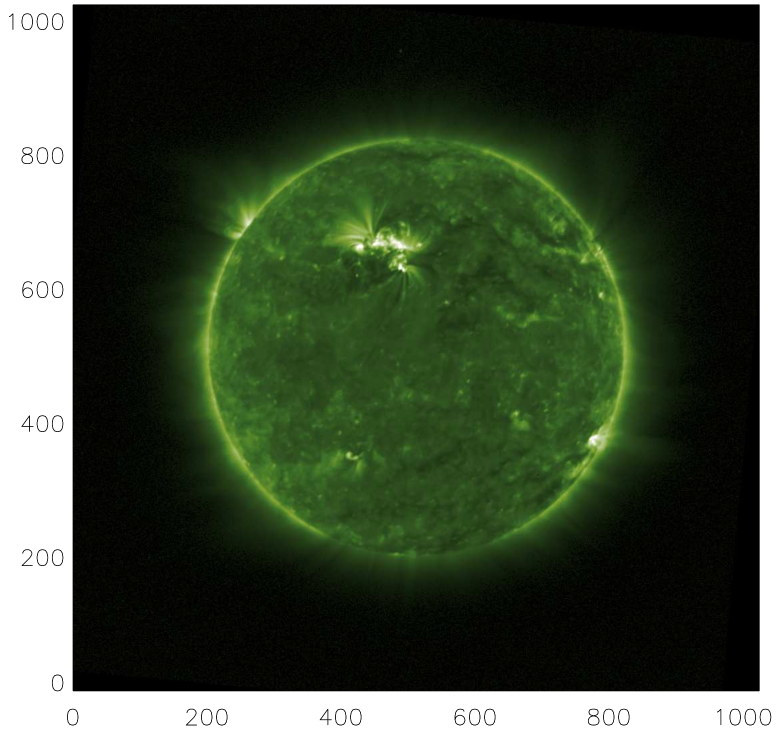

Figure 13: Example full sun image from SWAP of event 2. This image is from 2011 January 21 at 7UT. ARs 11149 and 11152 are the dominant regions on the disk.

event, we only need to separate the emergence of a single pole. We then consider the emergence to begin (Table 11) once an isolated pole is detected.

In order to determine the time at which reconnection connects the two regions, we look at coronal data from SWAP, and locate a line which divides the pre-existing from the emerging region, as shown in the middle panel of Figure 14. To best observe and enhance the loop brightenings, we subtract off a 3 pixel (in 3D) wide running mean from the SWAP data, and use this smoothed image to locate a proper slit from which to create a stack plot. The stack plot is created from the unsmoothed data by

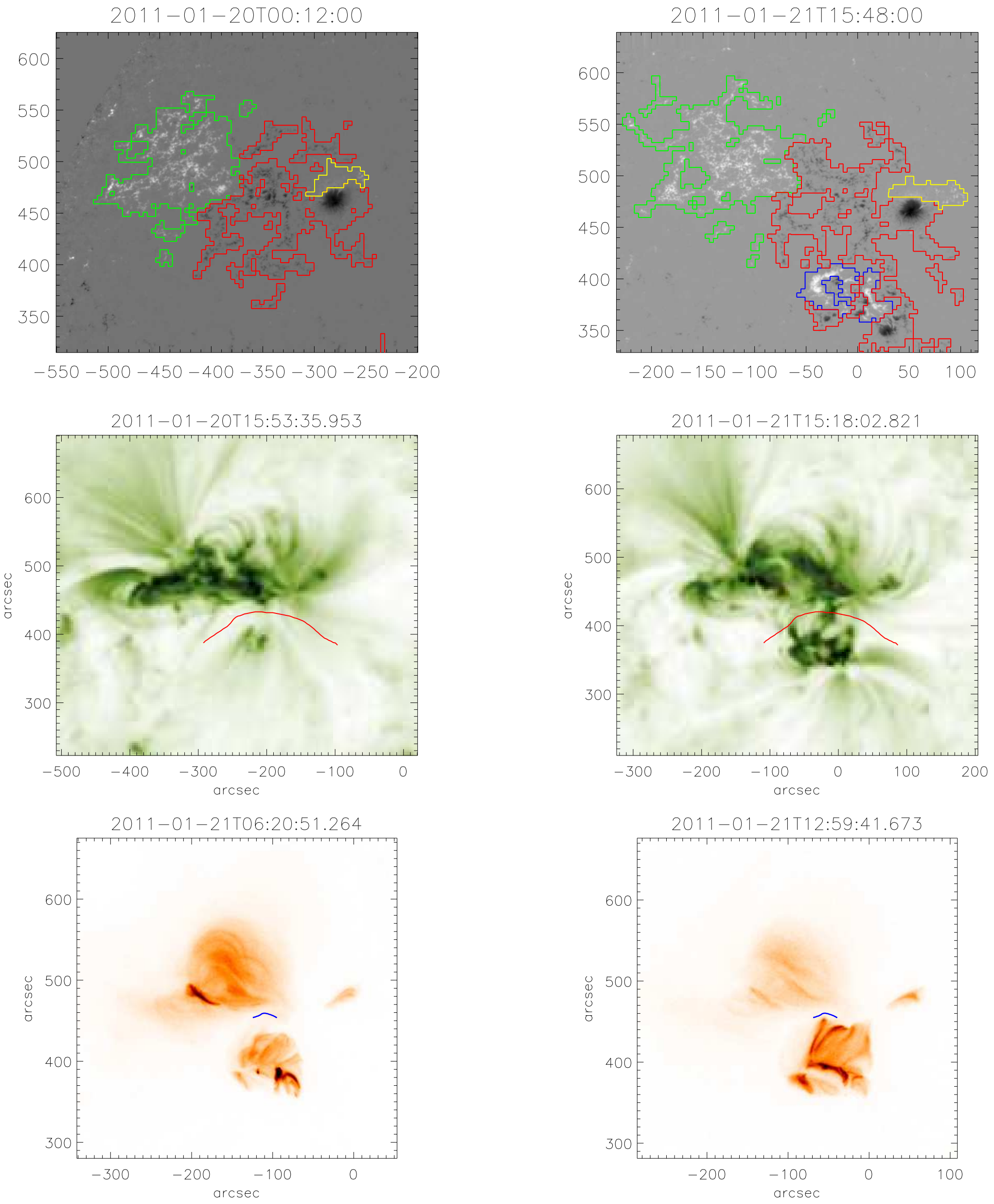

Figure 14: HMI magnetograms (top) and reverse color SWAP and XRT images (middle and bottom) showing the emergence of AR 11152 near AR 11149. Top : The left image shows the region before emergence, and the right shows the region after the emergence has begun. The different color contours represent different flux features clumped together by polarity and connectivity. Note that the negative flux of the emerging region is considered part of the pre-existing region, but the positive flux is independent. Middle: The left reverse color SWAP image shows the regions after flux emergence but before the regions connect. The right shows the regions after connection, showing many loops crossing the "slit," which is denoted by the red line. Bottom: Reverse color XRT images of the region, with the slit used denoted by the blue line. This smaller slit spans the approximate area where the first loops can be seen to connect the two regions in SWAP. The left is with the Ti_poly filter, the right is the Al_mesh filter, image timings picked to showcase detail of the X-ray structures.

stacking the intensities across the slit at successive times, as shown in Figure 15. We then look for brightness enhancements in the resultant stack plot. We then verify in the full image which brightenings relate to loops existing between the ARs, and which are due to pre-existing loops and possible EUV jets and other sources. All features which do not appear to be structures connecting the ARs are ignored.

Similar to the results of Longcope et al. (2005), the stack plots show possible early heating events just a few hours after emergence, while a more thorough bout of heating events occurs many hours later. For the case of Event 2, as shown in Figure 15, the first possible heating events become visible in the stack plot 10.2 hours after emergence, though the bulk of the heating begins 26.6 hours after emergence.

For this event, we also looked at the XRT data, to see if any signatures of reconnection could be seen in emission from higher temperatures (bottom panel of Figure 14). During this event, XRT was viewing the region of interest with Ti_poly and Al_mesh filters, a 384"×384" field of view, and an average cadence of 4 minutes. We have performed the same analysis as we did for the SWAP data, creating a slit and then looking for brightening events across the slit. Due to inconsistencies between the alignments and plasmas seen with SWAP and XRT, a different slit was used for XRT, though the same slit was used for both XRT filters. Since we could better localize the region where reconnection occurs, a smaller slit was used for XRT. The light curves for XRT are shown in Figure 16. The signal between the AR 11149 and AR 11152 is too low to perform an accurate filter ratio temperature measurement, but using the

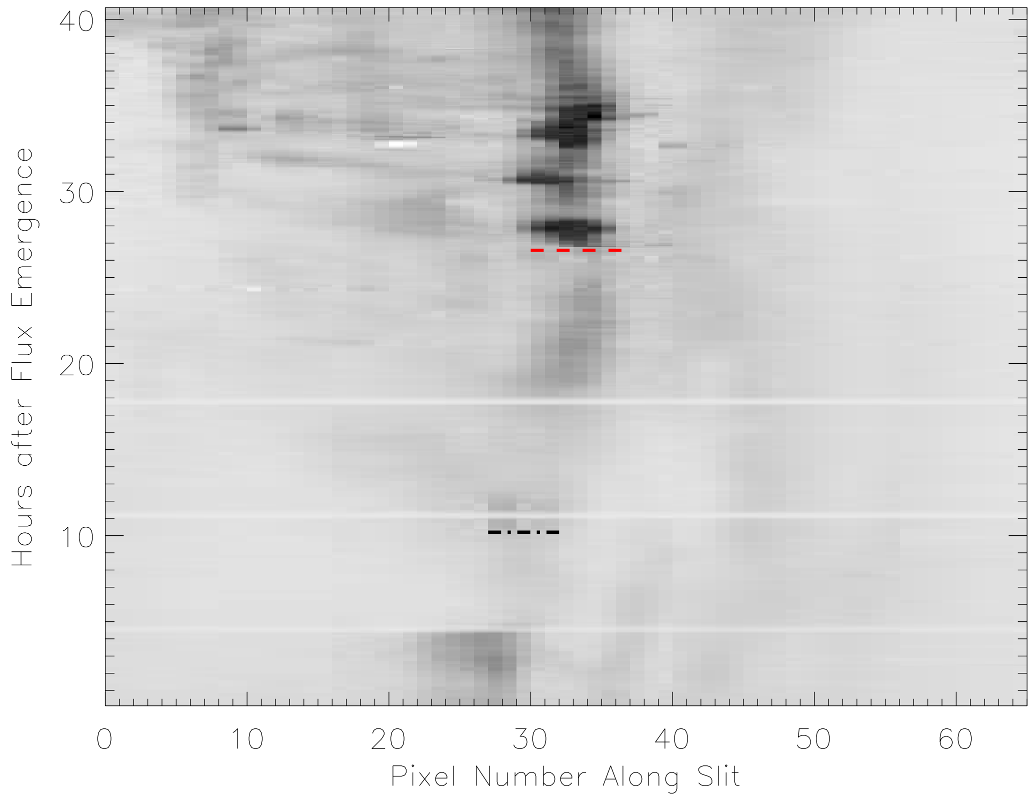

Figure 15: Stack plot the “slit” used for SWAP on Event 2. The black dash-dot line represents the first notable brightenings across the region, the red dashed line represents the beginning of regular reconnection. The x-scale represents the pixel number along the slit, which begins on the left-most edge of the slit noted in Figure 14.

estimates discussed in Takeda et al. (2012) suggests temperatures above 3MK around the peak time of 12:25:53 UT, 29.2 hours after the flux emergence and 2.5 hours after reconnection was observed with SWAP.

It is unexpected that the brightenings are first visible in SWAP, as it would be expected the events would be visible in the hotter channels first. Due to the nature of loop heating, it is difficult to see loops heating up, as the temperature changes rapidly (see Chapter 3), while the density takes longer to respond, and as such there

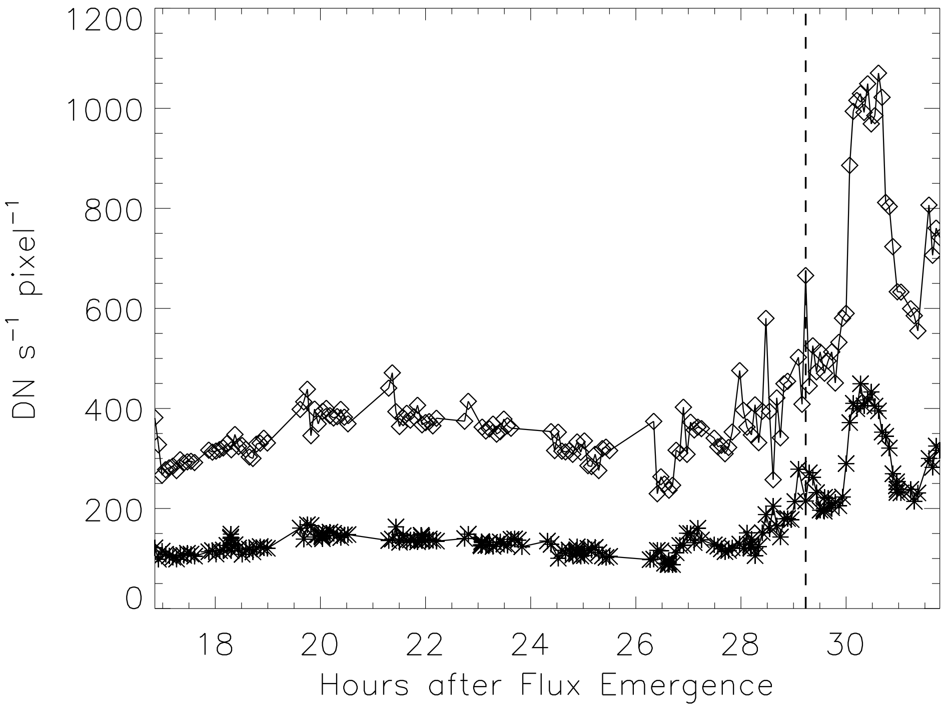

Figure 16: The average X-ray flux observed in the XRT slit. The diamonds represent the Al_mesh flux, the stars the Ti_poly flux. The dashed vertical line represents the peak time in XRT for this event (12:25:53UT, 29.2 hours after emergence).

is not enough hot plasma to be observed while the loop temperature is rising. What can be seen, though, is a dense loop cooling down, and thus it is expected to see the loop in higher temperature passbands before becoming visible in cooler channels. As such, we expected to see signs of the brightening in XRT before SWAP, which was not observed. Depending on how impulsive the heating of these loops is, it is possible that when the loops are warm enough to show up in the XRT passband, there is not sufficient density to be observed, and thus the first loops may not be seen in X-rays. This is a useful finding, supporting the impulsive heating of the loops, as a more prolonged heating would allow the density to grow while there is still sufficient temperature to be observed with XRT.

The same process was followed for the other 7 events, though without analysis of XRT. For the case of Events 1,5 and 7, similar findings were found as discussed for Event 2. Some initial heating signatures could be detected 6.2, 11.0, and 11.2 hours after emergence (respectively), but the bulk of the heated loops became visible 24.4, 29.4, and 22.8 hours after emergence. In the case of Event 3, initial connections between AR 11162 and 11161 can be seen quite quickly after emergence, though the bulk of the loops are observed 12 hours later. This is the shortest delay observed here. Event 4 showed the longest delay, taking 40.5 hours before the bulk of the heated plasma became visible. The apparent distance between these ARs and their sizes does not seem to be a factor as they are of comparable size and scale as the other analyzed events. No reconnected loops spanning ARs 11590 and 11597 in Event 6 could readily be seen 3 days after emergence, suggesting no large scale reconfiguration occurred for these regions. Event 8 showed a longer delay than many of the other events. In Event 8, AR 11655 emerges on the leading edge of a group of established ARs, which could be a possible factor in the extended delay noted here. The early faint heating events in Event 8 became visible 23.5 hours after emergence, and 8.5 hours before strong heating was detected. In all cases of observed heating signature, a smaller, less prominent brightness enhancement was observed 8.5-14 hours before the main reconnective event, regardless of the delay between emergence and reconnection.

4.5. Conclusion

In this chapter, we analyzed 8 flux emergence events, and quantified the delay before it reconnected to the nearby pre-existing AR. We found that it generally took around 25 hours for the regions to connect with each other, though we found one case with a notable smaller delay ($\approx$14 hrs) and one where no reconnection was detected. This average delay is more likely an upper bound, given the difficulties with detecting such faint events and the temporal and spatial resolution of SWAP.

Similar to the results of Longcope et al. (2005), it was found that small scale heating could be detected before the larger events could be detected. Here it was seen that this delay was consistently around 12 hours before the main heating effects were observed in SWAP, suggesting that this gap can be more directly tied to the reconnection events than the flux emergence event, and could potentially be a more reliable standard for the delay between emergence and reconfiguration than looking for distinctive heating signatures in the observations.

In the future, we would like to track the rate of flux emergence, and attempt to perform some potential field source surface extrapolations to attempt to better understand what made the two exceptional cases behave differently than the others. The current era of high resolution multi-filter full sun imagers will be beneficial to studies such as these. It is possible for us to view most flux emergences, and have supporting coronal data to view their reconnections. A project like this would benefit from having multiple filters, observing cooler temperature plasma such as is available with AIA.

4.6. Acknowledgements

We thank the PROBA2 Guest Investigator program, which helped to support this research. We also thank Craig DeForest for his assistance with SWAMIS. SWAP is a project of the Centre Spatial de Liege and the Royal Observatory of Belgium funded by the Belgian Federal Science Policy Office (BELSPO). HMI data is courtesy of NASA/SDO and the AIA, EVE, and HMI science teams. *Hinode* is a Japanese mission developed and launched by ISAS/JAXA, collaborating with NAOJ as a domestic partner, and with NASA and STFC (UK) as international partners. Scientific operation of the *Hinode* mission is conducted by the *Hinode* science team organized at ISAS/JAXA. This team mainly consists of scientists from institutes in the partner countries. Support for the post-launch operation is provided by JAXA and NAOJ (Japan), STFC (U.K.), NASA, ESA, and NSC (Norway). This work was partially supported by NASA under contract NNM07AB07C with the Smithsonian Astrophysical Observatory.

5. CONCLUDING REMARKS

In Chapter 2, we built and developed a detection algorithm (based on the works of Berghmans & Clette (1999)), which was able to locate small scale brightenings in XRT. This simple, yet adaptable detection method was then used to find brightenings (microflares) in XRT and Hi-C (Chapter 3). The detection of brightenings in Hi-C showed the importance of high resolution instruments, which can be used to justify future developments in instrumentation.

We then developed an efficient and effective method to study the microflares we detected. This method involved modeling the microflares as multi-stranded loops and using a genetic algorithm to minimize the χ^2 value between the model and the observations. Using this model, we were able to show that the observed microflares tend to require an impulsive onset to their heating, and require multiple heating events. This promotes magnetic reconnection as the dominant heating source in coronal loops, as wave dominated heating would seem to favor a more steady, symmetric onset to the heating. In Chapter 2, we were unable to distinguish whether the microflares were multiple strands each being heated only once, or whether they were made of a single strand heated multiple times. The results did favor a small number of strands, though, each with radii of order hundreds of km.

In reality, these structures are likely made of a few strands, each of which are heated multiple times. This option, though, was not studied, as it would greatly increase the number of parameters required in the model, and would significantly limit the amount of useable observations by requiring each detected microflare to be observed with more data points to avoid over-constraining the system. If we can limit the other parameters, we could begin to venture into the territory of modeling multiple strands heated multiple times.

One possible constraint which could improve our ability to add parameters to the model would be to better limit the size of the constituent strands. Chapter 3 partially addressed this goal, by modeling observations from an instrument with significantly better resolution; Hi-C observed the corona with an order of magnitude improvement in pixel size (2 orders in area!) compared to XRT. We utilized this resolution to constrain the size of strands to around one hundred km in radius. The results from Hi-C also favored a single strand experiencing multiple heating events, further supporting the size constraint reached by the forward model. This could allow us to limit the number of strands available to the forward model when analyzing lower resolution data, allowing us to implement multiple strands being heated multiple times.

The results of Chapters 2 and 3 both favored reconnection instigated heating in coronal loops, which prompted a more direct study of how magnetic reconnection heats loops. In Chapter 4, we looked at magnetic flux rising from the photosphere, and how it relates to reconnection in the corona by studying a few different flux emergence events. Utilizing data from multiple satellites and telescopes, we were able to add to the statistical body of knowledge of reconnective heating.

All of the results reported here can benefit from follow-up studies. In the case of the heating of small scale transients, it would be beneficial to analyze a larger number of XRT brightenings, which could help to distinguish between the different regimes of parameter space. Combining these results with spectroscopic analysis from instruments such as EIS we could better understand the thermal evolution of the plasma. The forward model would also benefit from a higher dimensional model (than EBTEL) that allows more complicated flows within the loop. This would improve the results we already have, and potentially allow us to expand our study to larger events such as flares, which are not necessarily within the regime of EBTEL.

The study of reconnection after flux emergence also has a lot of potential follow-up studies. The inclusion of AIA data would improve the spatial, temporal, and spectral resolution compared to SWAP, and could thus be used to better infer the rate and consistency of cooling in loops. It would also be worthwhile to combine all of the studies discussed here. With an instrument such as the Solar Optical Telescope on *Hinode*, it would be possible to observe and track small scale flux emergences and compare them to their coronal signatures, which could be detected and analyzed with a higher resolution imager using the methods of Chapters 2 and 3. The possibilities for future studies based on the work done here currently feels limitless.

To close, I thank you for your attention and time.

Adam Kobelski

APPENDICES

APPENDIX A

CALIBRATING DATA FROM THE *HINODE*/X-RAY TELESCOPE AND ASSOCIATED UNCERTAINTIES

Contribution of Authors and Co–Authors

Manuscript in Appendix

Author: Adam R. Kobelski

Contributions: Implemented part of study design. Managed writing and co-wrote first draft.

Co–Author: Steven H. Saar

Contributions: Helped to conceive study. Implemented part of study design. Co-wrote first draft. Provided feedback of analysis and comments on drafts of the manuscript.

Co–Author: Mark A. Weber

Contributions: Helped to conceive study. Provided feedback of analysis and comments on drafts of the manuscript.

Co–Author: David E. McKenzie

Contributions: Helped to conceive study. Provided feedback of analysis and comments on drafts of the manuscript.

Co–Author: Katharine K. Reeves

Contributions: Helped to conceive study. Provided feedback of analysis and comments on drafts of the manuscript.

Manuscript Information Page

Adam R. Kobelski, Steven H. Saar, Mark A. Weber, David E. McKenzie and Katharine K. Reeves
Solar Physics
Status of Manuscript:
____Prepared for submission to a peer–reviewed journal
____Officially submitted to a peer–reviewed journal
____Accepted by a peer–reviewed journal
__x__Published in a peer–reviewed journal

Published February, 2014, Solar Physics

ABSTRACT

The *X-Ray Telescope* (XRT) onboard the *Hinode* satellite, launched 23 September 2006 by the Japanese Aerospace Exploration Agency (JAXA) is a joint mission between Japan, the United States, and the United Kingdom to study the solar corona. In particular XRT was designed to study solar plasmas with temperatures between 1 and 10 MK with $\approx 1''$ pixels ($\approx 2''$ resolution). Prior to analysis, the data product from this instrument must be properly calibrated and data values quantified in order to assess accurately the information contained within. We present here the standard methods of calibration for these data. The calibration is performed on an empirical basis which uses the least complicated correction that accurately describes the data while suppressing spurious features. By analyzing the uncertainties remaining in the data after calibration, we conclude that the procedure is successful, as the remaining uncertainty after calibration is dominated by photon noise. This calibration software is available in the Solar Soft software library.

Introduction

The *X-Ray Telescope* (XRT) Golub et al. (2007) on *Hinode* (Kosugi et al., 2007) is a high resolution grazing incidence soft X-ray imager launched in 2006. The primary design of the instrument is to measure the hot (thermal) coronal plasma of the sun. Details of the camera system can be found in Kano et al. (2008). To fully understand the significance of the photometric observations and quantify the results, it is necessary to calibrate the data and estimate the remaining noise and uncertainty. The radiometric calibration for quantitative photometric analysis described here is performed to improve the reliability and integrity of XRT data. A set of routines to perform these calibrations is included in the program `xrt_prep.pro` which is available as part of the standard XRT packages within the SolarSoft software library (SSW: Freeland & Handy, 1998).

The standard procedures of data calibration applied to visible light telescopes cannot be fully applied to XRT due to a few factors. In particular, we do not have access to a uniform (spectrally or spatially) X-ray source to make flat fields for calibration in flight, which limits our ability to adjust for temporal instrumental sensitivity variations, thus reducing the options for radiometric calibration. In spite of these complications a robust system of calibration has been developed through empirical analysis. These calibrations are not an attempt to determine every source of data degradation but an empirical correction for all notable sources of data inaccuracy that can accurately be corrected.

In addition to discussing the data calibration, we also provide estimates of the systematic uncertainties remaining after data calibration. This includes the variance from the calibration itself (such as from the vignetting and the dark correction), as well as the uncertainty from non-correctable sources such as JPEG compression. For the latter we provide an analysis of the cause of JPEG compression errors and have developed an accurate estimate of the magnitude of these uncertainties. We have found these errors to be small but notable. Calculations of these systematic uncertainties are available with `xrt_prep.pro`, which provides users a quantifiable measure of the precision of the data. We discuss the magnitude of photon counting errors but have not included these estimates in `xrt_prep.pro`, as they are strongly dependent on assumptions of the conditions within the particular coronal plasma producing the emissions detected by XRT. Included in the discussion are pixel maps returned by the software which locate pixels that are corrected (and thus the user should avoid using) such as pixels affected by dust, contamination and saturation.

In Section A we will discuss the zero-point determination for XRT, which consists of a discussion of dark frames in Section A.1, the odd-even bias voltage readout of the camera in Section A.2, and the *calculation* of the zero point correction is discussed Section A.3. In Section A.4 we discuss the use of Fourier filtering in the calibration, and uncertainties from it in Section A.5. Section A.5 discusses the geometrical (wavelength independent) vignetting. Normalizing the images to a consistent exposure time is discussed in Section A.5. The implications of using JPEG compression are discussed in Section A.5. Section A.5 discusses the pixel maps optionally returned by `xrt_prep.pro`. Undesired signals we do not treat are discussed in Section A.5. We then discuss combining the different sources of uncertainty in Section A.5. We then look at the improvements of the calibration with a test case in Section A.8.

Zero-point Determination

A.1. Dark Overview

Even when no light is incident on the detector, charge will still accumulate, creating extraneous signal. This extraneous signal (along with electronic bias) creates (at a minimum) a zero-point offset that will be present whenever the CCD is read. The calibration system of `xrt_prep.pro` permits the user several methods to correct for this. In some cases it is possible to speculate on the origin of certain effects (*e.g.*, orbital temperature variation of CCD dark current) while in other cases the source of an effect can be unclear (*e.g.*, the exponential portion of the "ski-ramp" dark shape as shown in Figure 17). In many cases, it is not feasible to separate the different noise sources (such as dark and readout noise) and so it is necessary to treat them together. We are primarily concerned throughout with developing an optimum calibration for XRT data, and have not focussed on *why* the instrument behaves in a certain way. We have therefore grouped together various effects which are naturally calibrated at a certain stage, even if they have different root causes (*e.g.*, bias, dark current).

The traditional method of dark correction is direct subtraction of the median (or mean) of contemporaneous dark images taken with the telescope shutter closed. This method of dark correction is available to users of `xrt_prep.pro`, through the optional keyword dark_type=1. In the case of XRT, however, this straightforward method is complicated due to numerous variable noise effects. These variable effects occur on a variety of spatial and temporal scales, and can vary even from one frame to the next. They include an overall ski-ramp shape of the dark along columns, a basal level dependent on CCD temperature and binning, as well as various electronic noise patterns with varying amplitudes and frequencies. Because of this variability, averaging together dark frames, even those taken near in time, can actually increase noise. We have opted, instead, for a semi-empirical approach as the default dark subtraction (dark_type = 0). The approach involves an empirical model dark generated by the routine `lsback_away.pro`, whose parameters have been calibrated based on analysis of over 2000 dark frames as discussed in Section A.3. The mean level of this model dark is then adjusted to conform to the dark frames that are acquired contemporaneously with the X-ray images to be calibrated. A fully empirical model without zero-point adjustment (dark_type = 2) is also included; in Section A.3 we demonstrate that the default zero-point adjusted ("hybrid") model yields the best results, both for recovery of the zero point, and for minimizing noise.

A.2. Odd-Even Bias Voltage Differences

A design feature of the CCD camera sets bias voltages in odd and even pixel columns to slightly different levels (≈ 4 digital numbers (DN) different). This offset is approximately constant in time and its source has not been fully identified. If using direct dark-subtraction (dark_type = 1), this effect is automatically removed from the data. When using the model-based options (including the default), we have opted to correct for this offset by subtracting from half of the columns the median difference between odd and even CCD columns, ignoring pixels where the signal response becomes non-linear (DN > 2500 - hereafter referred to as "saturated"). This correction is performed by the subroutine `no_nyquist.pro` (since the pattern appears at the Nyquist frequency).

A.3. The Dark Frame Model

An XRT dark frame is largely constant along rows (x), though exhibits a distinctive "ski-ramp" profile along columns (y). We found the best functional form with the fewest parameters is given by:

$$F(y) = Ae^{-y/W} + B + Sy \tag{5.1}$$

where $F(y)$ is the flux in DN along y, and A, W, B, and S are fitting constants for a given image (Figure 17). Other functional forms were explored (*e.g.*, polynomials) but none matched the average shape as accurately with so few parameters. Each of the fitting constants has dependencies on other factors. These dependencies were determined by using 2129 darks, each having 2048^2 pixels, taken between mission start and February 2008 and fitting them to Equation (5.1). Smaller numbers of 2×2, 4×4, and 8×8 binned darks (934 total) were also studied to determine variations of the functional form due to pixel binning, N_{bin}. The behavior of the fit parameters with various CCD and exposure properties have been studied. The ramp amplitude A increases non-linearly with exposure time t_{exp}. An approximate fit using a minimum of parameters is described below and illustrated in Figure 18:

$$\begin{aligned}
A(t_{\text{exp}}) &= 4.01 && \text{for } t_{\text{exp}} < 0.1\text{s}, \\
A(t_{\text{exp}}) &= 0.175\, log_{10}(t_{\text{exp}}) + 4.185 && \text{for } 0.1\text{s} \leq t_{\text{exp}} < 4\text{s}, \\
A(t_{\text{exp}}) &= 4.29 && \text{for } t_{\text{exp}} \geq 4\text{s},
\end{aligned} \tag{5.2}$$

where the lower and upper ranges represent the average values of the data when $t_{\text{exp}} < 0.1\text{s}$ and $t_{\text{exp}} > 4\text{s}$ respectively.

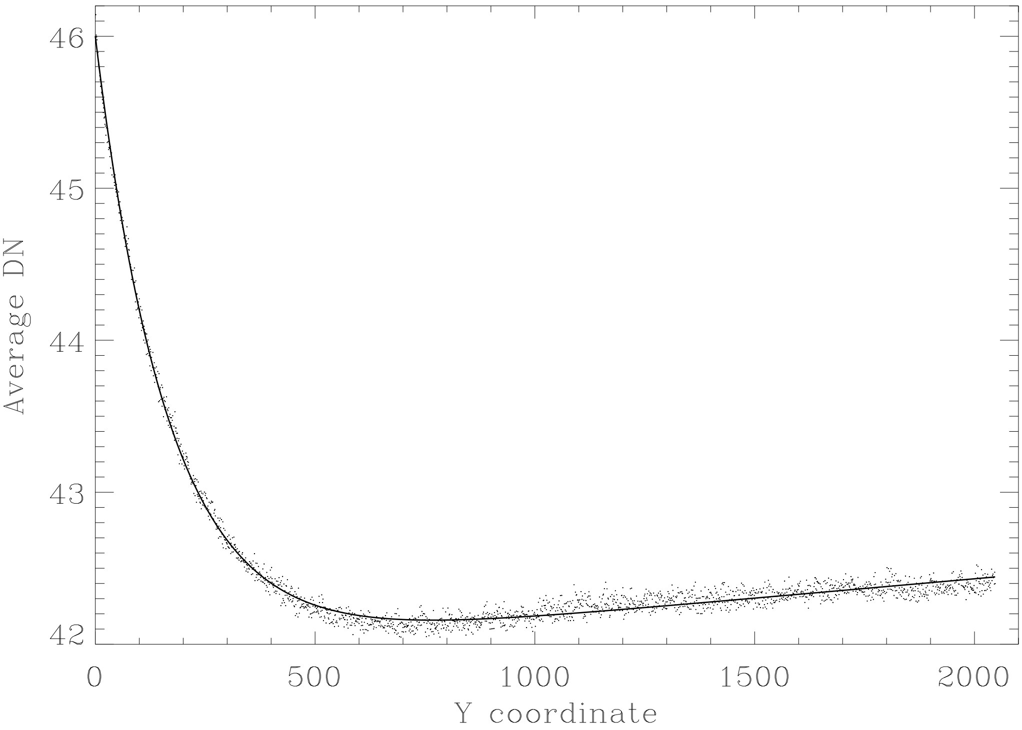

Figure 17: The average column profile of a typical 2048×2048 dark, overplotted with the four parameter “ski-ramp” fit ($\sigma_{\text{fit}} = 0.051$ DN).

The base level B depends primarily on CCD pixel binning ($N_{\text{bin}} \times N_{\text{bin}}$), but shows a secondary dependence on CCD temperature T_{CCD} and t_{exp}. Specifically,

$$B = B_1 + B_2 + B_3 T_{\text{CCD}} + B_4 T_{\text{CCD}}^2, \tag{5.3}$$

where

$$B_1 = 1.44 \times 10^{-3} N_{\text{bin}}^2 t_{\text{exp}}, \tag{5.4}$$

and B_2, B_3, B_4 depend on N_{bin} as shown in Table 12. The dependence of B on T_{CCD} is shown in Figure 19 for $N_{\text{bin}} = 1$ (*i.e.* full-resolution) as an example.

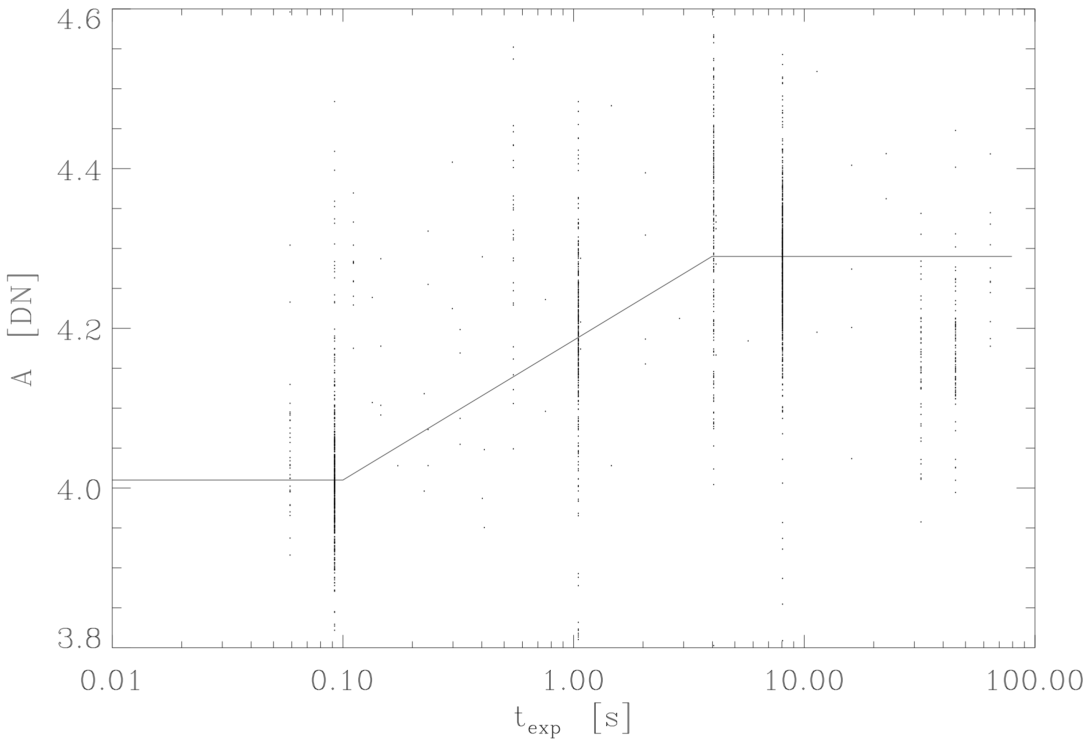

Figure 18: Fit of the dependence of the "ski-ramp" amplitude parameter A on exposure time.

N_{bin}	B_2	B_3	B_4
1	86.08	0.1695	1.955×10^{-3}
2	247.84	2.459	2.349×10^{-2}
4	517.65	4.425	3.805×10^{-2}
8	1067.09	8.898	7.647×10^{-2}

Table 12: Variation of base level coefficients from Equation (5.3) with CCD pixel binning for the dark frame model.

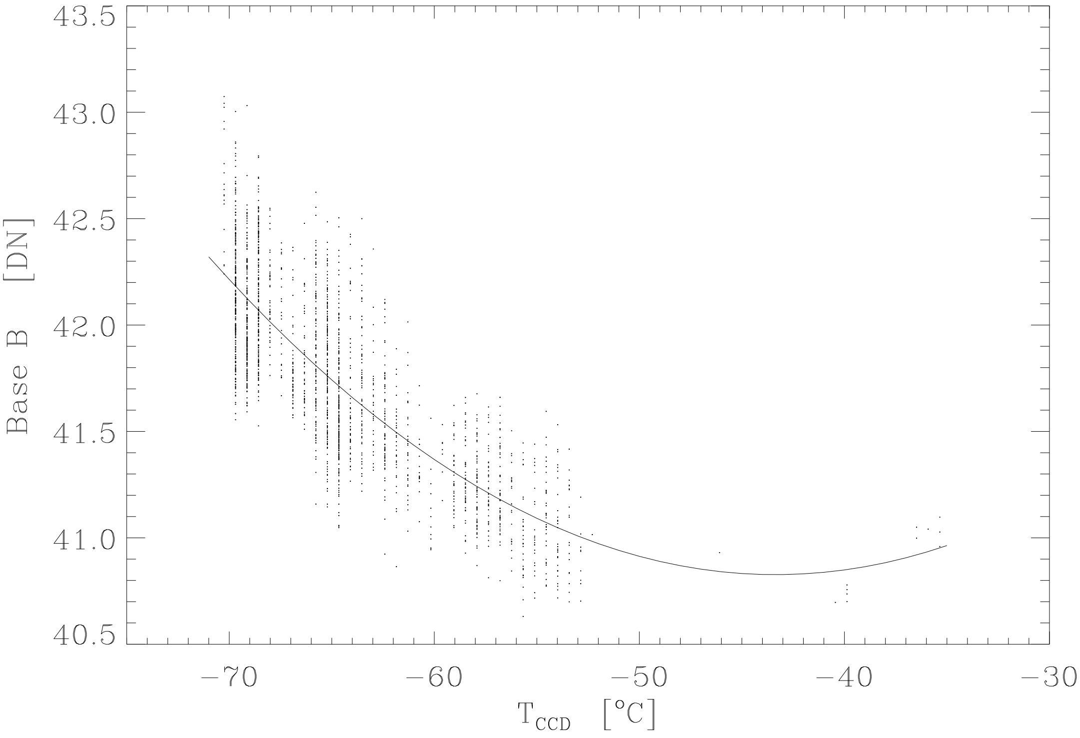

Figure 19: Quadratic fit of the dependence of "ski-ramp" base parameter B on CCD temperature for 1x1 binning.

The ramp width parameter W decreases with CCD pixel binning as

$$W = 188.2 - 8.43 \times N_{\mathrm{bin}}. \tag{5.5}$$

This dependence is shown in Figure 20. The slope S increases slightly with T_{CCD} as

$$S = 4.56 \times 10^{-4} + 2.52 \times 10^{-6} T_{\mathrm{CCD}} \tag{5.6}$$

which is shown in Figure 21. Smaller fields of view have the dark profile of the corresponding *bottom* portion of a full-frame dark, *i.e.*,

$$D(x_1 : x_2, y_1 : y_2) = D_{\mathrm{full-frame}}(x_1 : x_2, 0 : y_2 - y_1). \tag{5.7}$$

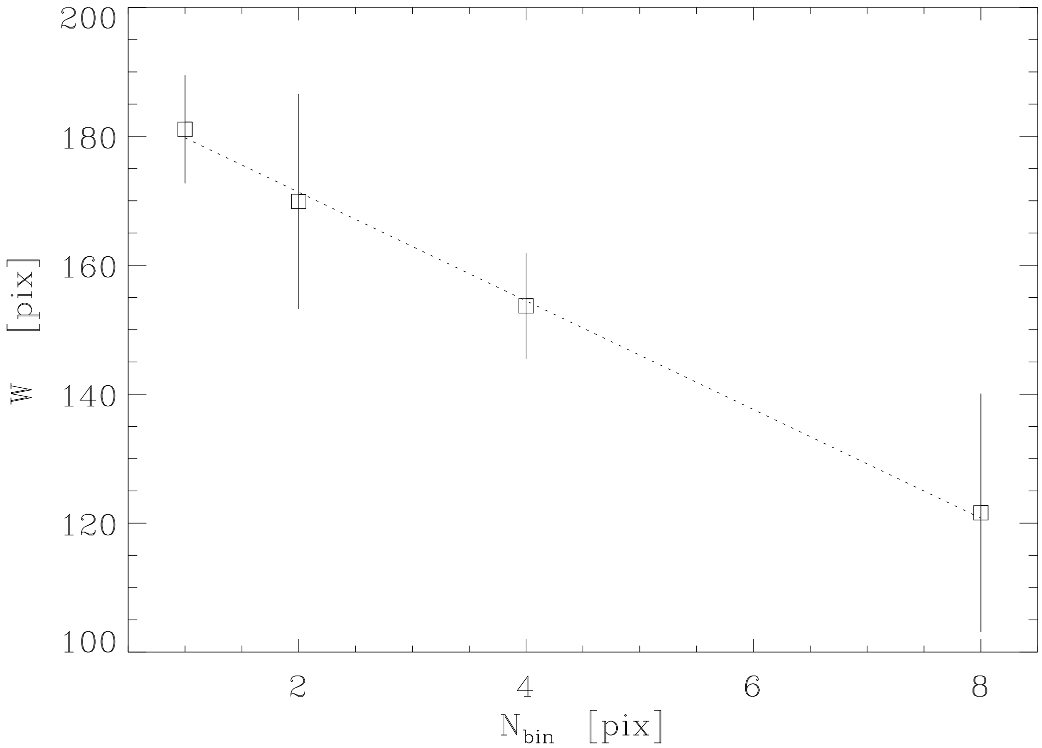

Figure 20: Fit of the dependence of the “ski-ramp” width parameter W.

Optimally, the arithmetic difference between an observed dark frame, D_i, and a model dark $D_{\mathrm{mod},i}$, would yield a frame with a mean of zero and only random noise remaining. To test the dark model for deviations from this ideal, we analyzed all of our test darks to determine two simple measures of the goodness-of-fit: the scatter of the average residual $\langle D_i - D_{\mathrm{mod},i}\rangle$, *i.e.*

$$\sigma_{\langle D-D_{\mathrm{mod}}\rangle} = [\Sigma_i^N \langle D_i - D_{\mathrm{mod},i}\rangle^2/(N-1)]^{0.5} \tag{5.8}$$

and the average of the scatter *within* the residuals:

$$\langle \sigma_{D-D_{\mathrm{mod}}}\rangle = \langle [\Sigma_i^N (D_i - D_{\mathrm{mod},i})^2/(N-1)]^{0.5}\rangle. \tag{5.9}$$

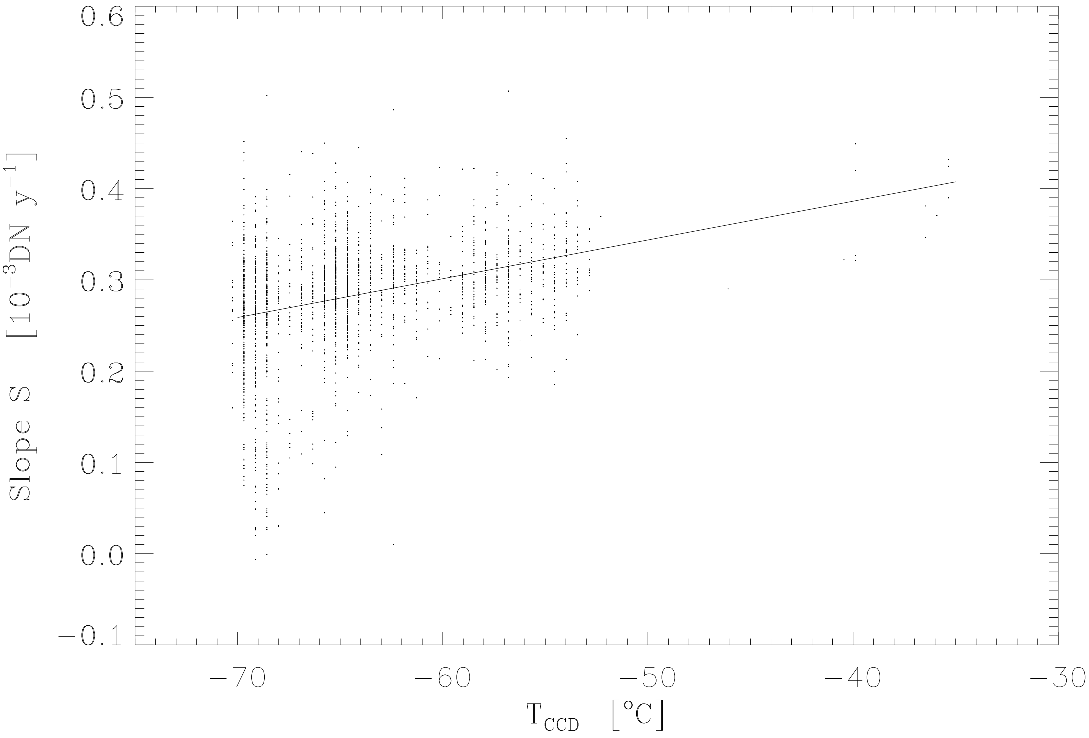

Figure 21: Linear fit of dependence of “ski-ramp” slope parameter S on CCD temperature.

Since we have adjusted B so that the average over all residuals is zero, the first diagnostic, $\sigma_{\langle D-D_{\mathrm{mod}}\rangle}$, essentially gives a measure of the scatter in the zero-point determination. The second, $\langle\sigma_{D-D_{\mathrm{mod}}}\rangle$, gives a measure of how well the model matches the 2-D dark *shape*.

The values of the constants in Equation (5.1) have been computed for the entire set of 2129 darks. We also computed analogous values for the case where the dark model, D_{mod}, is defined as the median of the five dark frames taken nearest in time to the dark to be corrected. We found that the model dark was better at determining the shape of the dark with the lowest scatter ($\langle\sigma_{D-D_{\mathrm{mod}}}\rangle$) while the traditional median was better at reducing scatter in the zero-point amplitude ($\sigma_{\langle D-D_{\rm mod}\rangle}$). There were systematic deviations in the zero-point level on intermediate timescales (≈months) which were uncorrected by the pure model dark. These uncorrected deviations led us to develop a hybrid model as the default for `xrt_prep.pro`, wherein the average of the model dark is then adjusted to match the average of the median of the five temporally nearest dark frames. The values for $\sigma_{\langle D-D_{\rm mod}\rangle}$ and $\langle\sigma_{D-D_{\rm mod}}\rangle$ are then used to compute the combined uncertainties introduced by dark subtraction and bias correction such that

$$\sigma^2_{\rm dark} = \langle\sigma_{D-D_{\rm mod}}\rangle^2 + \sigma^2_{\langle D-D_{\rm mod}\rangle}. \tag{5.10}$$

Results of the analyses are shown in Figures 22, 23, and 24. Note that the number of points in each case is less than the total number analyzed, as some points were removed for excessive radiation hits, or in the cases using median darks, there were insufficient darks of adequate type and quality to generate the median $D_{\rm mod}$.

One can clearly see in Figure 22 that the median and median-adjusted (lower panel of Figure 22) hybrid models show lower scatter in the zero-point $\sigma_{\langle D-D_{\rm mod}\rangle}$ than the pure model adjustment (upper plot in Figure 22), mostly because many intermediate timescale trends are removed. We note that $\langle\sigma_{D-D_{\rm mod}}\rangle$ splits into multiple, roughly fixed levels (Figure 23). These levels are primarily due to the data compression level Q (Figure 24 and JPEG compression discussion in Section A.5); compression acts to alter high frequencies in the data, altering high frequency noise. Using the median $D_{\rm mod}$ (Figure 24, right) shows higher average $\langle\sigma_{D-D_{\rm mod}}\rangle$ with a larger range at each Q

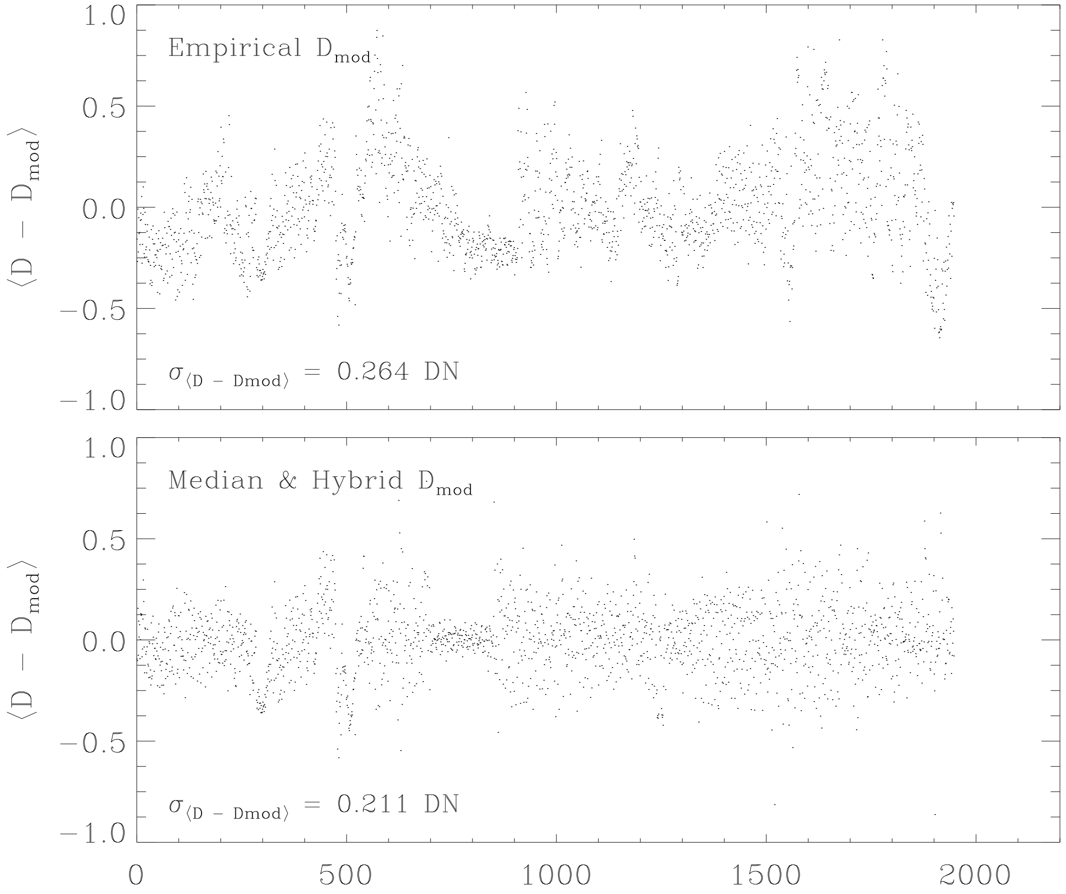

Figure 22: Plots of $\langle D - D_{\rm mod}\rangle$ (in DN) for full-frame images with 1×1 binning. The upper plot uses an empirical model dark (dark_type = 2) for $D_{\rm mod}$. The lower plot uses a median of five dark frames (dark_type = 1). The results for $D_{\rm mod}$ (dark_type = 1) and hybrid $D_{\rm mod}$ (dark_type = 0) are identical. Note the reduced scatter in the cases of dark_type = 1 or 0 quantified by the lower value of $\sigma\langle D - D_{\rm mod}\rangle$.

because of intrinsic noise in $D_{\rm mod}$ compared to the (noise-free) analytic models. There are also some added semi-fixed levels of $\langle\sigma_{D-D_{\rm mod}}\rangle$ when compared to the analytic models. These semi-fixed levels appear to be due to a combination of Q mixtures in median $D_{\rm mod}$, and the effects of varying numbers of radiation hits for some Q values.

Fourier filtering

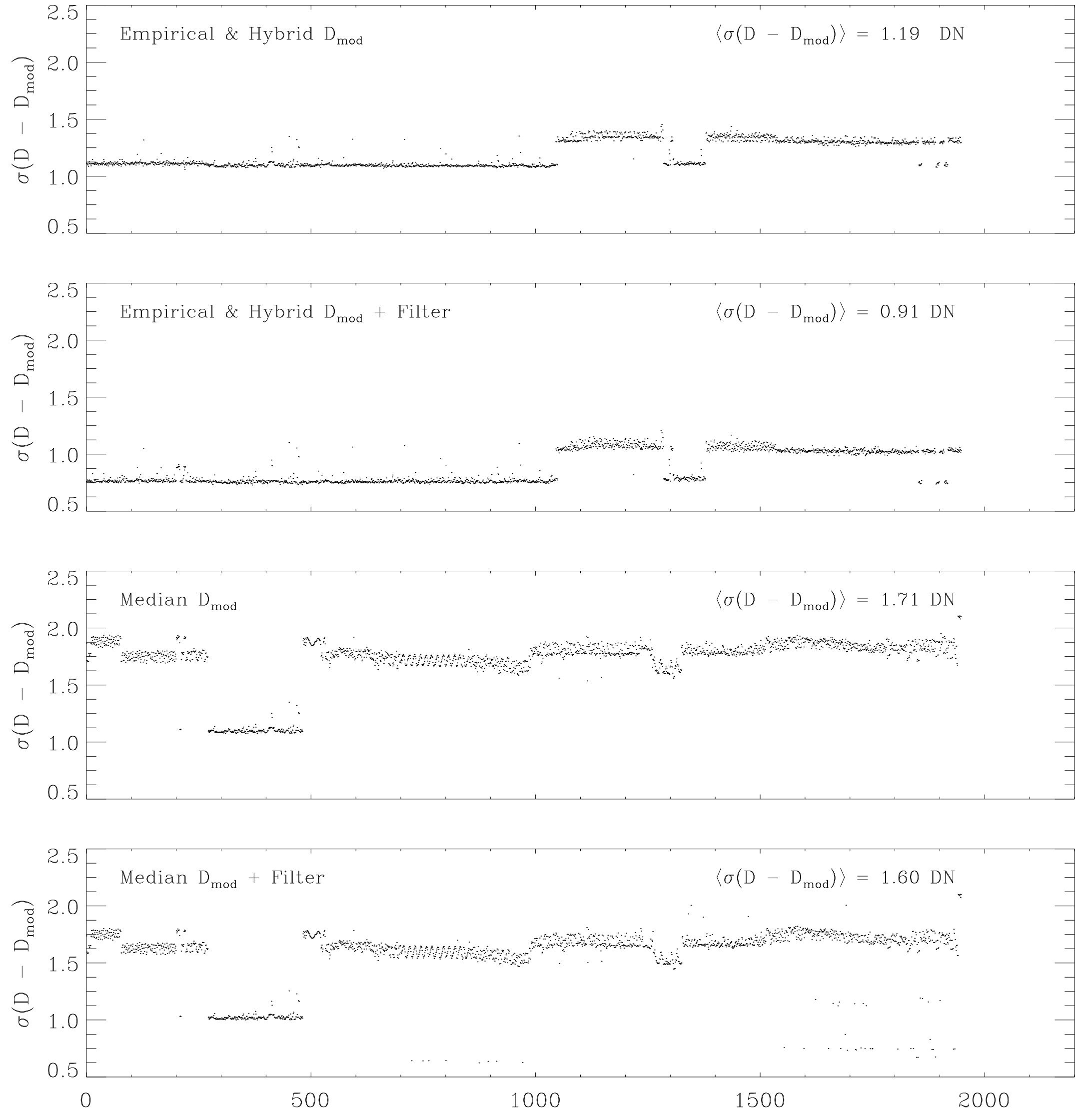

Figure 23: Plots of $\sigma(D-D_{\mathrm{mod}})$ (in DN) for full frame images with 1×1 binning. The top plot is for cases using the empirical or hybrid D_{mod} (dark_type = 0 or 2), and the second plot is for the same cases but Fourier filtered (see discussion on Fourier filtering in Section A.4). The lower two plots are for median filtered D_{mod}(dark_type = 1), with the lowest plot including Fourier filtering. Note the Fourier filtering reliably lowers $\sigma(D-D_{\mathrm{mod}})$. The different discrete levels visible are due to changes in $\langle\sigma(D-D_{\mathrm{mod}})\rangle$ due to different JPEG compression levels (more details in Section A.5); in the case of dark_type = 1, additional levels are added for mixtures of compression type within a D_{mod}. The noise reduction for the case of dark_type = 1 and full Fourier noise removal is due to the reduction of high frequency noise in the medianing, which leaves less periodic signal for the filter to remove.

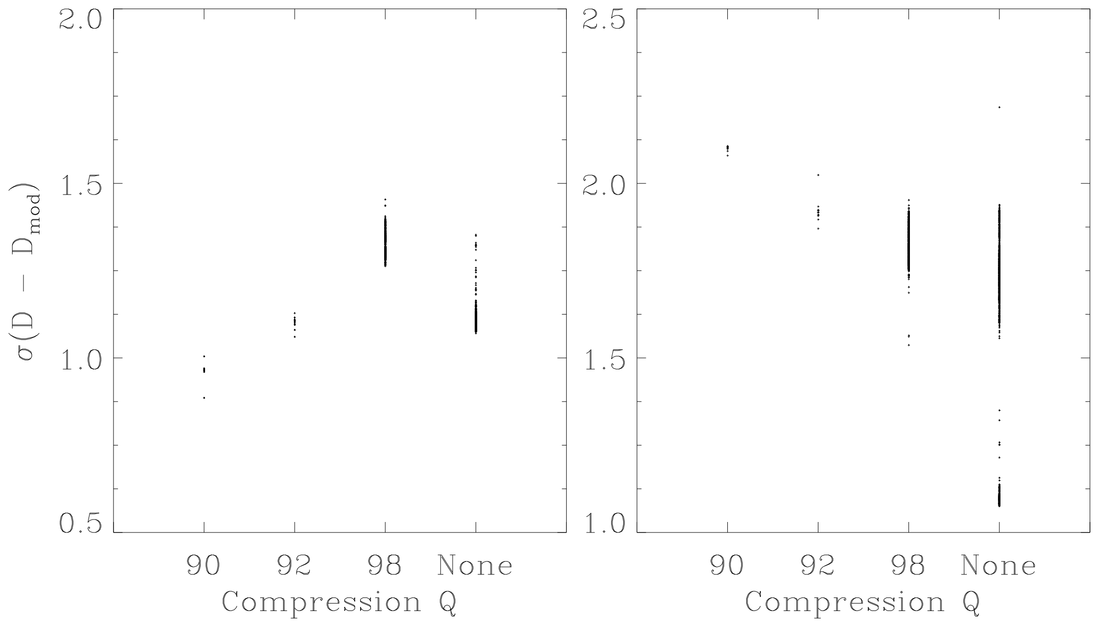

Figure 24: Plots of $\sigma(D - D_{\rm mod})$ as a function of compression level Q, showing scatter about distinct mean levels which vary with Q and dark_type (left panel, model $D_{\rm mod}$, dark_type = 0, 2; right panel, median dark $D_{\rm mod}$, dark_type = 1). The median model (right) shows higher average values (due to noise in $D_{\rm mod}$) and multiple concentrations at a given Q, caused in part by mixtures of different Q values used to create the median dark.

A.4. Fourier Filtering

All XRT data exhibit moderate to high frequency “ripples” whose amplitudes and frequencies change in time. While the amplitude of these features is small (a few DN), they can nevertheless be troublesome, especially in fainter parts of an image and portions where the intensity gradients are small (making quasi-regular variations more noticeable). Due to their relatively low amplitudes, the features are most easily seen in dark frames, where the signal level is low and nearly flat. These features do not completely cancel out, even when fairly large numbers of darks are averaged, because of rapid frame-to-frame variability. These features can be easily discerned in Fourier transforms (Figure 25) and come in several varieties: type 1) features with constant horizontal and vertical frequency (ν_x and ν_y, respectively) and variable amplitudes; type 2) features with constant ν_x, but spanning all ν_y with variable amplitude $[a(\nu_y, t)]$; type 3) features with constant ν_x and variable amplitude $[a(\nu_y, t)]$, but in the shape of a moving pulse in ν_y, dropping to 0 outside a limited ν_y range. The temporal variation of these features can be seen in Figure 26. Type 2 and 3 features are more pervasive than type 1 features.

Each data image is corrected with the procedure `xrt_fourier_vacuum.pro`, which applies a tapered filter to each of these features in Fourier space, suppressing them down to the average noise level measured local to, but outside of, the feature. Two thresholds are used in the filtering. The first threshold is n_{sig}, the number of standard deviations above local fluctuations (in Fourier space) a signal must be before it is suppressed. The second is n_{med}, the threshold in Fourier amplitude (in standard deviations above the median large-scale Fourier noise level) above which no corrections are performed. This threshold avoids damaging the "real data" part of the transform. Thus, n_{sig} controls how strong a Fourier feature must be before it is suppressed, and n_{med} governs what part of the transform is considered "real data" by the program and shielded from any alteration. The default values of these parameters are set to $n_{\mathrm{med}} = 3.5$ and $n_{\mathrm{sig}} = 4.5$.

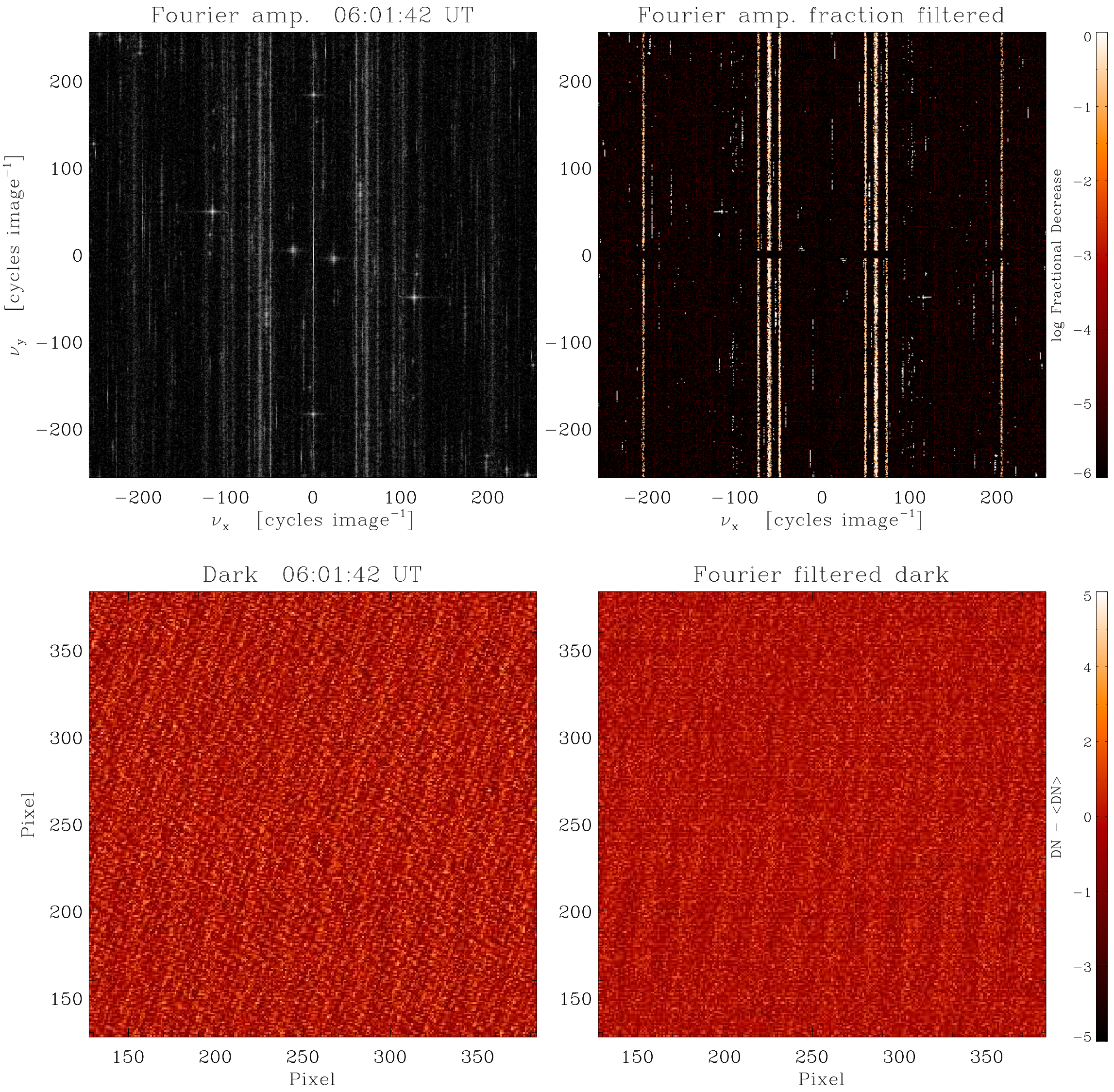

Figure 25: Top left: 2-D FFT of a dark taken on 6 November 2006, log-scaled and thresholded between 10^{-1} and 10^{-3}, showing typical noise features (*e.g.*, localized peaks, streaks spanning ν_y at fixed ν_x, and pulses with fixed ν_x and restricted ν_y). Top right: Log of the fraction of the Fourier amplitude which is filtered out of the same dark by the `xrt_fourier_vacuum.pro` routine (scale at right). Bottom left: Central 256×256 pixels of the same dark (after "ramp" and Nyquist removal) before Fourier filtering. Bottom right: Same as bottom left, after filtering (scale for both bottom panels is at right). Note that high frequency periodic noise is suppressed, but some lower frequency noise remains, due to shielding of low ν portions of the transform to prevent damage to actual data signals.

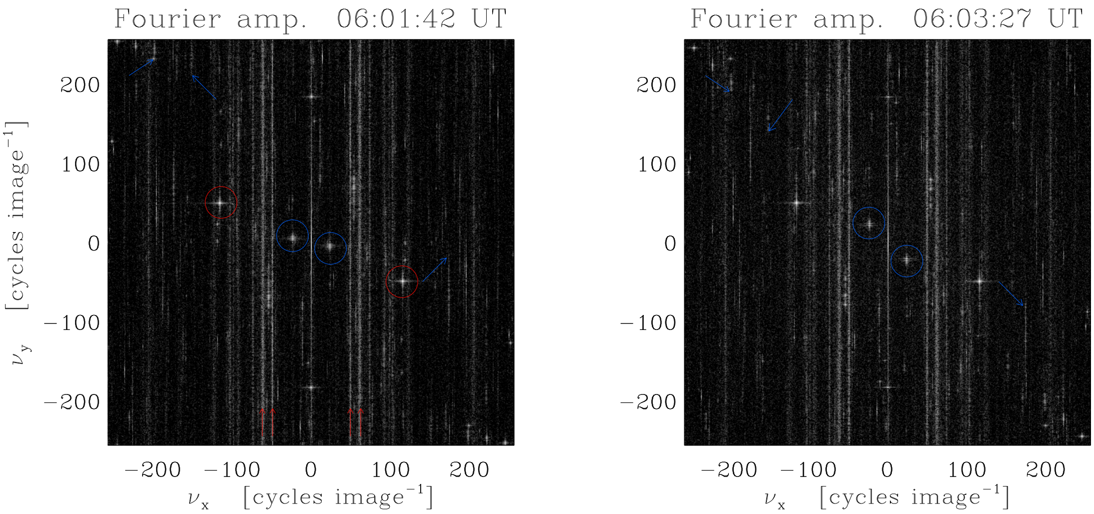

Figure 26: Left: Same 2-D FFT shown in Figure 25 (top right) with some typical noise features; localized peaks fixed in ν_x and ν_y (circled in red), streaks spanning ν_y at fixed ν_x (red arrows), and peaks (blue circles) and pulses (blue arrows) with fixed ν_x and variable ν_y. Right: 2-D FFT of a dark taken ≈ 2 min later, displayed as in left panel. Note the motion in ν_y of some of the marked features (blue), corresponding to a different noise ripple pattern in the dark (compare Figure 25 bottom panels).

Generally features of type 1 and 2 are well removed from the solar parts of the transform. Due to their variability in ν_y, noise features of type 3 can sometimes remain uncorrected in the final product. An image of a dark frame before and after Fourier filtering is shown in Figure 25.

A.5. Fourier Filter Uncertainties

We have computed the average effect of the Fourier filtering, which typically reduces the scatter $\langle\sigma_{D-D_{\mathrm{mod}}}\rangle$ by $\approx 25\%$ (in the 1x1 binning case), though the reduction is less for higher binning levels. This reduction in scatter for the dark correction from Fourier filtering is included in the calculation of the dark uncertainty described in Equation (5.10). While generally improving the noise floor of XRT, the use of a Fourier filter to suppress temporally variable readout signals is not without drawbacks and sources of uncertainty. Although we have taken great pains to design the Fourier filter such as not to damage the real data, uncertainties in the best choice of n_{sig} and n_{med} for a given data set make some added error unavoidable. In addition, some error is introduced by the inadvertent removal of "real" information at ν_x and ν_y. Thus, while suppressing the spurious readout signals, we introduce small errors due to imperfections in the filtering process itself. Specifically, uncertainties arise in imperfections from how the filter process protects "real" data. To estimate the uncertainty in the filtering process, we altered both parameters (n_{sig} and n_{med}) by ±1 and computed a Fourier filter error amplitude image σ_{FF}:

$$\sigma_{\mathrm{FF}} = [(I_{\mathrm{n}_{\mathrm{sig}}^{+}} - I_{\mathrm{n}_{\mathrm{sig}}^{-}})^2 + (I_{\mathrm{n}_{\mathrm{med}}^{+}} - I_{\mathrm{n}_{\mathrm{med}}^{-}})^2]^{0.5}, \tag{5.11}$$

where $I_{\mathrm{n}_{\mathrm{sig}}^{+}}$ is the Fourier filtered image with n_{sig} increased by 1 unit, $I_{\mathrm{n}_{\mathrm{sig}}^{-}}$ is the Fourier filtered image with n_{sig} decreased by 1 unit, and so on. We then attempted to model σ_{FF} using various image properties.

It was found that σ_{FF}, above a base level, is mostly comprised of "islands" of enhanced noise in areas of the image with sharp gradients (*e.g.*, near active regions).

It was determined that $\sigma_{\rm FF}$ can be reasonably modeled with a properly trimmed, scaled and smoothed version of the original image, according to

$$\sigma_{\rm FF} = B_{\rm FF} + \mathrm{smooth}^4((I > C_{\rm FF}), n_{\rm smoo})/D_{\rm FF} \qquad (5.12)$$

where $B_{\rm FF}, C_{\rm FF}, n_{\rm smoo}$, and $D_{\rm FF}$ are fitting parameters, and $\mathrm{smooth}^4()$ represents an $n_{\rm smoo}$ pixel running mean unweighted ("boxcar") smoothing, reiterated four times. We studied groups of ≈8 unbinned full frame images, with varying filters and exposure times, from mission start (October 2006) to May 2008. Each group represented data from one month. We found a value of $C_{\rm FF} = 50$ DN to be a suitable intensity threshold for fitting the data. The other parameters were determined using non-linear least squares fitting across image parameters. Numerous combinations of image parameters were tested, but the best fits were achieved with the mean data level $\langle I \rangle$ and the average unsigned amplitude of the local spatial gradient of the image ($\langle |dI/dz| \rangle$, where dI/dz is the 2-D spatial derivative of the image I using 3 point Lagrangian interpolation via the IDL `deriv.pro` function).

There was a notable change in the functional dependence of $\sigma_{\rm FF}$ once the XRT CCD became affected by contamination spots in July 2007 Narukage et al. (2011) and again in January 2008. Thus we model $\sigma_{\rm FF}$ separately for the three epochs defined by the contamination spots (*i.e.*, pre-July 2007, July 2007 through January 2008, and post-January 2008). For these three epochs, the best-fit parameters are given in Table 13. The likely cause of the variation is the introduction of numerous small sharp "edges" from the spots themselves. While individually the gradients induced

Table 13: Coefficients for Fourier filter uncertainty σ_{FF} for three epochs defined by absence or presence of CCD contamination spots. Epoch I = prior to 24 July 2007; Epoch II = 24 July 2007 through 20 January 2008; Epoch III = after 20 January 2008. For each coefficient, the residual scatter in the fitting is expressed as the error in the *logarithm of the coefficient.*

Epoch	B_{FF}	D_{FF}	n_{smoo}
I	$0.24\ \langle\lvert dI/dz\rvert\rangle^{1.22}$	$26\ \langle\lvert dI/dz\rvert\rangle^{-3.40}\langle I\rangle^{1.70}$	$\mathrm{round}[40\ \langle\lvert dI/dz\rvert\rangle^{-0.53}\langle I\rangle^{0.53}]$
	$\sigma_{\mathrm{B}} = 0.224$	$\sigma_{\mathrm{D}} = 0.463$	$\sigma_{\mathrm{n}} = 0.263$
II	$0.26\ \langle\lvert dI/dz\rvert\rangle^{1.19}$	$77\ \langle I\rangle^{0.55}$	$\mathrm{round}[26\langle\lvert dI/dz\rvert\rangle^{-0.54}\langle I\rangle^{0.54}]$
	$\sigma_{\mathrm{B}} = 0.183$	$\sigma_{\mathrm{D}} = 0.368$	$\sigma_{\mathrm{n}} = 0.438$
III	$0.26\ \langle\lvert dI/dz\rvert\rangle^{1.18}$	$79\ \langle I\rangle^{0.59}$	$\mathrm{round}[28\langle\lvert dI/dz\rvert\rangle^{-0.33}\langle I\rangle^{0.49}]$
	$\sigma_{\mathrm{B}} = 0.160$	$\sigma_{\mathrm{D}} = 0.453$	$\sigma_{\mathrm{n}} = 0.447$

by the spots are (typically) on a smaller spatial scale than those of active regions, they are considerably more numerous and more spatially uniform. In summary, the base level increases with the scale of gradients in the image. During the non-spotted epoch, the normalization depends on the average counts, and inversely with the image gradients; after the formation of contamination spots, D_{FF} primarily depends on the mean count rate.

The parameters in Table 13 are appropriate for full-resolution images. Based on test cases, the scaling to other binnings is found to be well described by

$$\sigma_{\mathrm{FF}}(N_{\mathrm{bin}} > 1) = N_{\mathrm{bin}}^{-1.5}\sigma_{\mathrm{FF}}(N_{\mathrm{bin}} = 1). \qquad (5.13)$$

This model is not a precise pixel-for-pixel match to σ_{FF}, but rather follows its larger scale structure. Errors scatter around this model on a fine scale. Overall, Fourier filter errors are a minor component of the overall error budget, as will be shown further below.

Vignetting

In the astronomical community there is an ambiguity in describing vignetting, with some authors using the term to describe only the geometrical factors that result in uneven illumination of the focal plane (*e.g.* due to obscuration by baffles), and other authors using the term to describe all possible effects including, *e.g.*, wavelength-dependent reflectivity of a grazing incidence mirror. In the present work, we conform to the former usage, wherein only geometrical effects independent of the wavelength of incident photons are considered. A known source of wavelength-dependent variation of illumination, other than the reflectivity of grazing incidence telescopes, is photon scattering due to residual roughness of the mirror. Correcting for photon scattering or for wavelength-dependent reflectivity requires knowledge of the photon wavelengths, which in the case of a broadband instrument like XRT is only possible with knowledge of the temperature-dependent emission measure and element abundance of the observed plasma. Such a strongly model dependent analysis is clearly outside the scope of this calibration. However we note that a wavelength-dependent vignetting in the case of XRT should be expected to manifest as a systematic bias of filter-ratio temperatures with respect to off-axis angle, an effect which to our knowledge has not been observed.

The effect of vignetting in XRT was measured before launch at the X-ray Calibration Facility at NASA's Marshall Space Flight Center in Huntsville, AL during the end-to-end testing. As the telescope was tested in its fully assembled configuration, and with monochromatic Cu-Lα photons, these tests included all sources of non-uniform illumination of the focal plane within the optical path and focused on the wavelength independent and rotationally symmetric sources of vignetting.

We fit the measured CCD response as a function of off-axis angle θ with a linear function, normalized to 1 at $\theta = 0$. The mirror vendor provided a functional vignetting of the form

$$V(\theta) = 1.0 - 2/3(\theta/\theta_{\mathrm{graze}}) \tag{5.14}$$

where $\theta_{\mathrm{graze}} = 54.6'$, the manufacturer specified graze angle of the mirror. However, the end-to-end testing measurements did not sample enough off-axis positions to fully populate the image plane, and so interpolation/extrapolation from the sparsely sampled data points does not provide sufficient precision to determine the vignetting function uniquely. At the same time, the end-to-end testing gave no clear evidence for deviations from the expected vignetting profile, a result which indicates that the mirror is the only significant component contributing to vignetting in the focal plane. Later analysis of solar images made at different spacecraft pointings with respect to Sun center supported the conclusion that Equation (5.14) adequately represents the vignetting detected in XRT images, in all four of the thinnest focal plane analysis filters (Ishibashi, 2008, private communication).

The vignetting is corrected by the `nono_vignette.pro` program which divides the image by this function, reversing the effects of vignetting. Errors due to the fit remaining after the correction were determined from additional study of the scatter in the dither analysis data mentioned above (Ishibashi, 2008, private communication). We found:

$$\begin{aligned} \sigma_{\mathrm{V}} &= 0.0045 && (\theta \leq 9.916'), \\ \sigma_{\mathrm{V}} &= 0.0215 - 0.0061\theta + 0.00044\theta^2 && (\theta > 9.916'). \end{aligned} \tag{5.15}$$

In the central region of the CCD, the vignetting uncertainty is quite reasonable (0.45%), though it does get large (> 10%) near the edges of the full field of view. It is worth noting that while the X-ray intensities (and thereby emission measures) measured from off-axis sources are affected by the vignetting, since the vignetting function is multiplicative and wavelength independent, ratios of the intensities are unaffected.

Exposure Time Normalization

XRT uses a rotating focal plane shutter with three differently-sized slots to control the amount of time that the detector is exposed Golub et al. (2007). A variety of exposure lengths can be achieved by rotating the shutter through a combination of slots. The CCD is flushed at the beginning of the exposure and read immediately after the end of the exposure, to minimize the accrual of stray light and dark current.

The actual length of time the CCD is exposed to light is measured by an optical encoder on the shutter and noted in the image header (under the keyword `e_etim`), and used by `xrt_prep.pro` to normalize the images. Thus the uncertainty in the exposure time is limited by the precision of the stored value which is of order 10^{-6}s, and thus negligible compared to the other sources of uncertainty.

JPEG Compression

In 2007, the transceiver for *Hinode*'s X-band antenna failed, forcing all scientific telemetry to use the lower bandwidth of the S-band transceiver. To accommodate this lowered telemetry, the instruments on *Hinode* have used a stronger compression than the lossless algorithm, DPCM, to conserve telemetry. The alternative compression algorithm adopted is the lossy algorithm of the Joint Photographic Experts Group (JPEG). JPEG compression is one of the most commonly used consumer file compression algorithms, and the file format is ubiquitous in digital photography. The compression is a multistep process and is performed by the Mission Data Processor (MDP) on board the spacecraft. It is very useful to understand the mechanism of JPEG compression in order to understand and calculate the errors caused by the compression. We find (and show below) that even though visible artifacts of the JPEG compression can be detected in some X-ray images, the photometric magnitude of the uncertainty is quite small, on the order of 2–3% for typical images of coronal active regions.

The first step in JPEG compression is to center the data around zero to prepare it for a discrete cosine transform (DCT). The centering is performed by subtracting a pedestal equal to half of the bit limited range of the data. The second step is to subdivide the image into N pixel by M pixel subregions (hereafter referred to as macropixels). Most JPEG compression algorithms, including that used on *Hinode*, utilize macropixels made of 8 pixel by 8 pixel subregions. A DCT is then applied independently to each macropixel.

The transformed macropixel is then normalized by a quantization table which suppresses the high frequency signals. The strength of JPEG compression is determined and denoted by the particular quantization table used. The high frequency information in the data is lost when the array is recast as an integer array after normalization, which truncates low signal values to zero. By storing only the non-zero amplitudes of the low frequencies by the use of Huffman entropy encoding, high frequency data is discarded and a smaller file size is achieved. The compressed file size depends on the amount of high frequency signal in the original data as well as the particular compression array used. Decompression is performed by reversing the compression process.

For XRT the compression level ranges from $Q100$ to $Q50$. The $Q100$ compression loses minimal information (generally just round-off error), and creates a file $\approx$22% of the size of the raw image and $\approx$66% the size of a DPCM compressed image. The $Q50$ compression shrinks the file to just $\approx$2% of the raw image and $\approx$6% of the DPCM compression, though such high compression significantly alters the original image and is thus rarely used.

The level of compression involved in science level JPEG compression (typically $Q92$ and $Q95$) is significantly lower (*i.e.*, less lossy) than commonly used in consumer applications. Also, coronal images often have less high frequency information than is found in consumer images (such as caused by text or hard edges), which makes JPEG artifacts less common in science images than in consumer digital photography. Apart from numerical rounding error, the nature of the transformation generally conserves flux within each macropixel. Most of the error we observe comes about from smearing the high frequency components throughout the macropixel.

To determine the uncertainty created by JPEG compression, we applied JPEG compression to 1253 images of size 512×512 (pixels) obtained from different science datasets that had used DPCM compression. Compression was performed using an algorithm designed to mimic the method and computational architecture of the MDP. We then studied the discrepancy between the original and compressed images. A discrepancy histogram is shown in Figure 27. The discrepancy does not follow a single Gaussian distribution, suggesting a more sophisticated approach of determining the uncertainty is required.

The most efficient proxy found for the uncertainty in JPEG compression is the range of values within a macropixel. Generally speaking, the larger the range of values within the macropixel, the more high frequency signal within the region for JPEG compression to suppress. Thus the more high frequency signal within a given macropixel, the larger the compression error. Since flux is generally conserved in

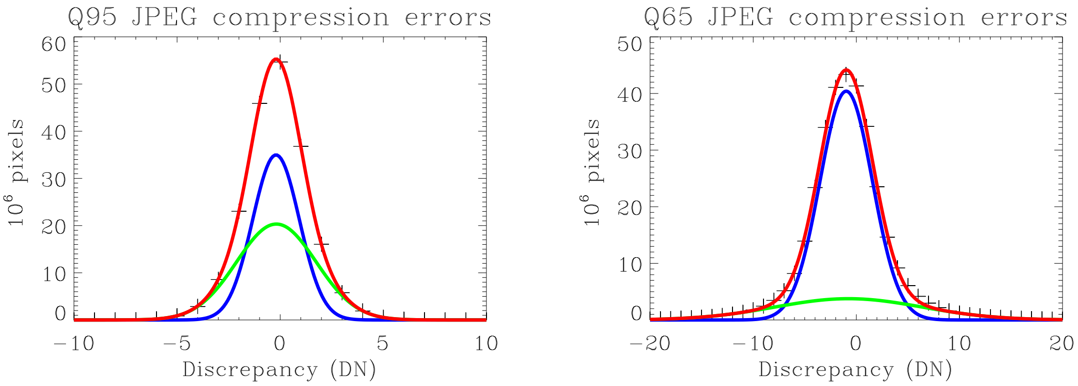

Figure 27: Histogram of discrepancies from $Q95$ (low) and $Q65$ (high) compression when compared to the uncompressed data. A single Gaussian does not provide a sufficient fit. The data can be fit by two separate Gaussians, as shown. The blue and green curves represent the two individual Gaussians used, with the red curve representing the sum of these curves.

a macropixel, this results in the smearing that creates the notorious JPEG "block" artifacts.

As suggested by these factors, we find the largest uncertainty from JPEG compression occurs on the edges of active regions, where the signal rapidly transitions from a few DN/pixel in the quiet sun to well over a thousand DN/pixel in the active region. Utilizing data from the large data set of 1253 images, we have made histograms of the average absolute discrepancy per macropixel for each possible value of the (maximum - minimum) pixel range within a macropixel. These histograms are easily fit by Gaussians. The center of these Gaussians gives the JPEG compression uncertainty for each pixel within the macropixel, as is illustrated in Figure 28. We use these empirically determined values to determine estimates of the uncertainty in `xrt_prep.pro`. The software determines the max-min value for each macropixel of

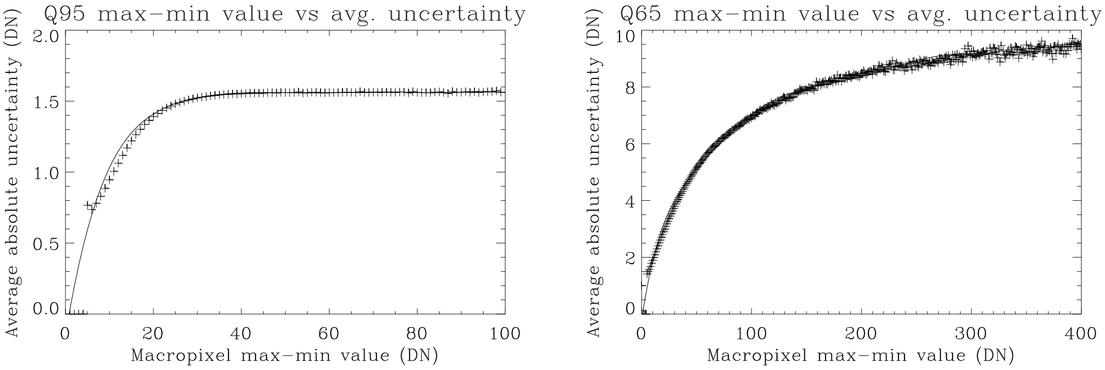

Figure 28: Plot of the average macropixel max-min values vs absolute uncertainty for $Q95$ and $Q65$ compression (+). Overplotted is a best fit polynomial line which is spliced with the asymptotic value of the curve. This piecewise continuous curve is used by `xrt_prep.pro` to calculate the JPEG uncertainty.

JPEG Q value	Asymptotic uncertainty (DN)
100	0.3
98	0.7
95	1.55
92	2.45
90	3.1
85	4.5
75	7.0
65	10.0
50	15.0

Table 14: Asymptotic uncertainty for varying JPEG compression Q factors. These values of uncertainty are the asymptotes of the average uncertainty per macropixel for each max-min value, as shown in Figure 28.

the image and assigns each macropixel an uncertainty using best fit curves as shown in Figure 28. The asymptotic value of the average uncertainty per macropixel for the available values of Q is shown in Table 14. It is important to remember that the values in Table 14 are asymptotes of the max-min vs average error graphs (Figure 28) and not maximum errors nor are they strictly average errors.

Pixel Maps

There are several properties/effects of the CCD which are noted and mapped by `xrt_prep.pro` but not otherwise corrected, often because there is no demonstrably reliable way of making a quantitative correction. Certain useful maps are available as optional outputs of `xrt_prep.pro`. Each effect has been assigned a unique grade in the maps.

Pixels missing in telemetry are replaced by the local data average and noted in the missing pixel map. Saturated pixels (DN > 2500, grade $= 1$), so-called saturation "bleed" pixels (where charge transfer from saturated pixels has corrupted values; grade $= 2$), contamination spots (grade $= 4$), dust speck (grade $= 8$) and possible "hot" pixels (grade $= 16$) are flagged in the pixel grade map, an output of `xrt_pixel_grade.pro`.

Contamination spots were first seen as the result of the first CCD bakeout on 23 July 2007, where an unknown organic contaminant collected in spots on the CCD Narukage et al. (2011). The data are checked after each CCD bakeout and the spots are periodically remapped. These spots are partially opaque to X-rays, particularly at the longer wavelengths normally admitted by the thinner filters. The spots act as an anti-reflection coating in the visible wavelengths thus increasing the G-band signal in spots. Attempts to create an effective wavelength dependent flat field to correct for the effect of the contamination spots has so far proven unsuccessful, though a cosmetic correction can be performed. Software to perform the cosmetic correction exists in SSW, and one method will be included as an option in the latest update to `xrt_prep.pro`, however, we stress this is not a scientific calibration of the spots. The use of pixels affected by contamination spots is strongly discouraged.

Dust specks were noted before launch and essentially block most incoming radiation. Hot pixels are defined as persistently over-bright pixels seen in averaged dark frames; the resulting maps are a combined result of independent analysis by R. Kano and coauthor Saar. These pixels are flagged as a precaution; it is not clear that they are significantly degraded in their calibration relative to "normal" pixels.

Additional Systematic Effects Outside of the Scope of the `xrt_prep.pro`

Some effects on the instrument are more difficult to correct. Many are model dependent, and thus beyond our ability to correct/estimate with confidence. Cosmic ray streaks are not corrected by `xrt_prep.pro`, as the most effective repair is cosmetic, and thus not scientifically robust (though the cosmetic repair is optionally available within `xrt_prep.pro`).

The grazing incidence mirror used by XRT is a source of scattered light. This scattered light requires a model dependent and non-trivial deconvolution to correct, and is thus not performed by `xrt_prep.pro`. Estimates of the uncertainties due to scattered light are similarly difficult to estimate, and as such are not considered.

We have chosen not to estimate the uncertainties from photon counting in `xrt_prep.pro`, as they rely heavily on models of the emitting plasma, as shown in Section A.5. Modeling the photon counting uncertainty requires knowledge of the temperature and density of the emitting plasma, which can then be used to estimate the number of electrons each photon will excite in the CCD, which is strongly wavelength dependent. It is non-trivial to estimate the differential emission measure of solar plasma with broadband imager data. The interested user can estimate these uncertainties using software already in SSW, in particular `xrt_cvfact.pro`.

In May of 2012, a calibration shift was detected, believed to have been caused by a small breach in the entrance filter on the outer annulus of the telescope. The fissure in this filter allows extra visible light to fall onto the detector at the back of the telescope. While the full extent of this shift is still under investigation, it has been determined that the calibrations discussed here are not affected by the shift. The correction for this effect is still under development and will be detailed in a later paper after a more complete analysis can be performed.

Due to the normal and expected degradation over its lifetime, the CCD is beginning (as of late 2012) to exhibit signs of charge transfer inefficiency (CTI). CTI is caused by the CCD not fully transferring accumulated charge from one pixel to the next during readout, which creates a faint smeared trail in vertically adjacent pixels. This is a common problem in similar devices and tends to increase during the life of the CCD Janesick (2001). In the case of XRT, the CTI is noticeable in a few pixels in low-signal areas, with a magnitude that is of the same order as the dark noise (a few DN/pixel). In general CTI can be remedied by an annealing process whereby the CCD is exposed to heat, though the onboard heaters for XRT are unable to heat the CCD to high enough temperatures to noticeably improve charge transfer efficiency. At the time of this writing, no reliable quantitative correction procedure for CTI effects has been established.

Uncertainties

A.6. Combining the Systematic Uncertainties

A preliminary version of the discussion of combining and comparing the systematic uncertainties can be found in Kobelski et al. (2012), and we include an updated presentation here which includes more accurate estimates of the Fourier filter uncertainties (as discussed in Section A.5). Due to the multiplicative factor of vignetting, the systematic uncertainties (dark, Nyquist, Fourier, vignetting, and JPEG) do not add in simple quadrature. The dark, Fourier filtering and JPEG uncertainties do add simply, yielding

$$\sigma^2_{\mathrm{DFJ}} = \sigma^2_{\mathrm{dark}} + \sigma^2_{\mathrm{FF}} + \sigma^2_{\mathrm{JPEG}}. \tag{5.16}$$

Since the vignetting correction is a divisor to the image, we must add the uncertainty due to vignetting as a relative uncertainty, and thus

$$\Big(\frac{\sigma_{\mathrm{final}}}{I_{\mathrm{final}}}\Big)^2 = \Big(\frac{\sigma_{\mathrm{DFJ}}}{I_{\mathrm{DFJ}}}\Big)^2 + \sigma^2_{\mathrm{V}}, \tag{5.17}$$

where the I_{final} is the fully corrected image, and I_{DFJ} is the dark corrected image and σ_{V} is the vignetting uncertainty from Equation (5.15). A comparison between these individual uncertainties is shown in Figure 29. In all data sets we tested where the compression was $Q95$ or stronger, the JPEG uncertainty was the dominant source of systematic uncertainty, though still dwarfed by reasonable estimates of the photon counting uncertainty. It can also be noted that the uncertainties introduced by the calibration shift will add in quadrature into Equation (5.16).

A.7. Photon Counting Uncertainties

To determine the uncertainties from photon counting, we must attempt to translate the digitized DN value from the detector into the number of photons incident on the detector. This is a difficult (if not ill posed) inversion problem. The difficulties arise partially from the fact that the quantum efficiency and gain of the detector are wavelength dependent, such that the number of electrons produced from a single incident photon varies depending on the wavelength of the photon. With a broadband instrument such as XRT, we thus must estimate the temperature of the emitting plasma to determine the number of incident photons for a given DN. The photon counting uncertainty is temperature dependent and is thus not well known, especially when considering multi-thermal plasmas. An example of this temperature dependence can be seen in Figure 30. As previously mentioned, due to this model dependence, we have not included photon counting uncertainties with the systematic uncertainties that are included in `xrt_prep.pro`.

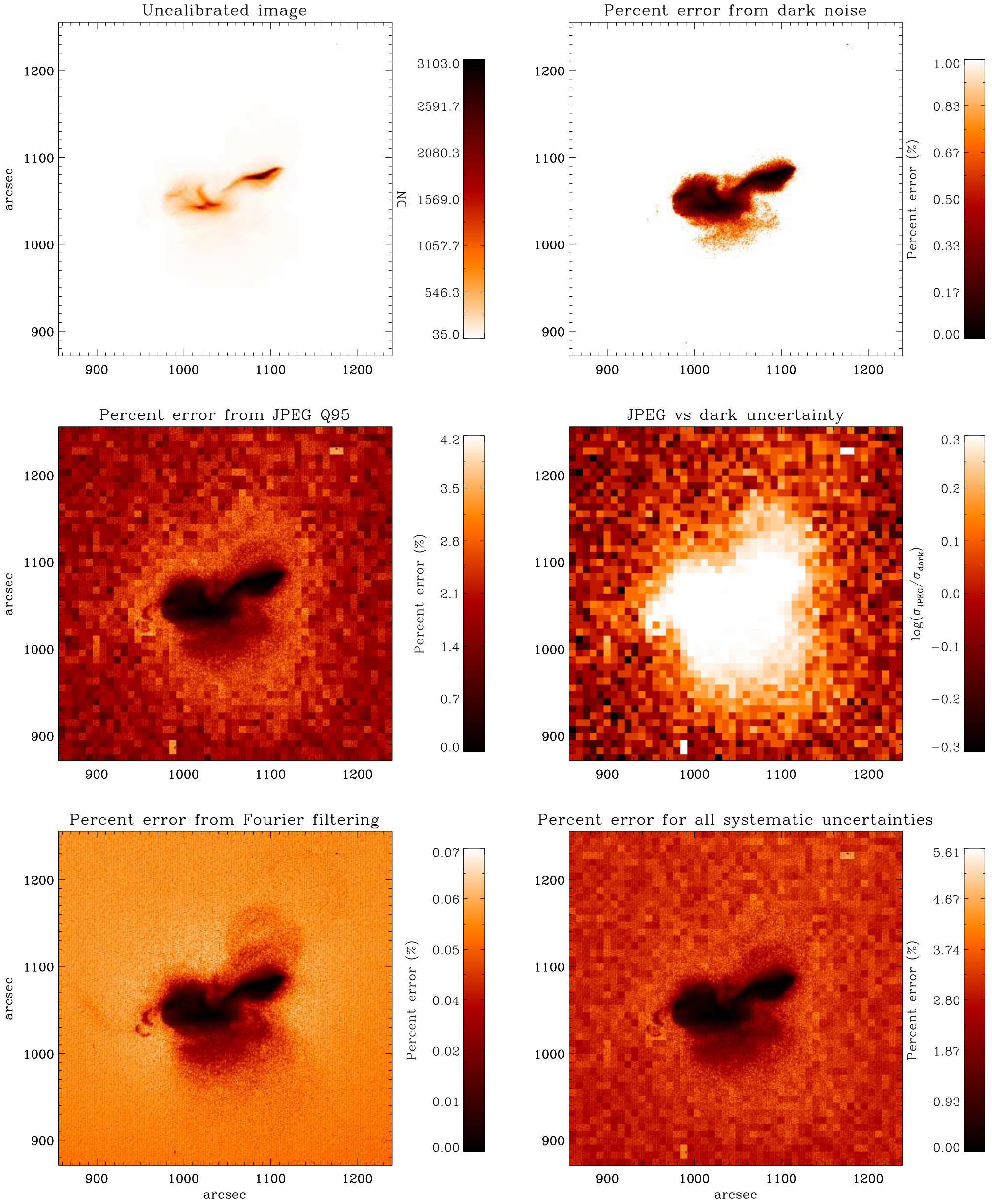

Figure 29: A comparison of the different systematic/non-statistical uncertainties from a randomly selected but typical image. Note the varying scales. The JPEG generally dominates the uncertainty when using $Q95$ compression. The upper left is the reverse color raw image. The upper right shows the percent error within the dark noise, which scales inversely with total signal (0–1.0%). The middle left shows the JPEG compression uncertainty for the same image (0–4.2%).Very few pixels have 4% uncertainties, most are much lower. The middle right is the *logarithm* of the ratio of JPEG uncertainty to Dark Uncertainty.The JPEG uncertainty is almost always larger than the dark uncertainty. The lower left is the percent error from the Fourier filtering, which is very small while still reducing the dark uncertainty. All of these plots are normalized by $I_{\mathrm{final}}/I_{\mathrm{DFJ}}$ as given by Equation (5.17). The vignetting uncertainty is not shown, as it is 0.45% across the whole field of view as given by Equation (5.15). The total systematic uncertainty is in the lower right.

A.8. Comparing the Uncertainties

We have measured the uncertainties including photon noise for multiple data sets so as to compare the magnitudes. Typical comparisons are shown in Figure 30. The temperatures chosen in Figure 30 ($10^{5.5}$ K and $10^{6.9}$ K) illustrate the variation in photon counting noise across the temperature range of XRT. The dominance of photon noise over the systematic uncertainties is clearly evident. The photon counting noise was calculated using the expected instrumental response to a plasma of a given temperature, as discussed in Narukage *et al.* (Narukage et al., 2011). The success of the calibration can be seen by how small the systematic uncertainties are when compared to the photon counting noise.

The regions of high JPEG uncertainty are generally in the low DN range, where the photon noise is also very great. As the assumed temperature is increased, the dominance of the photon noise becomes even more significant, becoming nearly 30 times larger than the systematic uncertainties. While the photon noise can be limited operationally (*e.g.* via deeper exposures and pixel binning), the photon counting uncertainty will always dominate the systematic uncertainties. It is also worth noting the small effect of JPEG compression when compared to the omnipresent photon counting noise. All of these factors suggest that while the JPEG compression uncertainty is non-negligible, it is quantifiable and does not significantly impair the data when compared to other factors.

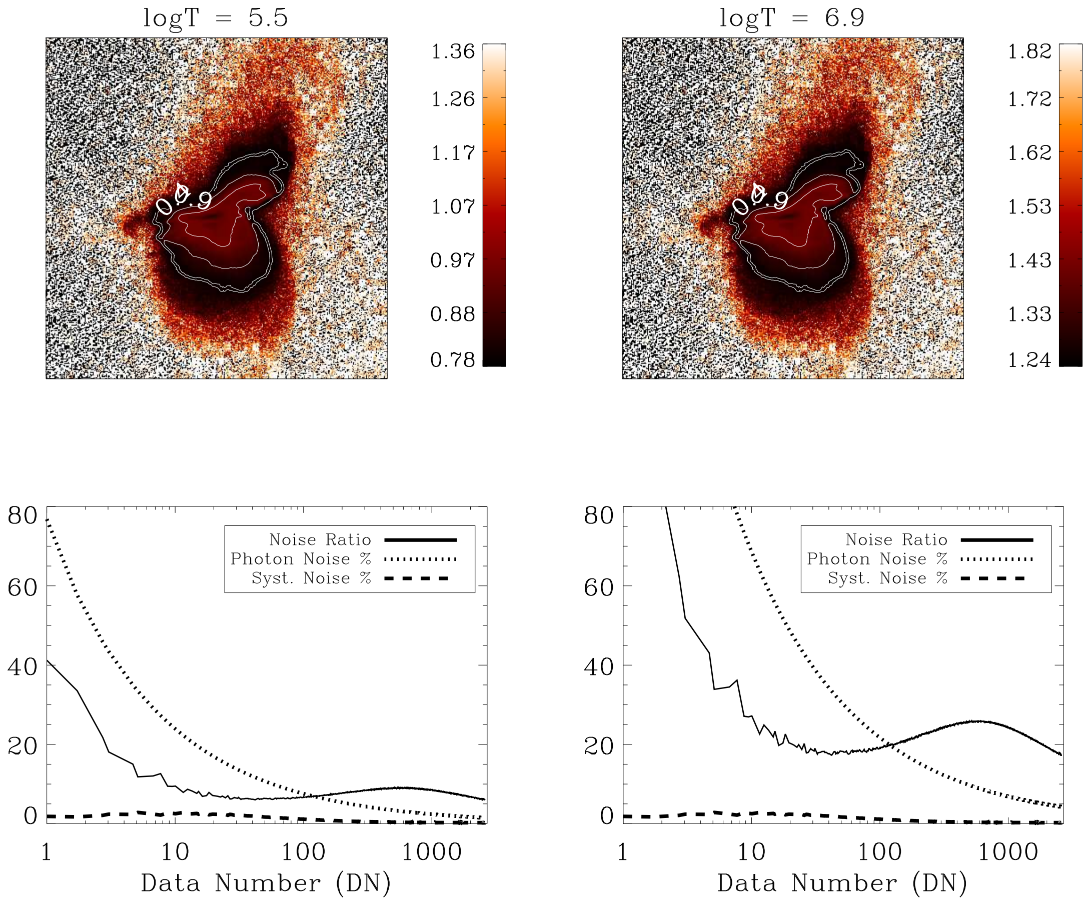

Figure 30: The top images are 512×512 pixel maps of the logarithm of the ratio of photon noise to systematic (non-statistical) noise for Ti_poly observations from January 2011 with contours illustrating the systematic uncertainty percent error. We assumed a $\log T$ of 5.5 for the left plot, and 6.9 for the right. The contours give reference values, where the ratio is 0.4 and 0.9. The bottom plot shows the ratio of photon noise to systematic noise as a function of signal for each assumed temperature, and also plots the percent uncertainty for both sources for the image set used above. The dotted line is the photon noise, while the lower dashed line is the systematic noise. In addition to showing the dominance of the photon counting noise compared to systematic uncertainty, these plots also illustrate the strong effect the assumed temperature has on the photon counting uncertainty. This plot is adapted and updated from a similar plot found in Kobelski *et al.* (2012).

Test Case

To illustrate the utility and capabilities of `xrt_prep.pro`, we demonstrate a sample analysis of XRT observations taken 15 February 2001 of active region AR 11158. This data set was chosen for having a large dynamic range in the observations as well as a fairly standard level of JPEG compression ($Q95$). The active region produced a few flares, including a GOES X-class flare at 01:56UT. Figure 31 shows an unprepped image and a comparison image to illustrate the effects of the calibration. The prepped image has an improved contrast across the image, especially in the eastern section of the active region. The roughness in the quiet sun regions of the percent change plot comes about from the prep process removing the high frequency noise in this region, thus smoothing the background levels.

As can be seen in the right panel of Figure 31, the correction from the calibration is stronger in the quiet sun regions where there is inherently a smaller signal compared to noise. Where more flux is detected, the difference between the prepped and unprepped data becomes smaller, though it is still significant.

Figure 32 illustrates the effects of the calibration process. The top light curve is the unprepped raw and calibrated data from the boxed region in Figure 31. For most of the data, the prep process determines that approximately 40% of the signal is extraneous, as shown in the bottom panel of Figure 32. Deviations from the average value illustrate the dynamics of the calibration, with which small brightenings become more prominent, as seen when comparing to the upper two light curves. The

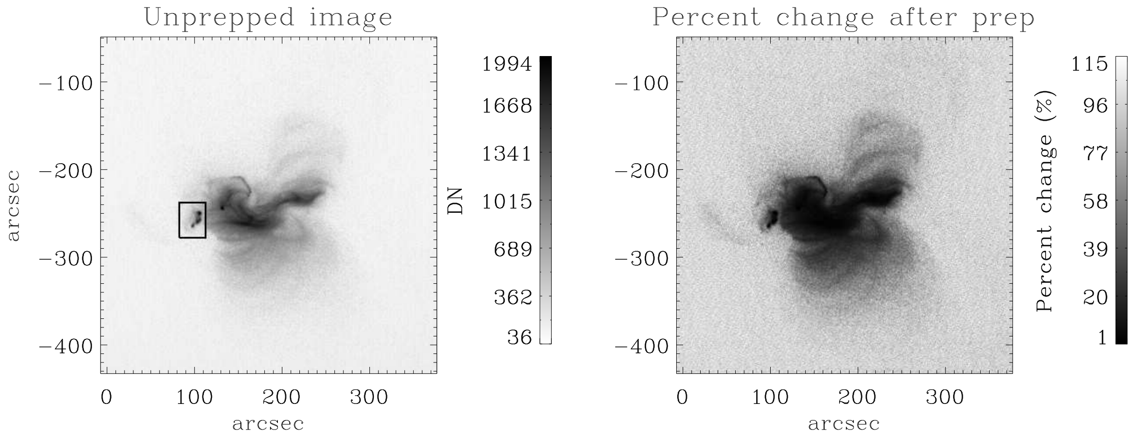

Figure 31: Reverse color Ti_poly image of AR 11158. On the left is the image before processing through `xrt_prep.pro`, and on the right is the percent change of the same image after the prep process. The percent change is the difference between the unprepped and prepped image, normalized by the unprepped image. The always positive result shows that the raw image always contains more DN/pixel than the prepped image, as extraneous signal is removed by the prep process. The processing improves the perceived contrast of the active region, and removes noise in the low signal regions. The box in the unprepped image marks the area integrated for the light curves plotted in Figure 32.

brightenings around 2UT strongly illustrate this effect and show that the difference in the upper and middle plots is from more than just exposure time normalization when compared to the lower plot. Additionally, the ability to estimate systematic uncertainties enables meaningful photometric measurements, particular important for distinguishing small brightenings from random fluctuations of X-ray intensity.

Conclusion

The current empirical calibration of XRT data provided by `xrt_prep.pro` is robust and greatly improves the reliability and accuracy of the data. Estimates of systematic uncertainties are provided by `xrt_prep.pro` to assist users in quantitative photometry

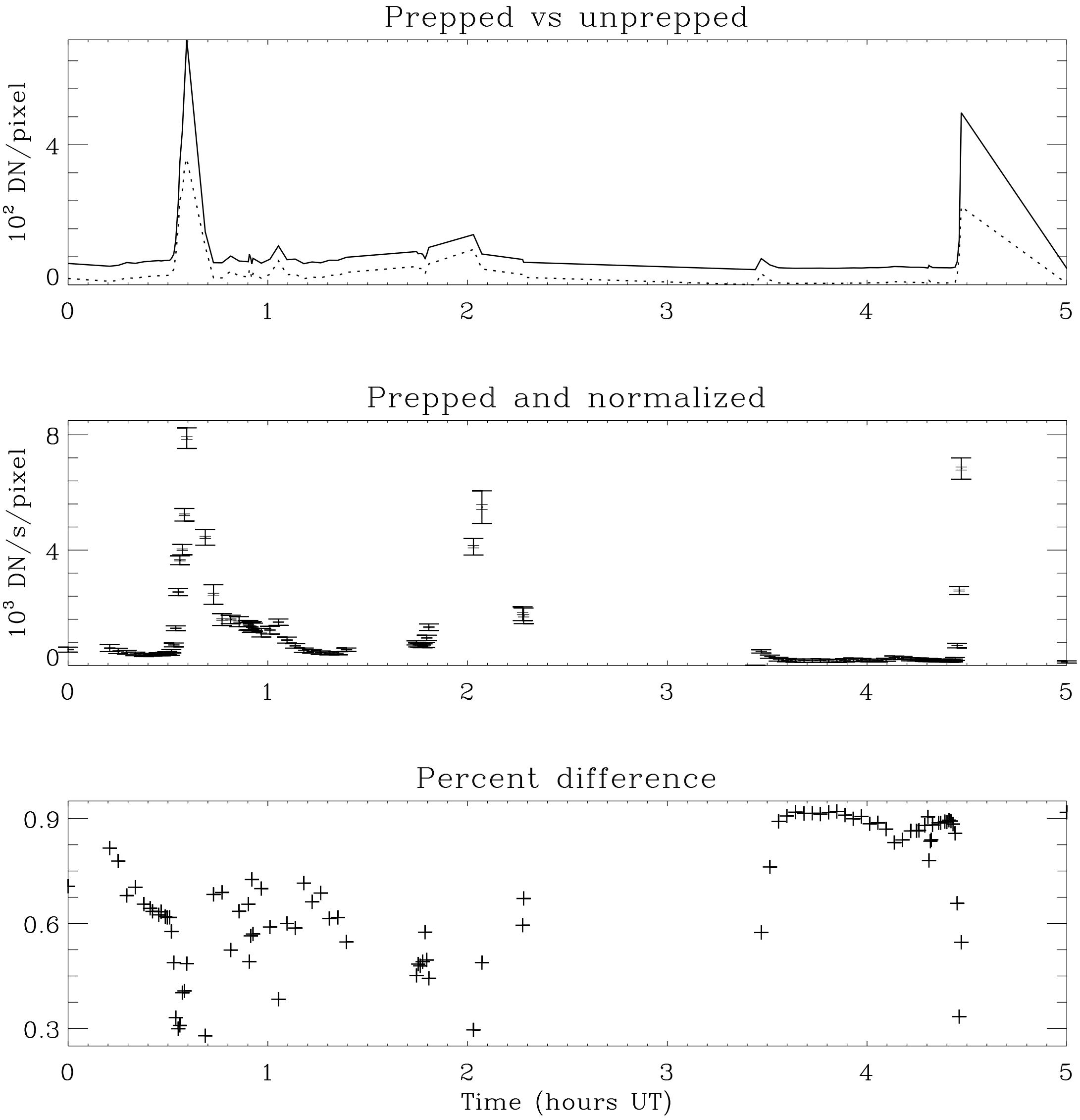

Figure 32: Light curve of the boxed region in Figure 31. The top light curve is the raw uncalibrated (solid line) and the calibrated data (dotted line), normalized by the number of pixels in the region. The second plot is the data after having been run through `xrt_prep.pro`, and normalized by exposure time. The more narrow error bars are the calculated systematic uncertainty, the bigger and wider error bars are the photon counting uncertainty. The final plot is the difference between the raw data and the prepped data, normalized by the raw data. The strong deviations from a flat line show the dynamics of the subtraction, *i.e.* more than just a spatially flat dark image was removed. Note that exposure time and pixel normalization does not matter for the lower plot, all of the normalization factors will cancel out.

of coronal features with XRT. In all cases the systematic uncertainties are found to be smaller than the (model dependent) photon counting uncertainties. The authors and the XRT Team recommend that any radiometric analysis of these data should include the corrections described in this paper and as performed by `xrt_prep.pro`. This analysis can also serve as a starting point for a more thorough correction of the data for the inclined and motivated user. Most of the methods used here are not limited to the analysis of X-ray data, and are thus viable ways to empirically calibrate data sets from other missions.

Acknowledgements

Hinode is a Japanese mission developed and launched by ISAS/JAXA, collaborating with NAOJ as a domestic partner, and with NASA and STFC (UK) as international partners. Scientific operation of the *Hinode* mission is conducted by the *Hinode* science team organized at ISAS/JAXA. This team mainly consists of scientists from institutes in the partner countries. Support for the post-launch operation is provided by JAXA and NAOJ (Japan), STFC (U.K.), NASA, ESA, and NSC (Norway). This work was supported by NASA under contract NNM07AB07C with the Smithsonian Astrophysical Observatory.

APPENDIX B

EXTRA FIGURES OF FLUX FROM MODEL FITS TO XRT DATA NOT INCLUDED IN CHAPTER 2

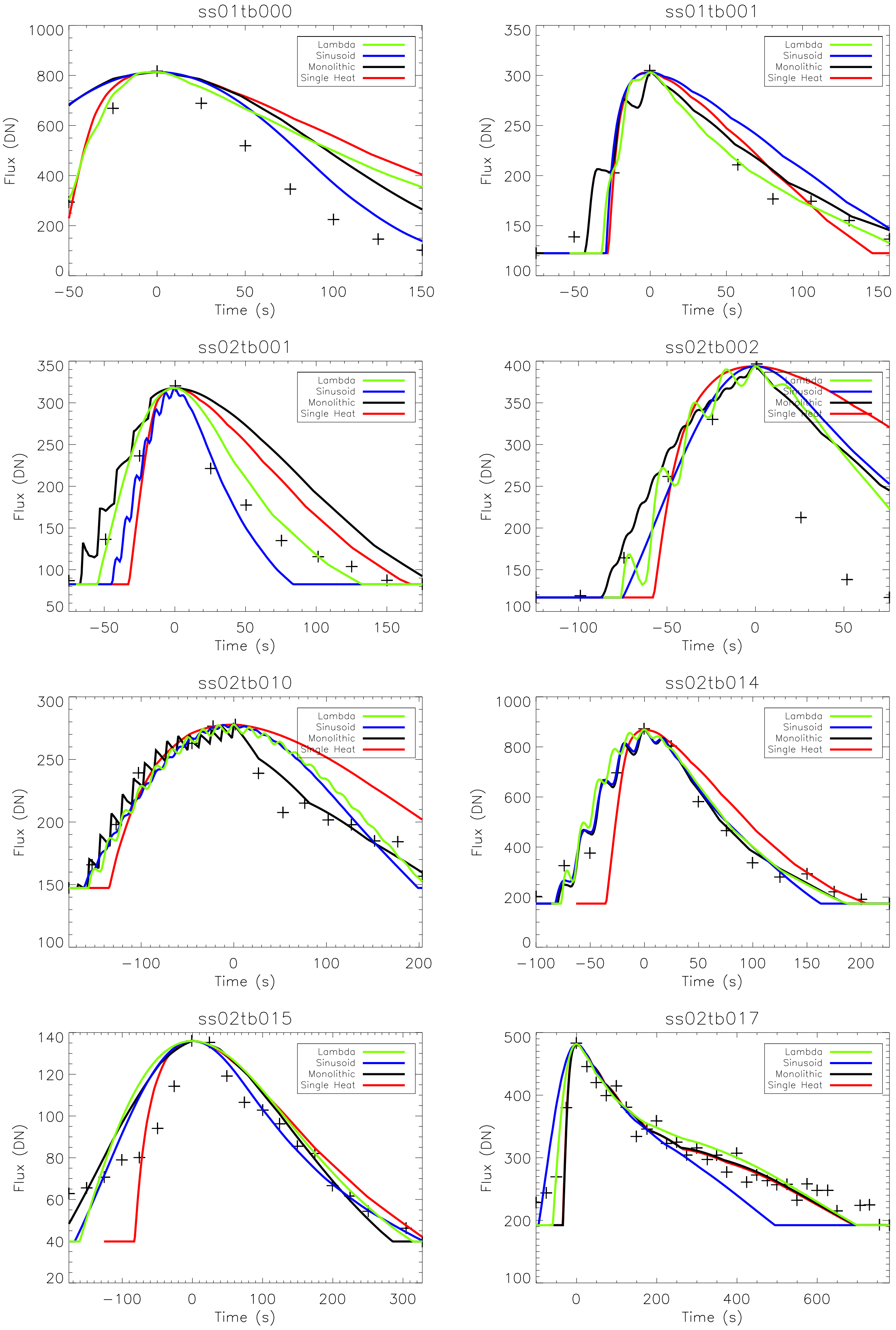

Figure 33: Figures of fits of the model to the data not shown in Chapter 2.

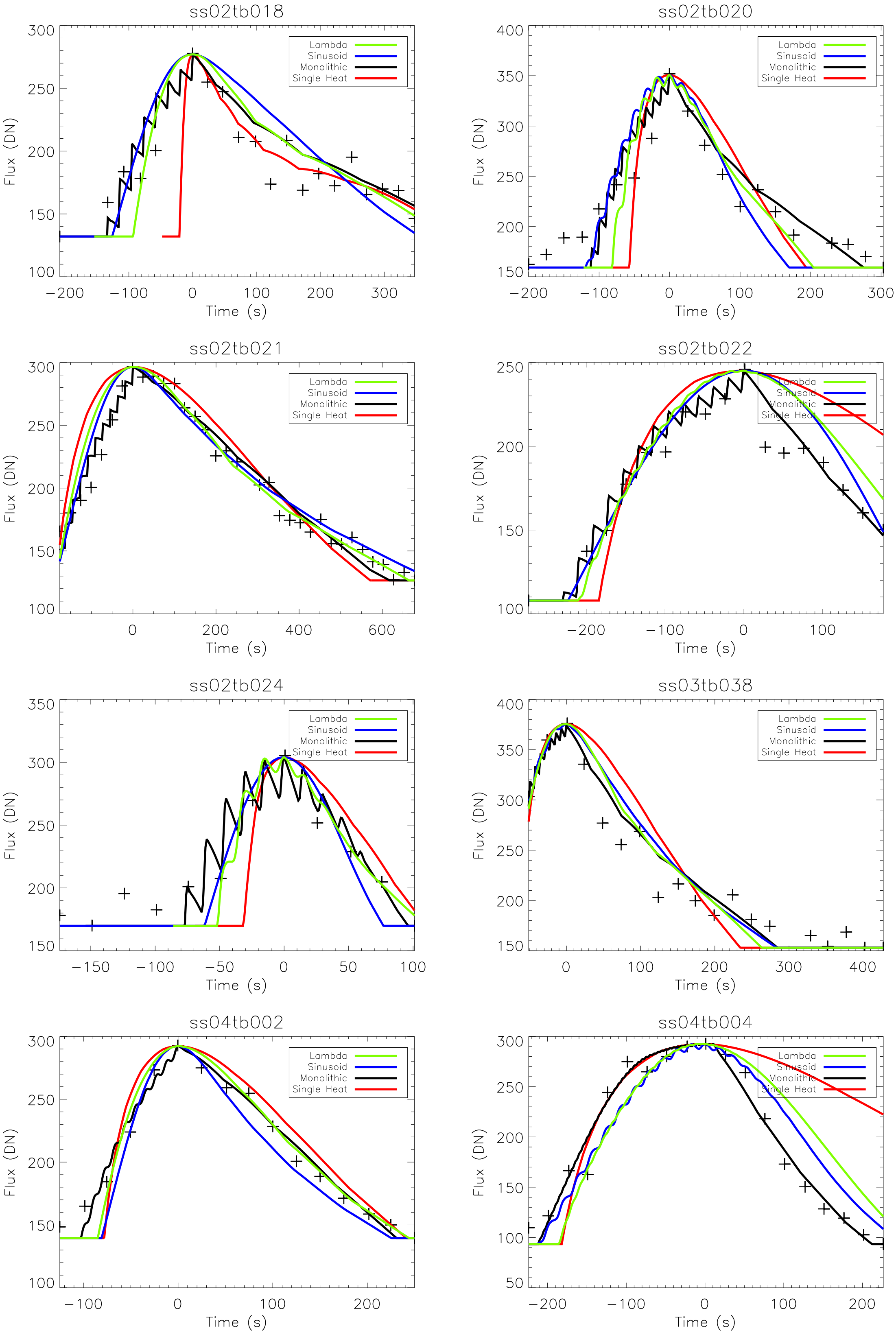

Figure 34: Figures of fits of the model to the data not shown in Chapter 2.

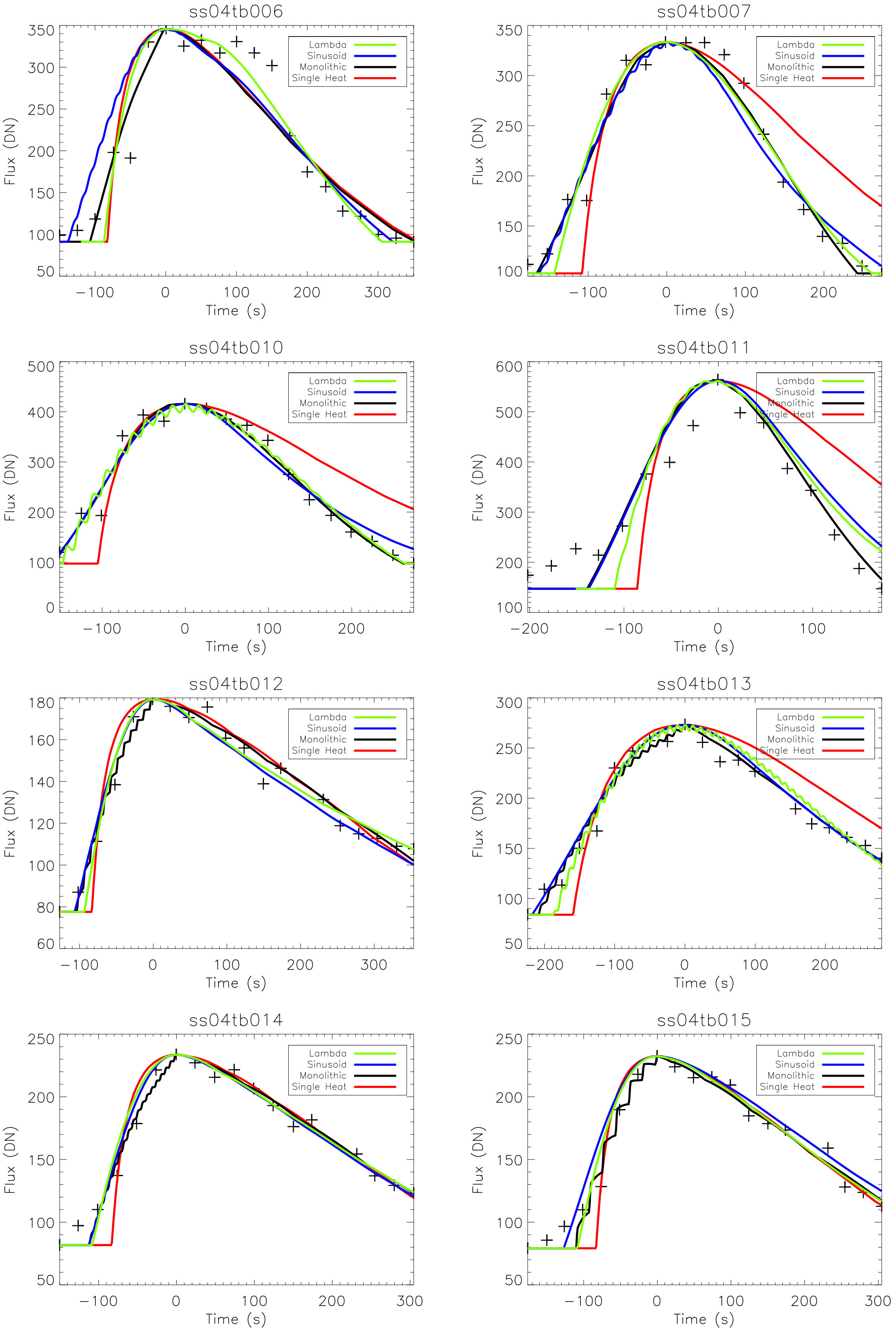

Figure 35: Figures of fits of the model to the data not shown in Chapter 2.

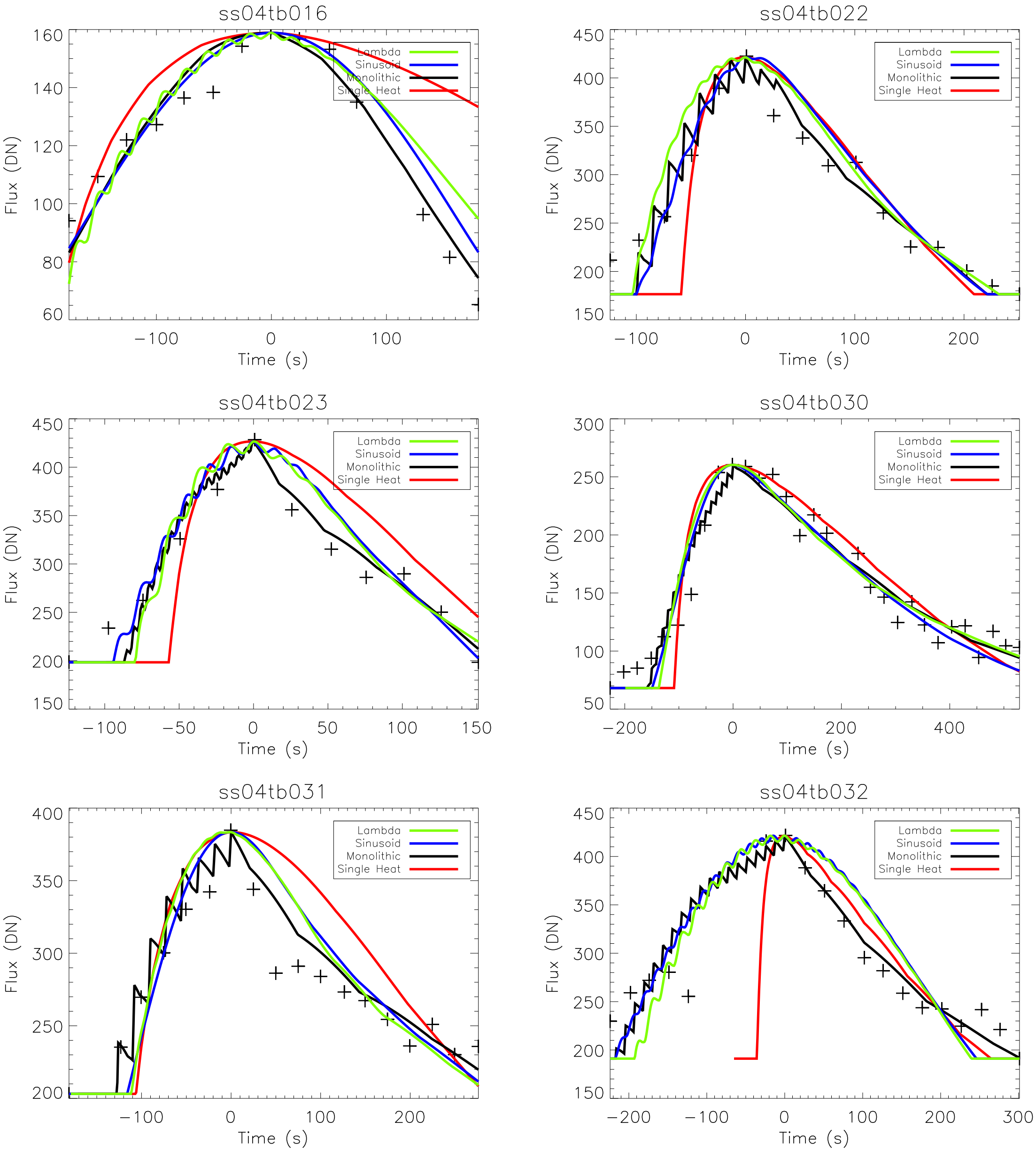

Figure 36: Figures of fits of the model to the data not shown in Chapter 2.

APPENDIX C

EXTRA FIGURES OF FLUX, TEMPERATURES, AND DENSITIES OF MODEL FITS TO HI-C DATA NOT INCLUDED IN CHAPTER 3

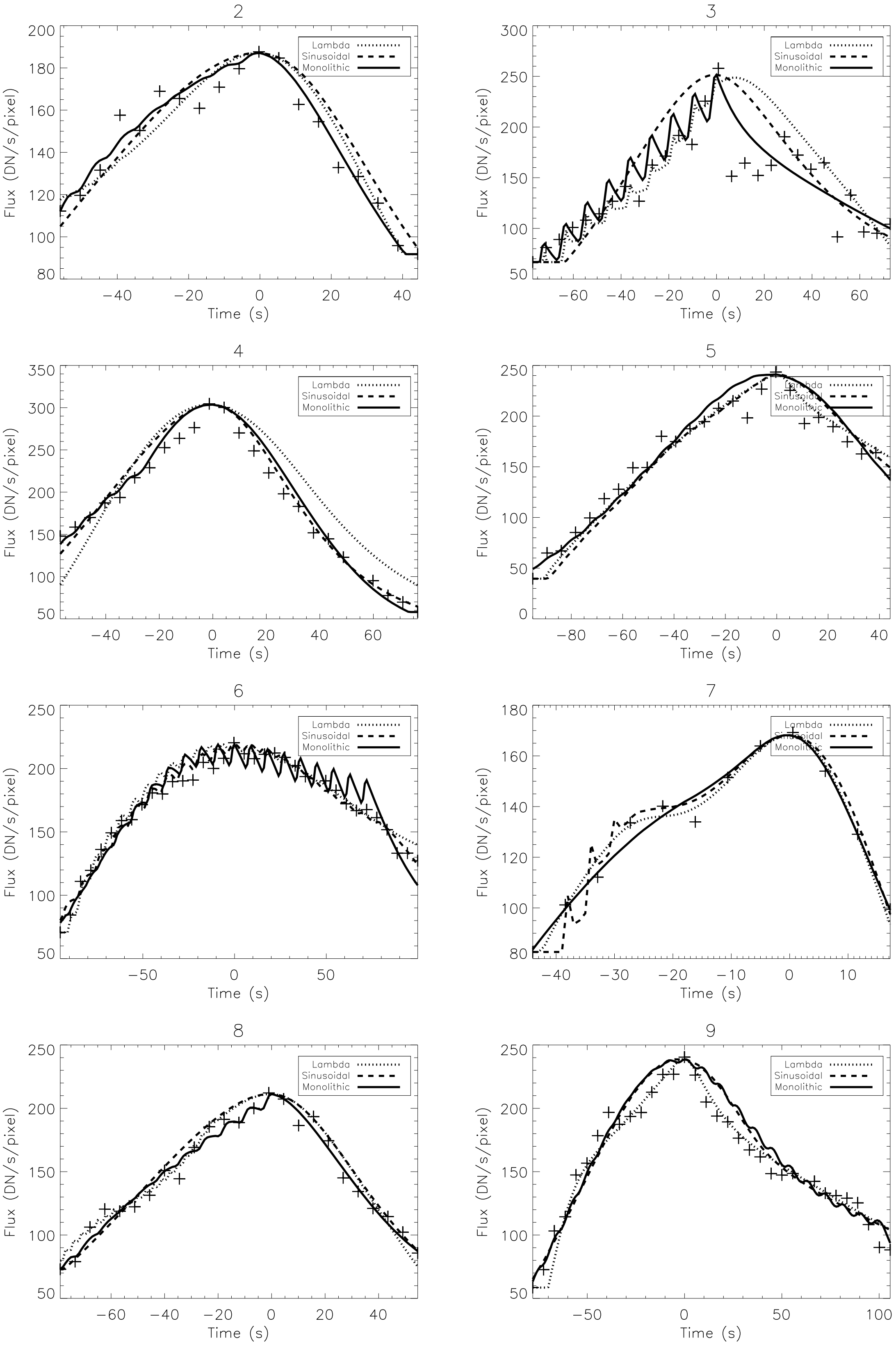

Figure 37: Figures of fits of the model to the data not shown in Chapter 3. Numbers 2-9 in Table 7. The dotted line is the fit from the lambda envelope, the dashed for the sinusoidal envelope and black for the monolithic envelope. The observational flux is denoted with (+)s.

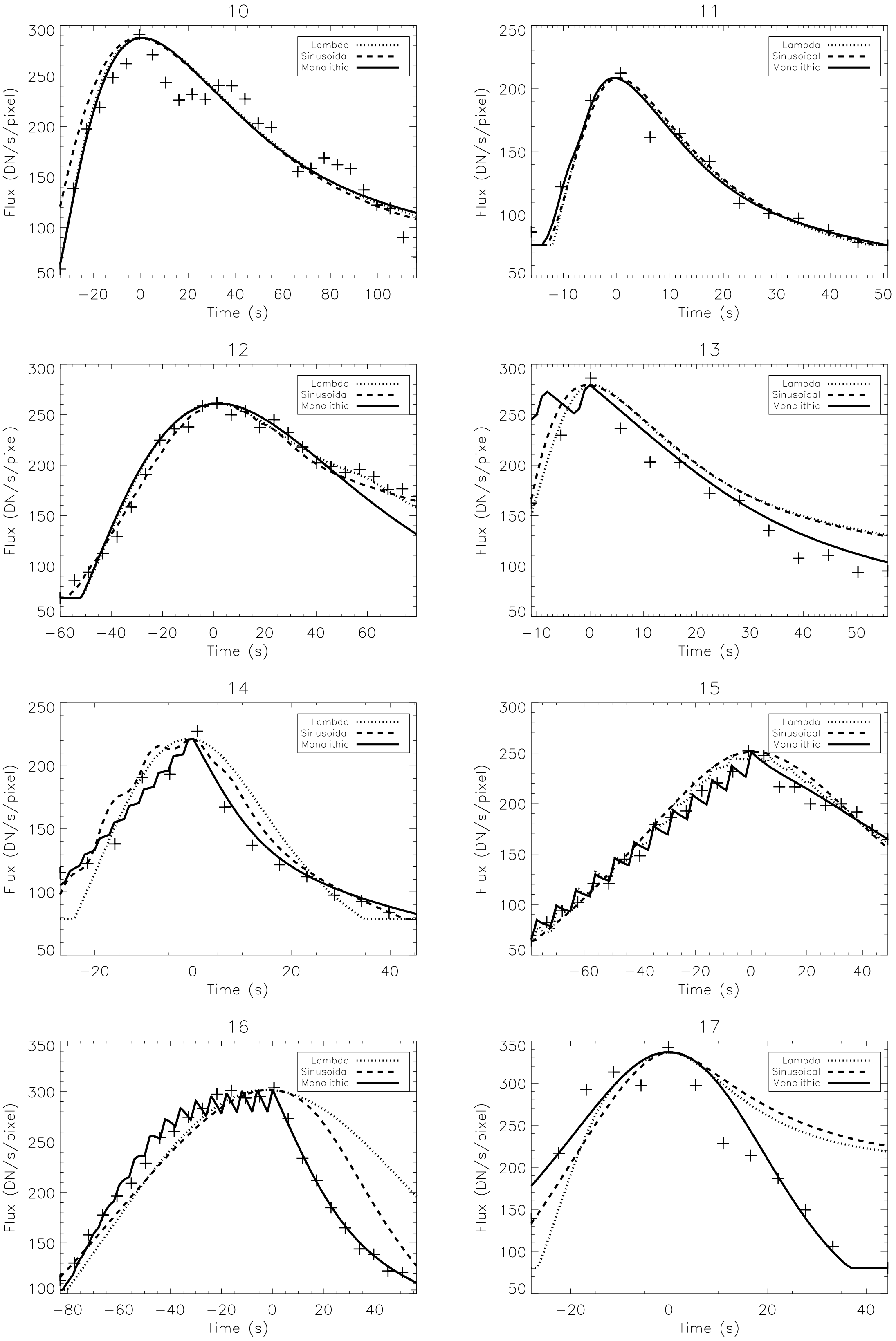

Figure 38: Figures of fits of the model to the data not shown in Chapter 3. Numbers 10-17 in Table 7. The dotted line is the fit from the lambda envelope, the dashed for the sinusoidal envelope and black for the monolithic envelope. The observational flux is denoted with (+)s.

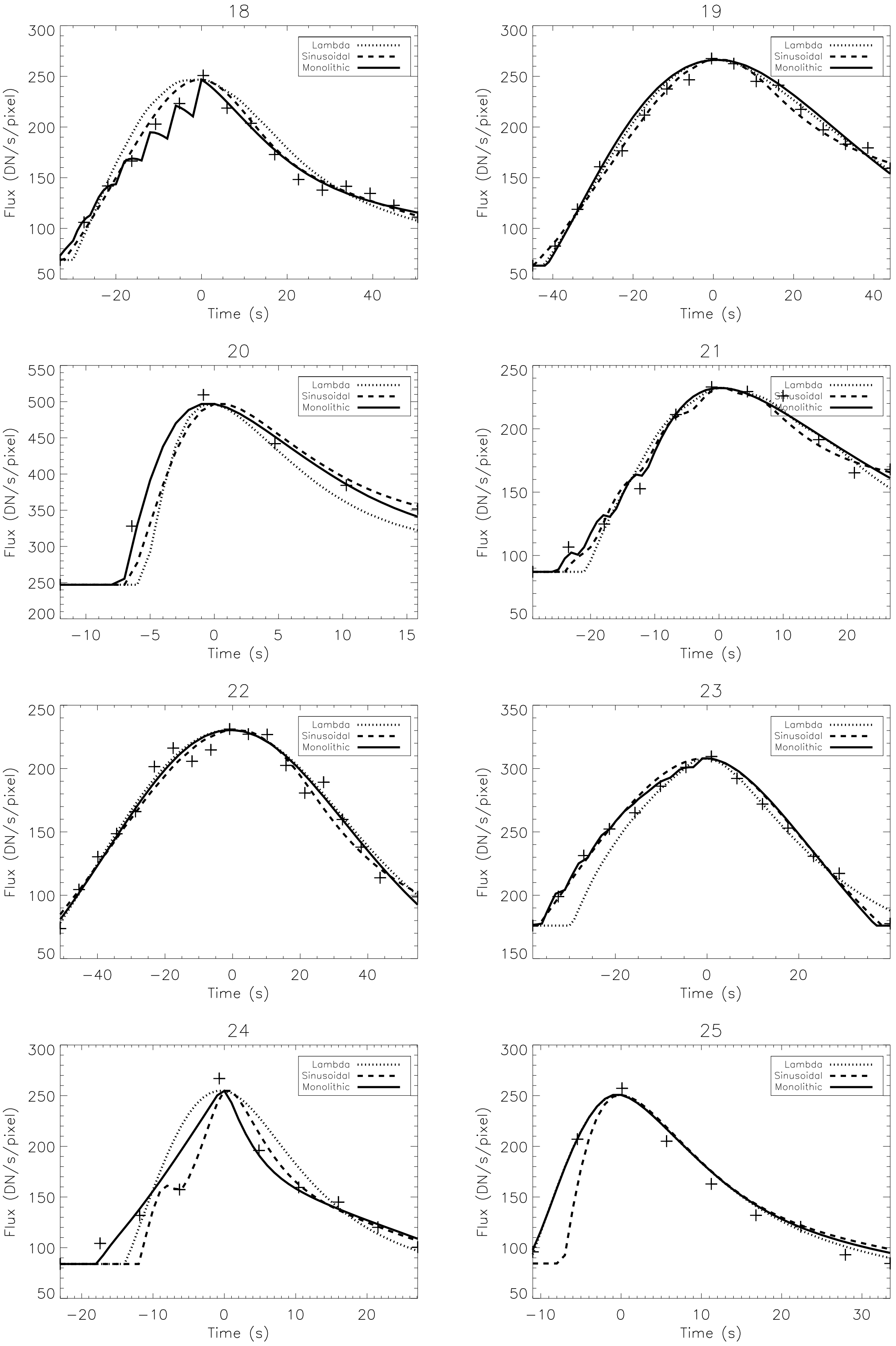

Figure 39: Figures of fits of the model to the data not shown in Chapter 3. Numbers 18-25 in Table 7. The dotted line is the fit from the lambda envelope, the dashed for the sinusoidal envelope and black for the monolithic envelope. The observational flux is denoted with (+)s.

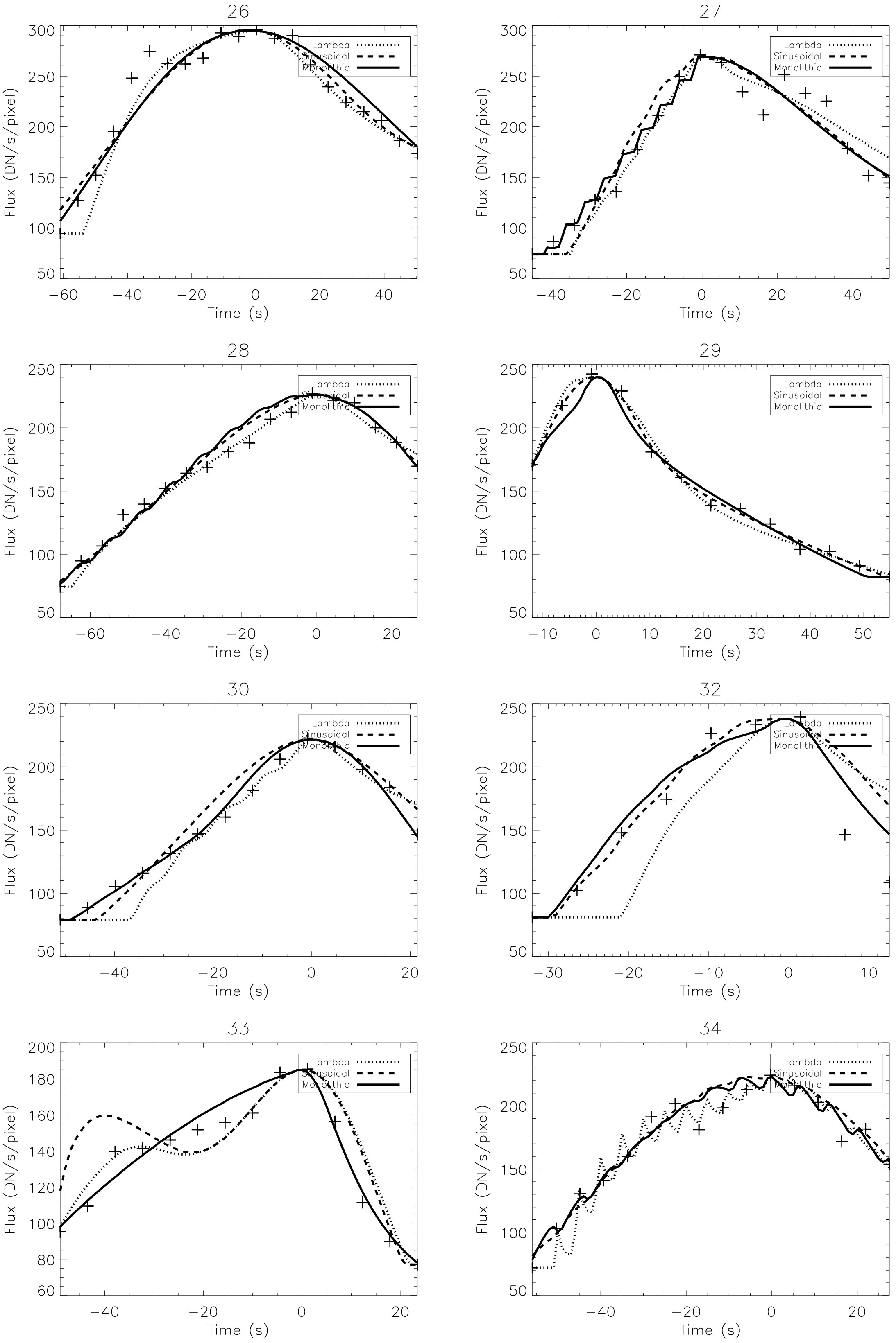

Figure 40: Figures of fits of the model to the data not shown in Chapter 3. Numbers 26-30 and 32-34 in Table 7. The dotted line is the fit from the lambda envelope, the dashed for the sinusoidal envelope and black for the monolithic envelope. The observational flux is denoted with (+)s.

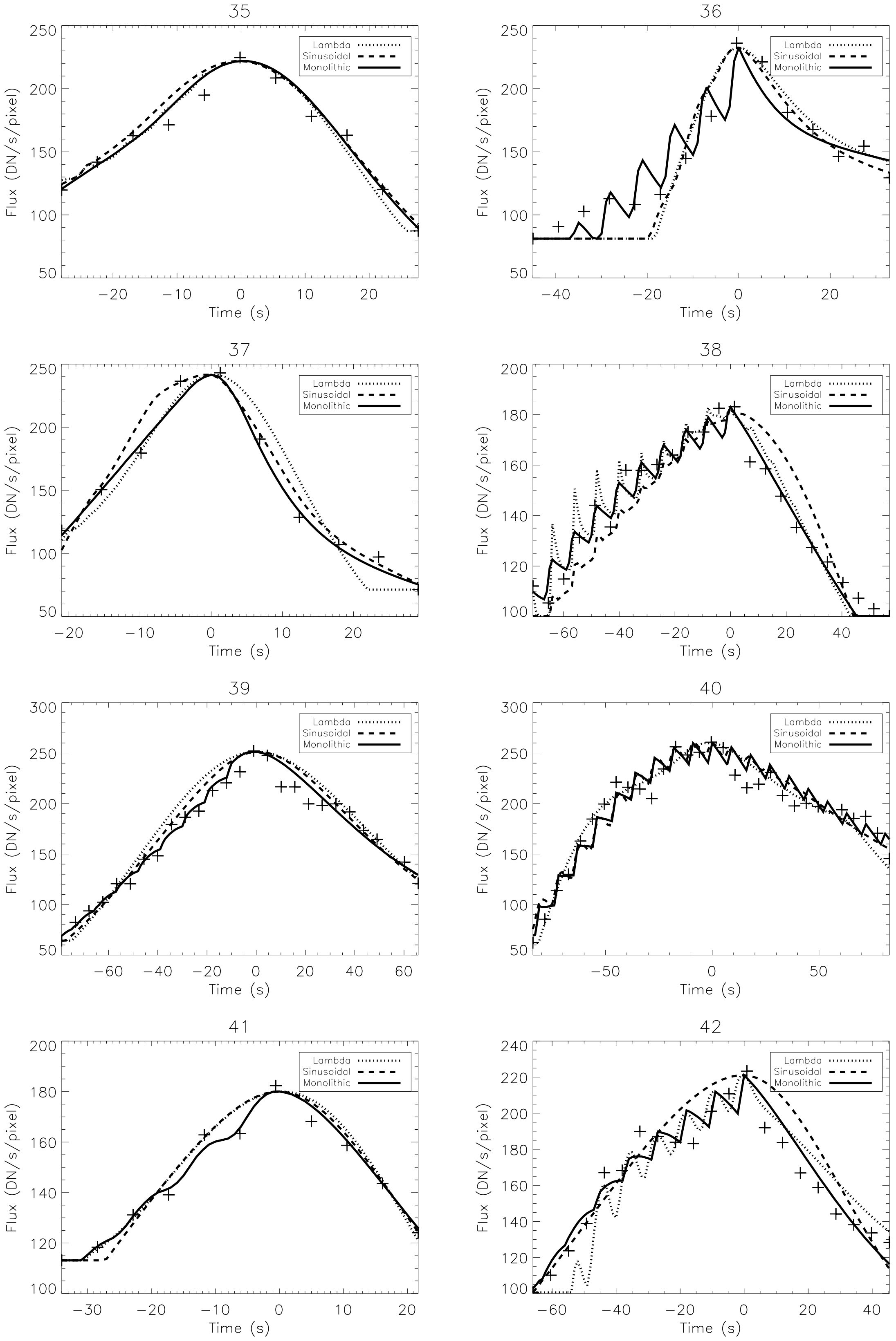

Figure 41: Figures of fits of the model to the data not shown in Chapter 3. Numbers 35-42 in Table 7. The dotted line is the fit from the lambda envelope, the dashed for the sinusoidal envelope and black for the monolithic envelope. The observational flux is denoted with (+)s.

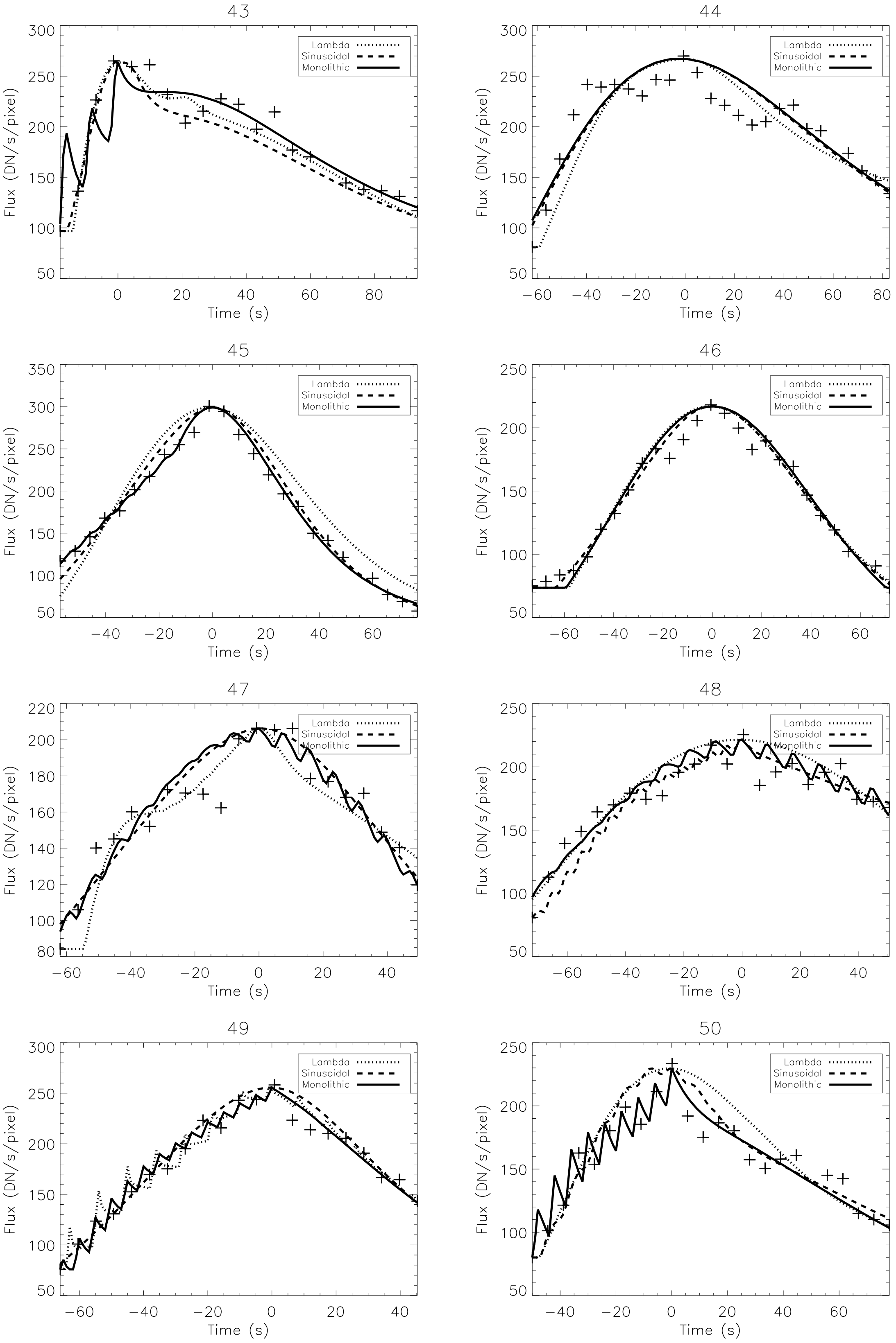

Figure 42: Figures of fits of the model to the data not shown in Chapter 3. Numbers 43-50 in Table 7. The dotted line is the fit from the lambda envelope, the dashed for the sinusoidal envelope and black for the monolithic envelope. The observational flux is denoted with (+)s.

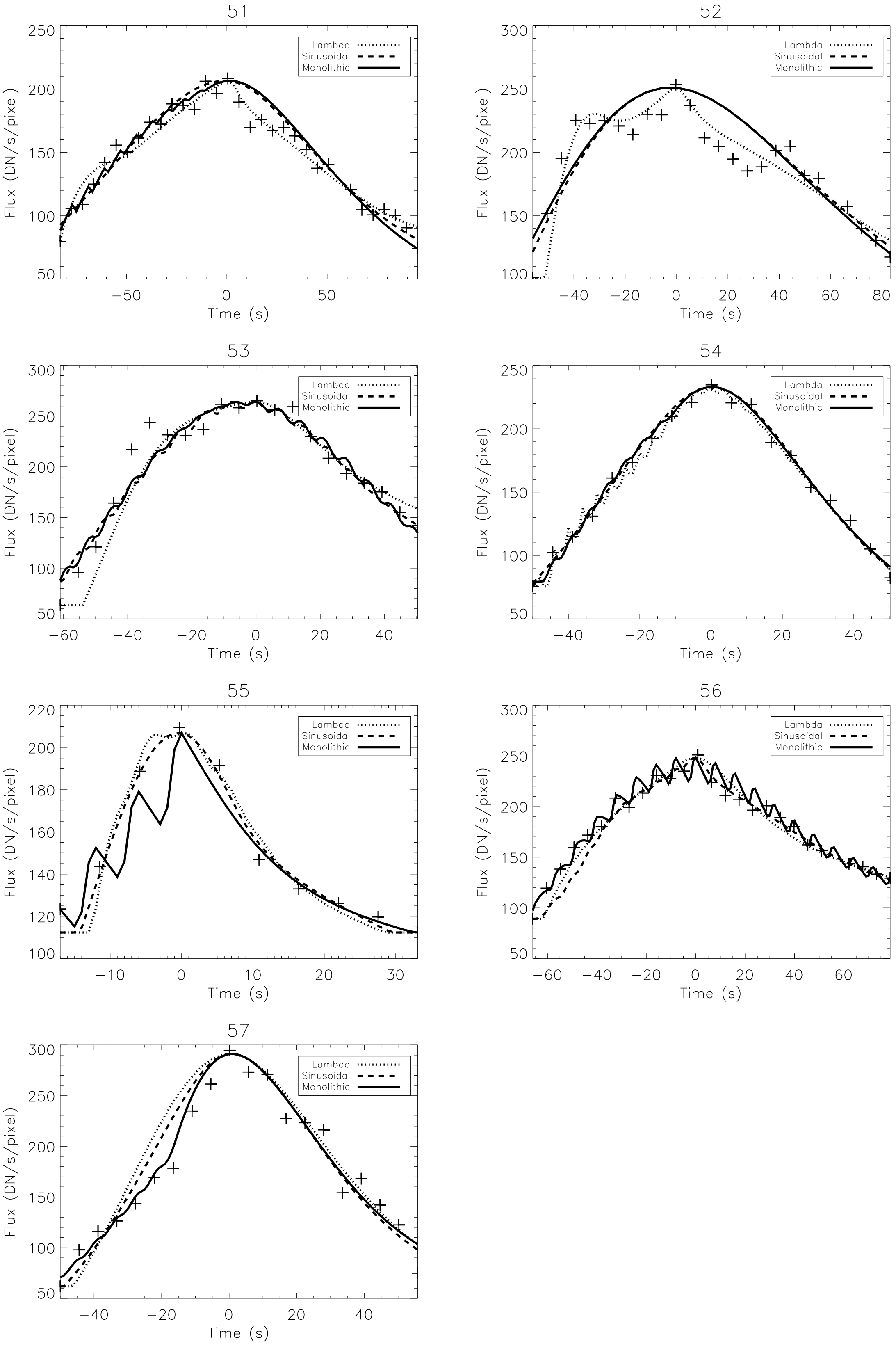

Figure 43: Figures of fits of the model to the data not shown in Chapter 3 Numbers 51-57 in Table 7. The dotted line is the fit from the lambda envelope, the dashed for the sinusoidal envelope and black for the monolithic envelope. The observational flux is denoted with (+)s.

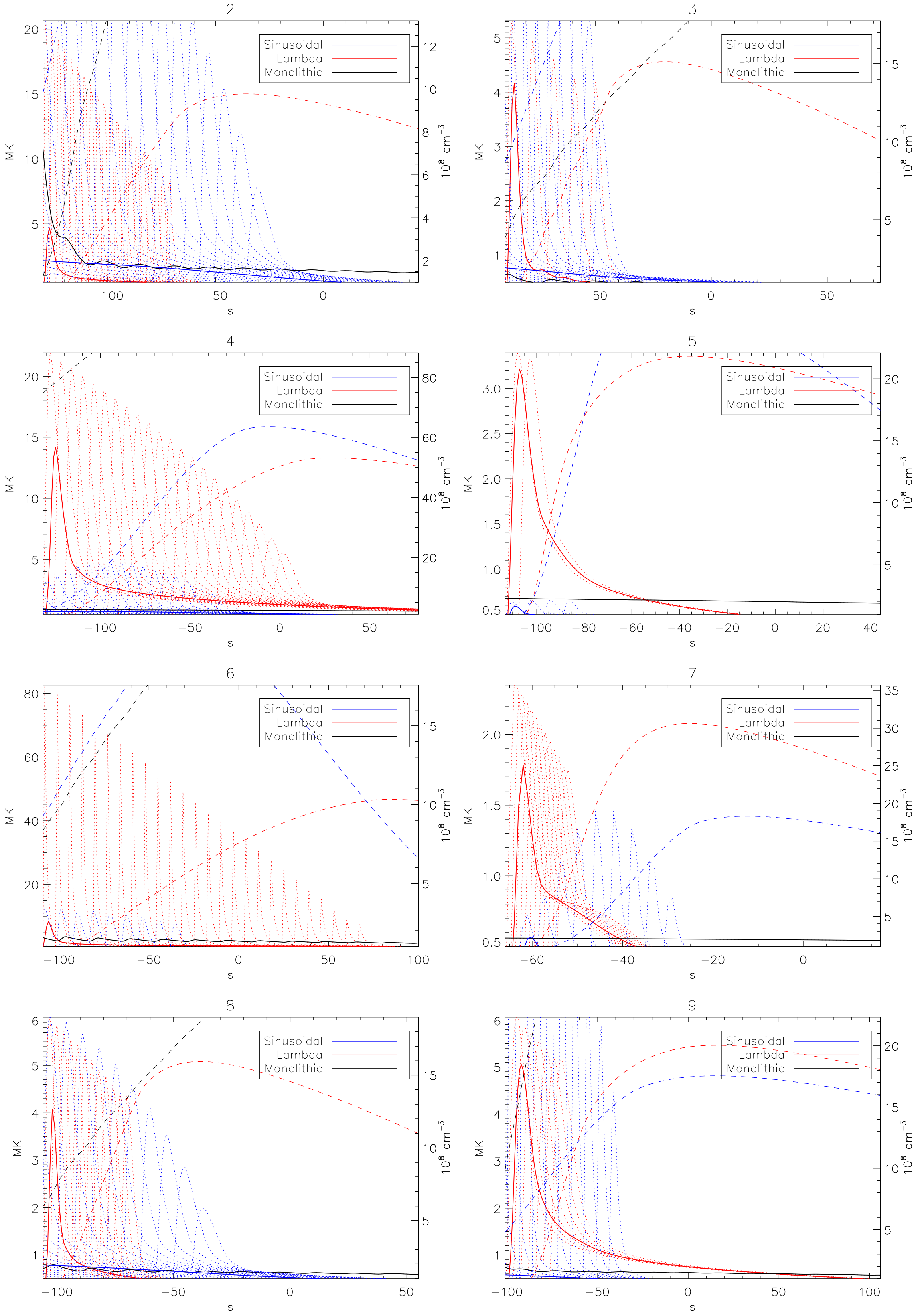

Figure 44: Figures of temperatures and densities used by the model to fit the data not shown in Chapter 3. Numbers 2-9 in Table 7. The dotted lines represent the temperatures of the individual strands, the solid lines are the emission measure weighted temperature. The dashed lines represent the average densities of the ARTB.

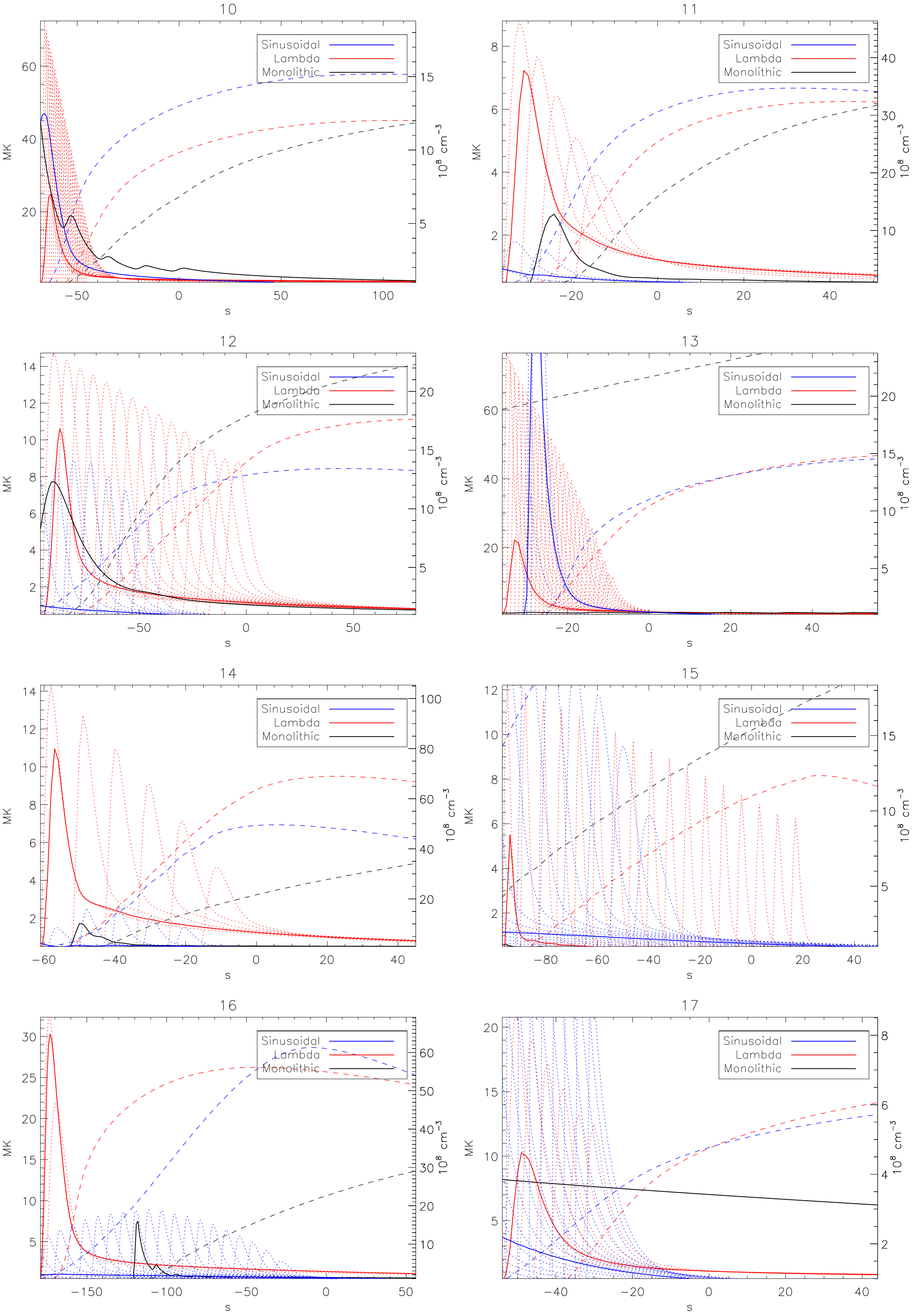

Figure 45: Figures of temperatures and densities used by the model to fit the data not shown in Chapter 3. Numbers 10-17 in Table 7. The dotted lines represent the temperatures of the individual strands, the solid lines are the emission measure weighted temperature. The dashed lines represent the average densities of the ARTB.

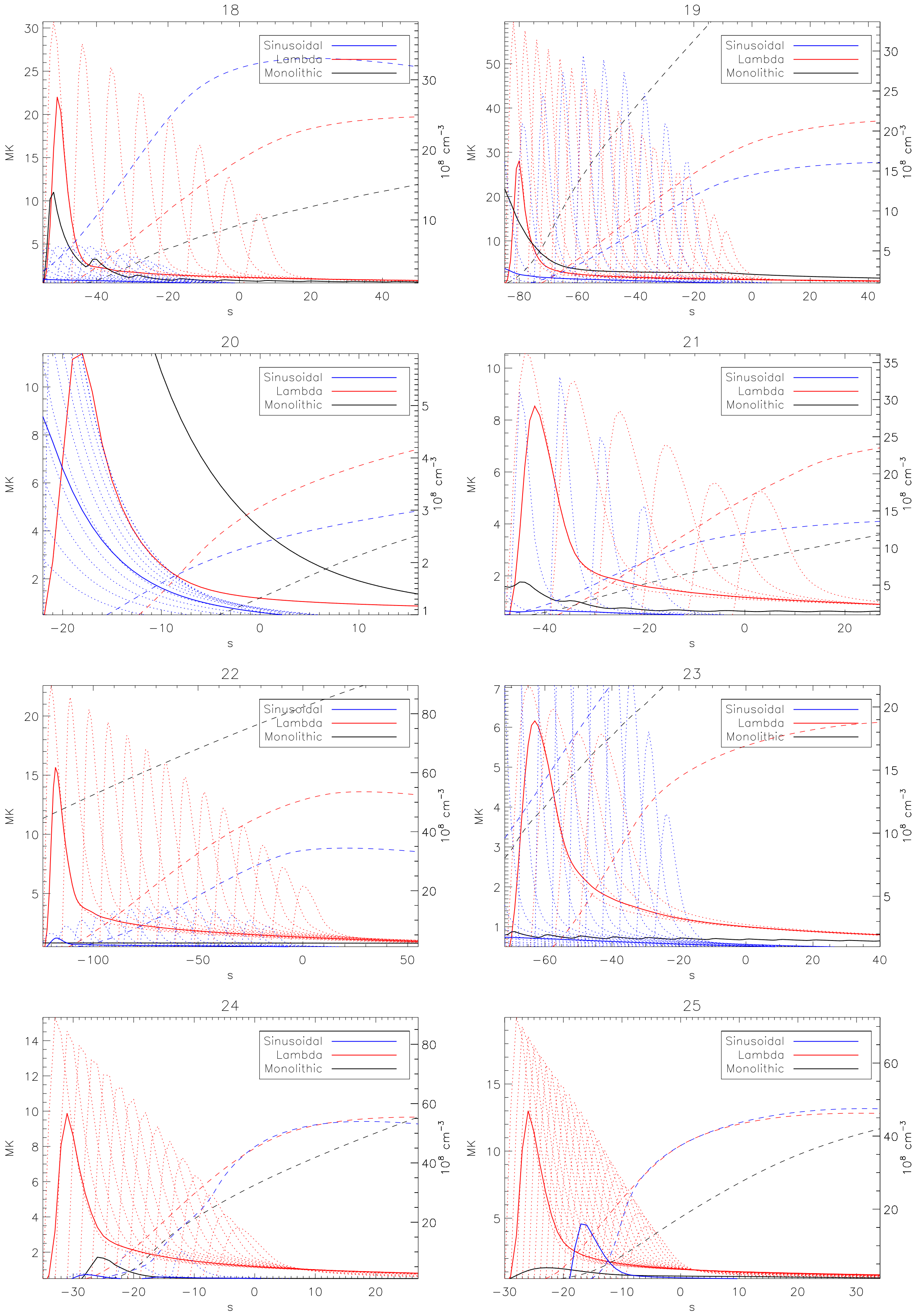

Figure 46: Figures of temperatures and densities used by the model to fit the data not shown in Chapter 3. Numbers 18-25 in Table 7. The dotted lines represent the temperatures of the individual strands, the solid lines are the emission measure weighted temperature. The dashed lines represent the average densities of the ARTB.

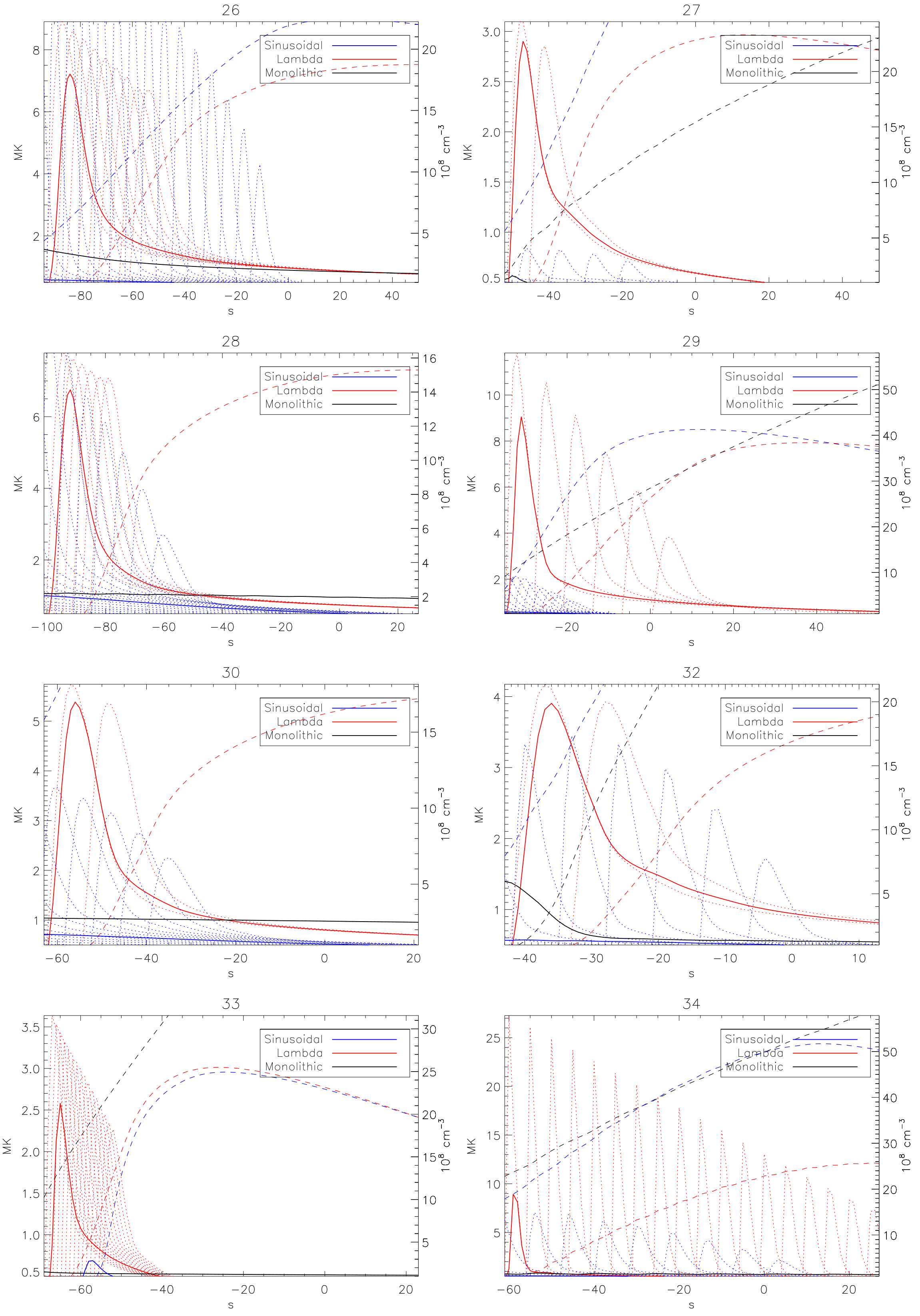

Figure 47: Figures of temperatures and densities used by the model to fit the data not shown in Chapter 3. Numbers 26-30 and 32-34 in Table 7. The dotted lines represent the temperatures of the individual strands, the solid lines are the emission measure weighted temperature. The dashed lines represent the average densities of the ARTB.

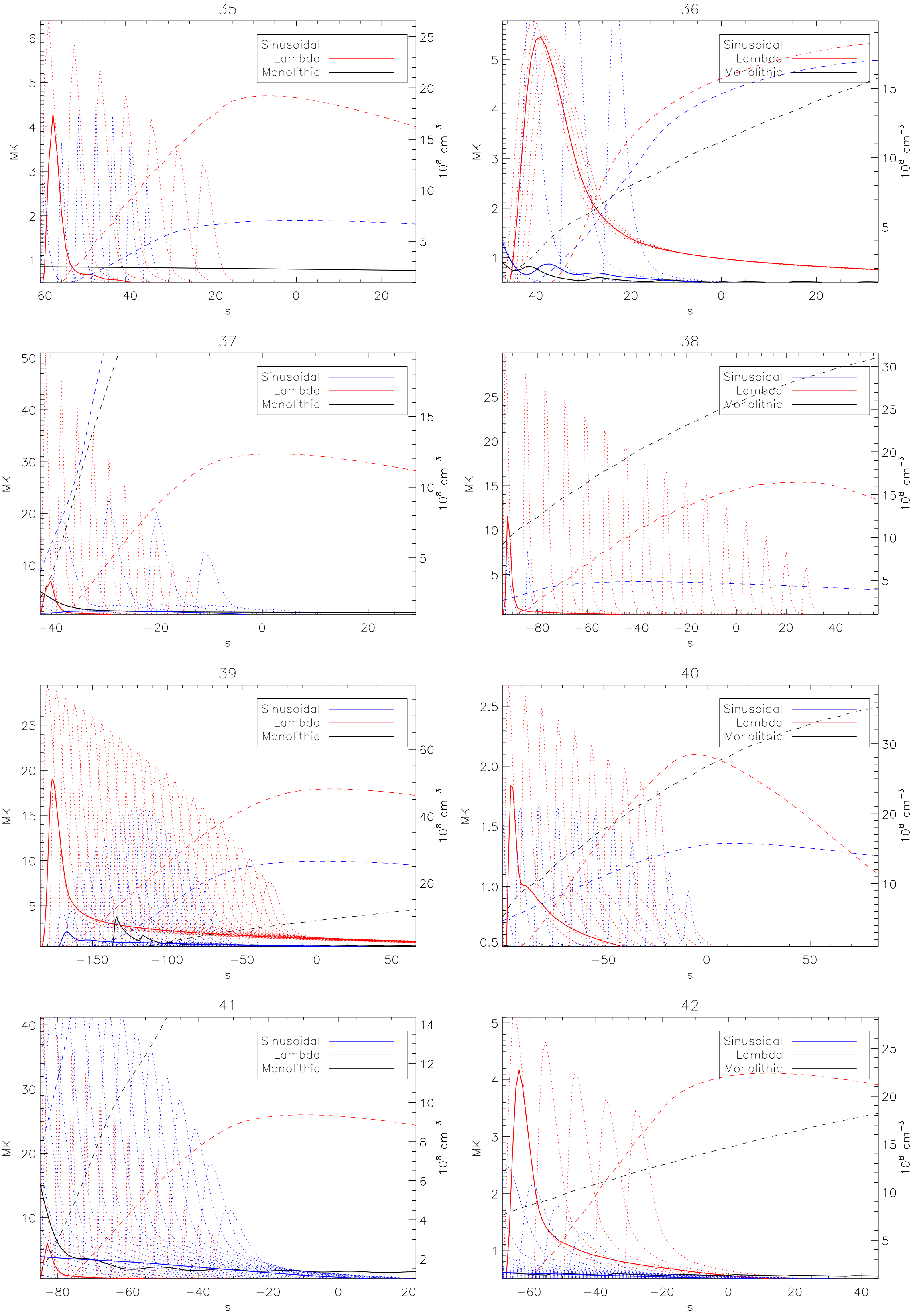

Figure 48: Figures of temperatures and densities used by the model to fit the data not shown in Chapter 3. Numbers 35-42 in Table 7. The dotted lines represent the temperatures of the individual strands, the solid lines are the emission measure weighted temperature. The dashed lines represent the average densities of the ARTB.

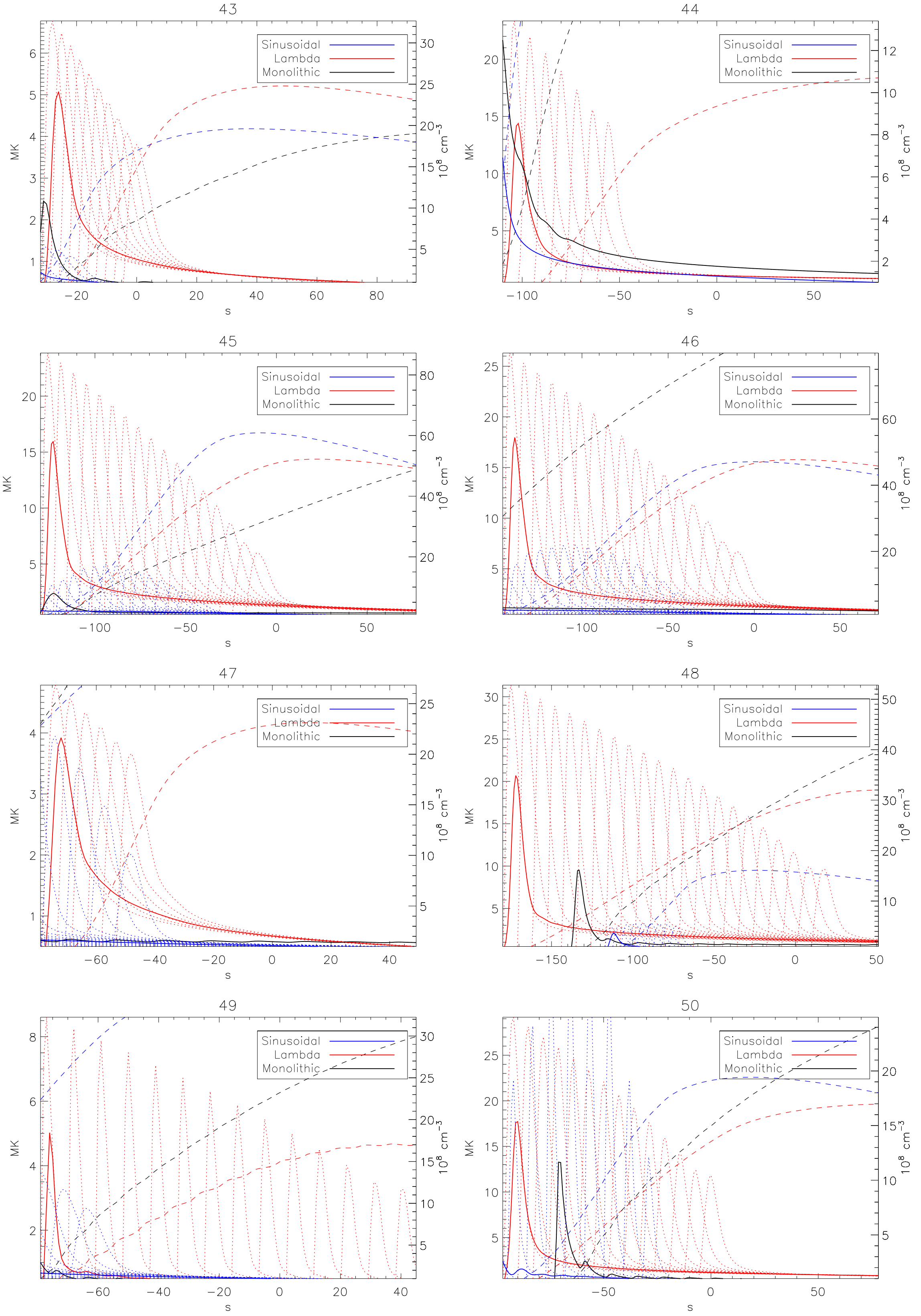

Figure 49: Figures of temperatures and densities used by the model to fit the data not shown in Chapter 3. Numbers 43-50 in Table 7. The dotted lines represent the temperatures of the individual strands, the solid lines are the emission measure weighted temperature. The dashed lines represent the average densities of the ARTB.

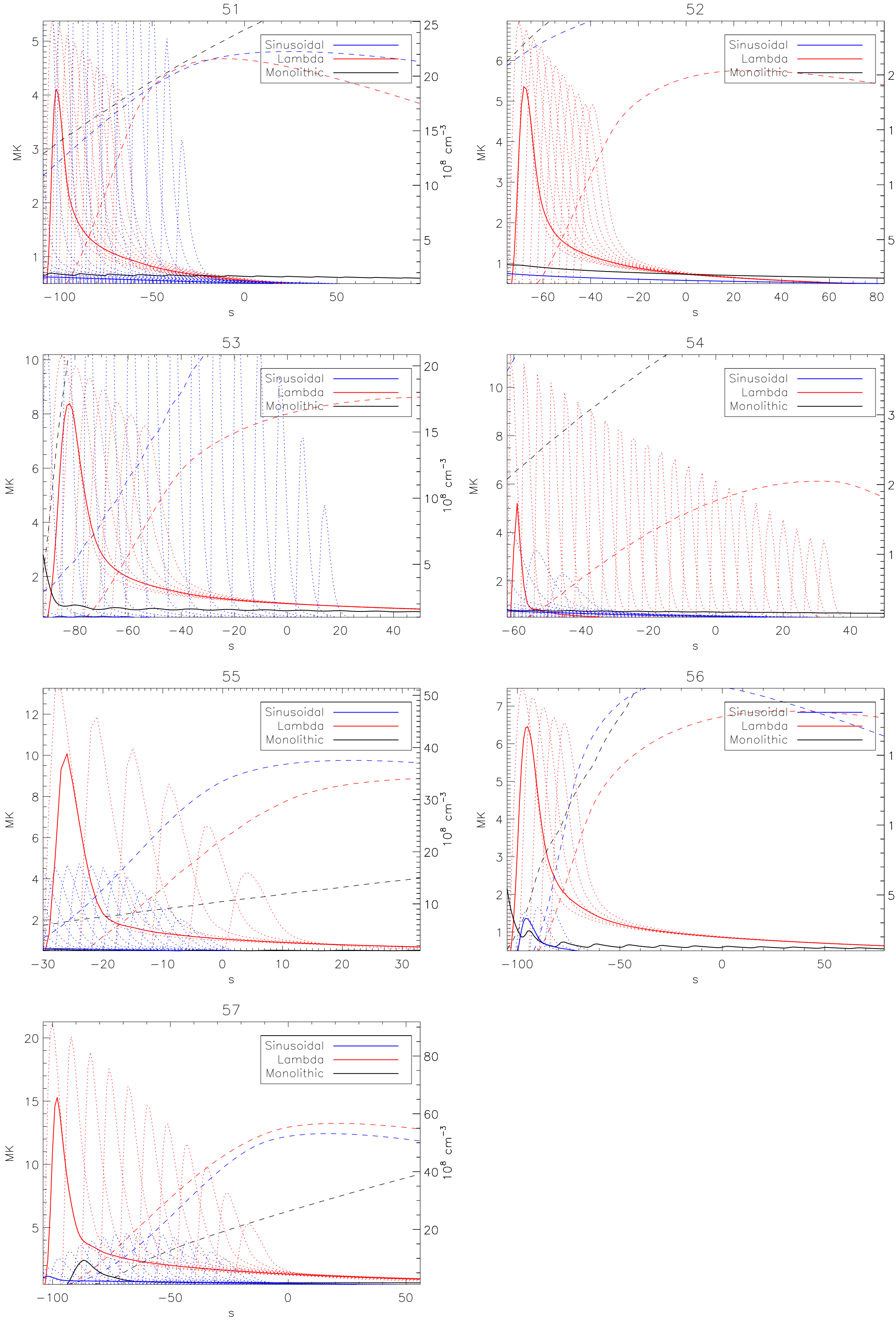

Figure 50: Figures of temperatures and densities used by the model to fit the data not shown in Chapter 3. Numbers 51-57 in Table 7. The dotted lines represent the temperatures of the individual strands, the solid lines are the emission measure weighted temperature. The dashed lines represent the average densities of the ARTB.

REFERENCES CITED

Benz, A. O. 2008, Living Reviews in Solar Physics, 5, 1

Berghmans, D. 2002, in ESA Special Publication, Vol. 506, Solar Variability: From Core to Outer Frontiers, ed. A. Wilson, 501–508

Berghmans, D., & Clette, F. 1999, Sol. Phys., 186, 207

Berghmans, D., McKenzie, D., & Clette, F. 2001, A&A, 369, 291

Brooks, D. H., Warren, H. P., & Ugarte-Urra, I. 2012, ApJ, 755, L33

Brooks, D. H., Warren, H. P., Ugarte-Urra, I., & Winebarger, A. R. 2013, ApJ, 772, L19

Cargill, P. J. 1994, ApJ, 422, 381

Cargill, P. J., Bradshaw, S. J., & Klimchuk, J. A. 2012a, ApJ, 752, 161

—. 2012b, ApJ, 758, 5

Cargill, P. J., Mariska, J. T., & Antiochos, S. K. 1995, ApJ, 439, 1034

Carmichael, H. 1964, NASA Special Publication, 50, 451

Cassak, P. A., Drake, J. F., & Shay, M. A. 2006, ApJ, 644, L145

Charbonneau, P. 1995, ApJS, 101, 309

Cheng, J. X., Kerr, G., & Qiu, J. 2012, ApJ, 744, 48

Cirtain, J. W., Golub, L., Winebarger, A. R., et al. 2013, Nature, 493, 501

Culhane, J. L., Harra, L. K., James, A. M., et al. 2007, Sol. Phys., 243, 19

Deforest, C. E., & Gurman, J. B. 1998, ApJ, 501, L217

DeForest, C. E., Hagenaar, H. J., Lamb, D. A., Parnell, C. E., & Welsch, B. T. 2007, ApJ, 666, 576

Delaboudinière, J.-P., Artzner, G. E., Brunaud, J., et al. 1995, Sol. Phys., 162, 291

Eddy, J. A., & Ise, R. 1979, A new sun : the solar results from SKYLAB

Fletcher, L., Metcalf, T. R., Alexander, D., Brown, D. S., & Ryder, L. A. 2001, ApJ, 554, 451

Forbes, T. G., & Acton, L. W. 1996, ApJ, 459, 330

Freeland, S. L., & Handy, B. N. 1998, Sol. Phys., 182, 497

Galsgaard, K., Archontis, V., Moreno-Insertis, F., & Hood, A. W. 2007, ApJ, 666, 516

Gary, D. E., Hartl, M. D., & Shimizu, T. 1997, ApJ, 477, 958

Golub, L., Deluca, E., Austin, G., et al. 2007, Sol. Phys., 243, 63

Gosling, J. T. 1993, J. Geophys. Res., 98, 18937

Grotrian, W. 1939, Naturwissenschaften, 27, 214

Guennou, C., Auchère, F., Klimchuk, J. A., Bocchialini, K., & Parenti, S. 2013, ApJ, 774, 31

Halain, J.-P., Berghmans, D., Seaton, D. B., et al. 2013, Sol. Phys., 286, 67

Hale, G. E. 1908, ApJ, 28, 315

Hey, J. S. 1946, Nature, 157, 47

Hirayama, T. 1974, Sol. Phys., 34, 323

Hudson, H. S. 1991, Sol. Phys., 133, 357

Janesick, J. 2001, Scientific Charge-Coupled Devices, Spie Press Monograph, Pm83 (SPIE Press)

Kano, R., Sakao, T., Hara, H., et al. 2008, Sol. Phys., 249, 263

Kazachenko, M. D., Canfield, R. C., Longcope, D. W., & Qiu, J. 2012, Sol. Phys., 277, 165

Klimchuk, J. A. 2006, Sol. Phys., 234, 41

Klimchuk, J. A., Lemen, J. R., Feldman, U., Tsuneta, S., & Uchida, Y. 1992, PASJ, 44, L181

Klimchuk, J. A., Patsourakos, S., & Cargill, P. J. 2008, ApJ, 682, 1351

Kobelski, A., Saar, S., McKenzie, D. E., et al. 2012, 456, 241

Kopp, R. A., & Pneuman, G. W. 1976, Sol. Phys., 50, 85

Kosugi, T., Matsuzaki, K., Sakao, T., et al. 2007, Sol. Phys., 243, 3

Krucker, S., & Benz, A. O. 1998, ApJ, 501, L213

Lee, T. T., Petrosian, V., & McTiernan, J. M. 1993, ApJ, 412, 401

Lemen, J. R., Title, A. M., Akin, D. J., et al. 2012, Sol. Phys., 275, 17

Lin, R. P., Schwartz, R. A., Kane, S. R., Pelling, R. M., & Hurley, K. C. 1984, ApJ, 283, 421

Longcope, D. W. 2005, Living Reviews in Solar Physics, 2, 7

Longcope, D. W., McKenzie, D. E., Cirtain, J., & Scott, J. 2005, ApJ, 630, 596

Lyot, B., & Marshall, R. K. 1933, JRASC, 27, 225

McKenzie, D. E. 2002, in Multi-Wavelength Observations of Coronal Structure and Dynamics, ed. P. C. H. Martens & D. Cauffman, 155

McTiernan, J. M. 2009, ApJ, 697, 94

Mercier, C., & Trottet, G. 1997, ApJ, 474, L65

Narukage, N., Sakao, T., Kano, R., et al. 2011, Sol. Phys., 269, 169

Ofman, L., Davila, J. M., & Steinolfson, R. S. 1995, ApJ, 444, 471

Parker, E. N. 1983, ApJ, 264, 635

—. 1988, ApJ, 330, 474

Pesnell, W. D., Thompson, B. J., & Chamberlin, P. C. 2012, Sol. Phys., 275, 3

Qiu, J., Liu, W., Hill, N., & Kazachenko, M. 2010, ApJ, 725, 319

Reale, F., Testa, P., Klimchuk, J. A., & Parenti, S. 2009, ApJ, 698, 756

Reeves, K. K., & Warren, H. P. 2002, ApJ, 578, 590

Santandrea, S., Gantois, K., Strauch, K., et al. 2013, Sol. Phys., 286, 5

Sarkar, A., & Walsh, R. W. 2008, ApJ, 683, 516

Scherrer, P. H., Schou, J., Bush, R. I., et al. 2012, Sol. Phys., 275, 207

Schmelz, J. T., Roames, J. K., & Nasraoui, K. 2007, Advances in Space Research, 39, 1497

Schmelz, J. T., Kashyap, V. L., Saar, S. H., et al. 2009, ApJ, 704, 863

Seaton, D. B., Winebarger, A. R., DeLuca, E. E., et al. 2001, ApJ, 563, L173

Seaton, D. B., Berghmans, D., Nicula, B., et al. 2013, Sol. Phys., 286, 43

Shibata, K. 1999, Ap&SS, 264, 129

Shimizu, T. 1995, PASJ, 47, 251

Shimizu, T., Tsuneta, S., Acton, L. W., Lemen, J. R., & Uchida, Y. 1992, PASJ, 44, L147

Sturrock, P. A. 1968, The Astronomical Journal Supplement, 73, 78

Takeda, A., Kobelski, A., McKenzie, D. E., & Yoshimura, K. 2012, in Astronomical Society of the Pacific Conference Series, Vol. 456, Fifth Hinode Science Meeting, ed. L. Golub, I. De Moortel, & T. Shimizu, 133

Tarr, L., Longcope, D., & Millhouse, M. 2013, ApJ, 770, 4

Tarr, L. A., Longcope, D. W., McKenzie, D. E., & Yoshimura, K. 2014, Sol. Phys., arXiv:1311.3705

Testa, P., De Pontieu, B., Martínez-Sykora, J., et al. 2013, ApJ, 770, L1

Tsuneta, S., Acton, L., Bruner, M., et al. 1991, Sol. Phys., 136, 37

Ugarte-Urra, I., & Warren, H. P. 2013, ArXiv e-prints, arXiv:1311.6346

Viall, N. M., & Klimchuk, J. A. 2011, ApJ, 738, 24

Walsh, R. W., & Ireland, J. 2003, A&A Rev., 12, 1

Warren, H. P. 2006, ApJ, 637, 522

Warren, H. P., Winebarger, A. R., & Brooks, D. H. 2012, ApJ, 759, 141

Winebarger, A. R., Walsh, R. W., Moore, R., et al. 2013, ApJ, 771, 21

Yokoyama, T., Akita, K., Morimoto, T., Inoue, K., & Newmark, J. 2001, ApJ, 546, L69

Yoshida, T., Tsuneta, S., Golub, L., Strong, K., & Ogawara, Y. 1995, PASJ, 47, L15

Zeeman, P. 1897, ApJ, 5, 332

Zuccarello, F., Battiato, V., Contarino, L., et al. 2008, A&A, 488, 1117